Self-Catalyzed GaAs Nanowires:

Controlled Growth and In-Situ Characterization by X-ray Diffraction of Individual Nanowires

DISSERTATION

to obtain the degree of Doctor of Science

Submitted by

M. Sc. Seyed Mohammad Mostafavi Kashani

born on 30.08.1985 in Tehran, Iran

Submitted to the Faculty of Natural Sciences and Technology at the University of Siegen

Siegen 2019

Supervisor and first appraiser: Prof. Dr. Dr. Ullrich Pietsch, University of Siegen
Second appraiser: Prof. Dr. Tilo Baumbach, Karlsruhe institute for technology

Date of the oral examination:
5. November 2019

Copyright © Seyed Mohammad Mostafavi Kashani 2019
Division of Solid State Physics
Department of Physics
Siegen University
Germany

Dedicate to

my mother, Fatemeh Ghorbanpoor,

and my father, Ali Mostafavi Kashani,

who are my role models for the care they have for goodness and humanity.

Zusammenfasung

"*Ich habe keine besondere Begabung, sondern bin nur leidenschaftlich neugierig.*" Albert Einstein

Eines der zentrales Anliegen der Technologie des 21.Jahrhunderts ist die Produktion und Anwendung effizienter und miniaturisierter elektronischer Bauelemente. Zum Beispiel erweisen sich Galliumarsenid-Nanodrähte als überlegene Kandidaten für mehrere (opto-)elektronische Anwendungen, z.B. als Solarzellen. Allerdings sind wir derzeit nur wenige Schritte davon entfernt, die Nanodrähte in unseren Alltag zu bringen. In dieser Arbeit trägt der Autor zu einigen notwendigen Fortschritten bei der Synthese von Galliumarsenid-Nanodrähten auf wirtschaftlichen Si-Substraten bei, das sind: i) Engineering des Nanodrahtwachstums mit kontrollierter Größe und Position, die in zukünftigen Geräten erforderlich sind; ii) Entwicklung grundlegender Erkenntnisse bei der Integration der Nanodrähte auf Si-Plattformen durch In-situ-Monitoring der Nanodrähte während der Synthese.

Der Autor demonstriert seine erfolgreichen Versuche, das Wachstum von vertikal ausgerichteten, selbstkatalysierten Galliumarsenid-Nanodrähten auf Si(111)-Substraten zu kontrollieren. Insbesondere werden die Nanodrähte durch einen Dampf-Flüssigkeit-Feststoff-Mechanismus innerhalb eines Molekularstrahlepitaxiesystems nach der Positionierung von Galliumtröpfchen gezüchtet. Auf dem nativen Oxid von Siliziumsubstraten konnte der Autor die Größe und Homogenität der Nanodraht-Arrays kontrollieren. Auf dem thermischen Oxid von Siliziumsubstraten konnte die Wachstumsposition des Nanodrahtes mit einem fokussierten Ionenstrahl genau definiert werden. Der Autor konnte auch einen signifikante Reduktion der Keimbildung von unerwünschten parasitären Objekten auf dem nativen und thermischen Oxid von Si-Substraten erreichen. Um die Qualität des Wachstums weiter zu verbessern, wurden Temperprozesse nach dem Wachstum untersucht, um das parasitäre Wachstum vollständig zu unterbinden und den Durchmesser der Nanodrähte zu verringern.

Der Autor könnte das Wachstum einzelner Nanodrähte mit Hilfe eines einzigarti-

gen in-situ Röntgenbeugungsexperiments überwachen. Insbesondere wurden die Nanodrähte während des Wachstums und des Rückwachstums (Tempern) von einem Mikrometer großen Röntgenstrahl innerhalb der Synthesekammer beleuchtet. Auf diese Weise wurde die Dynamik der Nanodraht-Kondensation und -Verdampfung extrahiert. Der Autor konnte Analysestrategien entwickeln, um einzelne Nanoobjekte unterschiedlicher Größe (0D, 1D), Kristallorientierung und Struktur zu identifizieren und in-situ zu charakterisieren. Dementsprechend wurden einige originäre Ergebnisse erzielt. Es wurde festgestellt, dass das Nanodrahtwachstum in zwei Phasen abläuft: nämlich i) axiales Wachstum in der Anfangsphase zusammen mit den Winkelinstabilitäten des Nanodrahts; gefolgt von ii) radialem Wachstum in der zweiten Phase zusammen mit der Winkelstabilisierung. Die in-situ-Überwachung während des Wachstums der Rückreaktion ergab, dass die Nanodrähte bei reduzierten Durchmessern Vibrationen oder Biegungen ausführen. Schließlich können die Nanodrähte nach längerer Verdampfung der Facetten flach auf das Substrat fallen. Interessanterweise werden bei Einwirkung der anfänglichen Wachstumsbedingungen die Vibrationen/Biegungen unterdrückt und die Neigung umgekehrt. Der Autor konnte eine periodische Schwingung der Nanodrähte sowohl während des Wachstums als auch innerhalb weniger 0,01° identifizieren, von der wir hoffen, dass sie in Zukunft weiter untersucht werden.

Abstract

“*I have no special talent. I am only passionately curious.*” Albert Einstein

In the 21st century, one of the central concerns of technology is the production and application of efficient and miniature electronic devices. As one example, gallium-arsenide nanowires (NWs) are superior candidates for several (opto)electronic applications, e.g., solar cells. However, we are currently a few steps away from bringing the NWs into our daily lives due to incomplete developments in their engineering as well as basic science. In this thesis, the author makes contributions to necessary advancements in the synthesis of gallium-arsenide NWs on economical Si substrates. These contributions are: i) engineering of the NW growth with controlled size and position, which are required in future devices and ii) developing fundamental understandings in the integration of the NWs on Si platforms by in-situ monitoring of the NWs during synthesis.

The author demonstrates his successful attempts in controlling the growth of vertically aligned self-catalyzed gallium-arsenide NWs on Si(111) substrates. In particular, the NWs are grown by the vapor-liquid-solid mechanism within a molecular beam epitaxy system after gallium droplet positioning. On the native oxide of silicon substrates, the author could control the size and homogeneity of the NW arrays. On the thermal oxide of silicon substrates, the NW growth position could be precisely defined using a focused ion beam. The author could also offer a significant decrease in nucleation of undesired parasitic objects on the both native and thermal oxide of Si substrates. To further enhance the quality of growth, aftergrowth annealing processes were studied, which could entirely remove the parasitic growth and decrease the diameter of the NWs.

For the first time, the author could in-situ monitor the NW growth of individual NWs utilizing a unique in-situ X-ray diffraction experiment. In particular, the NWs were illuminated by a micrometer-sized X-ray beam within the synthesis chamber during growth and reverse-growth (annealing). In this way, the dynamics of NW condensation

and evaporation were extracted. The author could demonstrate analysis strategies in order to identify, and in-situ characterize individual nano-objects of different dimensions (0D, 1D), sizes, crystal orientations, and structures. Accordingly, a few original findings were realized. It was found that the NW growth divides into two stages: i) axial growth at the initial stage along with angular unstablities of the NW; ii) radial growth at the second stage along with angular stabilization. The in-situ monitoring during reverse reaction growth revealed that the NWs undergo vibration/bending at decreased diameters. Eventually, the NWs can fall flat on the substrate after prolonged evaporation of the facets. Interestingly, when exposed to the initial growth conditions, the vibrations/bendings are suppressed, and the tilting is reversed. The author could identify a periodic oscillation of the NWs during both growth and reverse growth within a few 0.01°, which we hope that will be studied further in the future.

Contents

1 Introduction **1**

1.1 Journal and conference presentations of this dissertation 6

1.2 Extra journal and conference presentations 8

2 Crystal structure and epitaxy **11**

2.1 Crystal Structure of Si and GaAs Nanowires 11

2.2 Molecular Beam Epitaxy 15

2.3 Scanning electron microscopy characterization 17

3 X-ray diffraction **19**

3.1 X-ray diffraction experiment 20

3.2 Kinematic theory of X-ray diffraction 26

4 MBE GaAs nanowire growth **33**

4.1 GaAs growth on Si native oxide 34

4.1.1 Reflection high-energy electron diffraction 36

4.1.2 Sample preparation 39

4.1.3 Nanowire growth 39

4.1.4 Further analysis 50

4.1.5 Conclusion 53

4.2 Patterning Si Substrates by Focused Ion Beam 54

4.2.1 Experiment 55

4.2.2 Results and discussion 58

4.2.3 Conclusion 65

5 In-situ monitoring of nanowire growth **69**

5.1 Experimental details 69

5.2 Results and analysis 77

5.3 Discussion 89
5.4 Conclusion 91

6 In-situ monitoring of nanowire stability **93**

6.1 Introduction 93
6.2 Experimental details 95
6.3 Results 96
6.4 Discussion 106
6.5 Conclusion 114

7 Conclusions and outlooks **117**

8 Acknowledgements **139**

List of Abbreviations/Acronyms

DS	Debye-Scherrer
FCC	Face Centered Cubic
fwhm	Full Width at Half Maximum
GaAs	Gallium Arsenide
MBE	Molecular Beam Epitaxy
ML	Mono-layer
μXRD	Micro X-ray Diffraction
NW	Nanowire
PI	Parasitic Island
pMBE	Portable Molecular Beam Epitaxy
RHEED	Reflection High-Energy Electron Diffraction
SEM	Scanning Electron Microscopy
STM	Scanning Tunneling Microscopy
TEM	Transmission Electron Microscopy
UHV	Ultra High Vacuum
WZ	Wurtzite
XRD	X-Ray Diffraction
ZB	Zinc-blende

Chapter 1

Introduction

> "*The next-generation optoelectronics devices will consist of semiconductors, organic molecules, metal complexes, and biological molecules that are regularly positioned in nanospace.*" M.H. Crawford, in Semiconductors and Semimetals, 2017

Nanowires (NWs) are pillars with a diameter ranging between 5 and 200 nm, but they have significantly larger lengths. For example, remarkable lengths are reported for gallium-arsenide (GaAs) NWs (100 μm [1]) and Si NWs (few centimeters [2]). From the science point of view, the small diameter in NWs and the resulting high surface/volume ration can change the physical and chemical properties of the bulk material, e.g., quantization of physical properties, high crystallinity, new crystal structures, and possibility to hetero-epitaxially combine incompatible materials [3]. From the technology point of view, NWs can be used for efficient transportation of electrons and triggering optical excitation leading to miniaturization of electrical devices [4]. Down-scaling of electronics has been an increasing demand in industry since 1960s [5-7]. Semiconductor NWs play a decisive role in the future generation of (opto)electronic devices due to the efficient use of material with highly controllable properties [8].

In this thesis, we focus on GaAs compound NWs. Among semiconductors, GaAs bulk material possesses superior properties in (opto)electronic applications e.g., wide bandgap (with possibility of manipulation by doping), low temperature coefficients, low leakage current and rapid voltage buildup with illumination, and excellent resistance to radiation and moisture (see more information in ref. [9]). Because of its superior properties, GaAs is the most efficient solar cell in the world and accordingly applied in satellites for energy harvesting [9]. Use of NWs in GaAs solar cells, aside from the general NW advantages mentioned above, assists an increased light-trapping and

optical absorption, and reduced photon reflection. GaAs NWs have been used also in other applications such as transistors (best performance among field-effect transistors, higher than carbon nanotubes or graphene [10]), photodetectors/sensors [11-13], and light-emitting diodes [14, 15].

Despite the superior properties of GaAs NWs, their production is still too expensive to be vastly implemented in our daily life. In order to decrease the production costs, the Si substrates have been used as an economical as well as a mature integration platform for GaAs NWs [16]. The crystal structures in GaAs and Si are incompatible because of 4.1% of lattice mismatch. However, the tiny cross-section (diameter) of the NWs facilitates an epitaxial relation between GaAs and Si [17]. In particular, the lattices accommodate at a small contact point, leading to strain relaxation of the crystals [18].

For the synthesize of NWs, the most common approach is the so-called vapor-liquid-solid (VLS) mechanism. Here, vapor (V) source materials are preferentially captured onto a liquid catalyst metal nanoparticle (L) leading to precipitation of material onto a substrate (solid interface) and therefore solidification of a NW (S) [19]. In the VLS mechanism of NW growth, different catalyst elements have been formerly studied: mainly Au [20], but also, e.g., Mg [21], Ag [22], and Pd [23]. In the growth of GaAs NWs on Si, Ga nano-droplets have revealed to be the best catalyst candidates in order to gain the best purity and avoid detrimental mid-gap defects [24, 25]. That is called self-catalyzed GaAs NW growth method. Accordingly, in the last decade, there have been numerous studies on GaAs self-catalyzed NWs grown on Si [14,24-38]. Most of the studies are based on molecular beam epitaxy (MBE), which is also used in the present thesis. Here, the vapor source materials are molecular beam sources. Alternatively, a few groups have reported self-catalyzed GaAs using chemical vapor epitaxy where the source materials are of chemical compounds (e.g., organometallic or hydridic) [39-41]. The latter sources impose sophistication in the chemistry of the system and may be of a disadvantage when the target is to develop basic understandings about the NW synthesis details. Fundamental understandings are highly desirable for the development of reliable NW fabrication processes [42].

For developing fundamental knowledge about NW synthesis details, in-situ monitoring of NW growth is of utmost interest. In-situ studies have been performed using several characterization techniques targeting different physical/chemical aspects of NW growth. By the in-situ studies of NW growth using reflection high-energy electron diffraction (RHEED) [43, 44], transmission electron microscopy (TEM) [45-48], optical reflectometry [49, 50], and scanning tunneling microscopy (STM) [51], one could monitor: movement of adatoms on the crystal surface, surface reconstruction, mono-layer

(ML) growth rates, and chemical compositions. One could study crystal nucleation and phase transformations by mass spectroscopy [52] and RHEED [43, 44]. By infrared spectroscopy, one could access to the surface chemistry of NW growth [53]. In the past years, time-resolved X-ray diffraction (XRD) during MBE growth has been established as a powerful technique [54] for the investigation of the Au-catalyzed GaAs NWs [55], self-catalyzed GaAs NWs [56-58], as well as InAs NWs [59]. These studies used a large X-ray beam size that allows for obtaining statistical information about the evolution of structure [55-57,59] and sizes [58] of large NW ensembles.

In most of the mentioned studies, the convolution trends of several NWs are simultaneously probed. In such cases, the results represent a statistical averaging of an ensemble of NWs and give no access to the inherent fluctuation of the physical properties of individual objects, and therefore, some details are missing. In order to improve the knowledge about NW growth mechanisms, it is required to complement those studies by the investigations which address individual NW monitoring. Up to date, TEM is the most commonly applied technique which obtains local information from individual NWs [45-48 ,60-62]. TEM studies are usually limited to isolated NWs detached from the crystalline substrate surface, and therefore, effects relating to the substrate itself (e.g., diffusion of the growth species on the substrate) or the substrate/NW interface are not accessible. The electrons interact strongly with matter, and therefore, the probing electrons might influence the ongoing processes. In contrast to electrons, the interaction of high energy X-ray photons with matter is much weaker and therefore renders X-rays to be suitable for in-situ studies of free-standing NWs on substrates and under processing conditions. In this thesis, we demonstrate for the first time, in-situ time-resolved non-destructive high-temperature characterization of individual nano-objects employing XRD with a micrometer-sized X-ray beam, which we call mico X-ray diffraction (μXRD). Here, it is possible to identify individual nano-objects of different dimensions, crystal orientations, and structures. In-situ μXRD and ex-situ scanning electron microscopy (SEM) are the main characterization techniques in this thesis. We contribute in both fundamental understandings and engineering of GaAs self-catalyzed NWs toward future mass production of the NW arrays in devices.

This thesis is organized as follows. Chapter 2 and 3 are dedicated to the theory and experimental details. In Chapters 2, an introduction is given to the crystal structure of Si and GaAs, and their epitaxial correlation is visualized. Moreover, briefly, the molecular beam epitaxy technique is discussed, and our unique portable MBE system is introduced. This system is designed for in-situ XRD experiments on crystalline samples and is one of the few currently available setups. Our scanning electron microscopy

approach is also briefly introduced. In Section 3.1, our μXRD experimental details are introduced, which our group has developed that at the synchrotron radiation X-ray source of PETRA III, DESY. In Section 3.2, some aspects of the kinematic theory of XRD is introduced, which is the basis for XRD signal analysis from nanostructures.

In Section 4.1, low growth rate of NW growth on the native oxide surface of Si is discussed. Here, the most common approach of NW growth is criticized, i.e., NW growth initiation by a simultaneous supply of Ga and As vapor source material. Accordingly, a new methodology is suggested. The proposed strategy considers a Ga droplet positioning step (Ga pre-deposition) followed by controlled nucleation of GaAs from those droplets only. The key to control nucleation of GaAs was to perform the NW growth at substrate temperatures above 580 ± 10 °C at low Ga fluxes. By this method, the statistical distribution of the length and diameter of the upright grown NWs decreased to about $3-6$ % of their averaged values. Besides, the growth of undesired parasitic islands could be controlled, and also, 100 % epitaxial NW growth was realized. The detailed report is under review in paper I. The low growth rates were formerly not studied in the literature and particularly advantageous in in situ growth studies. According to the success of this work, it became possible to in-situ monitor the average statistical properties of the growth during the NW synthesis utilizing time-resolved XRD in paper II.

In Section 4.2, we report and detail a lithography-free method to pattern silicon substrates. In particular, a focused Ga ion beam is exposed at regular positions to drill holes in a thermal oxide layer on Si(111). We show that in this method, the hole diameter plays a crucial role to achieve single NWs at the drilled holes. To this end, we demonstrate the critical parameters which define the width of the holes: ion dose quantities, wet etching procedures, and high-temperature steps at the process of growth. As a result, we obtained more than 80% of the vertical NW yield. This patterning method can attain great attention because it provides the following advantages: i) lithography-free procedure, ii) quick patterning process and hole diameter optimization within a small window of trial and error, iii) potential applicability for different material systems. The findings were partly presented in a conference presentation in 2016 [Conference II]; and a detailed report is published in Paper III.

In Chapter 5, we report on monitoring the growth of an individual GaAs NW within our portable MBE utilizing the μXRD setup. After overcoming the experimental sophistication and challenges, a NW was monitored during about 1 hour of its growth onto the patterned Si substrate. Based on this chapter, it was discovered that the NW growth system is divided into two stages. In the first stage, the NW grows axially with

negligible change in the diameter. Interestingly, the NW oscillates within 1° tilt angle with respect to the substrate surface normal. In the second stage of growth, the NW diameter starts to grow, i.e., radial growth. At the same time, the NW tilts toward the substrate surface normal, and the vibrations stop. The outcome of this chapter is in review for a publication in paper IV.

In Chapter 6, individual pre-grown NWs are monitored by the μXRD setup within our portable MBE. In particular, the thermal and angular stability of the NWs were studied during more than six hours of MBE processing at a constant temperature of 610±5 °C, i) without any supply of source material, ii) with arsenic supply, iii) with arsenic and gallium supply. Several additional growth and annealing runs were performed at different annealing temperatures to support and expand the understandings from the in-situ μXRD. The author characterized the additional growth samples by ex-situ SEM. It is revealed that at annealing temperatures below 510±5 °C, the morphology of the NWs does not change, but the Ga seed particle decreases in size or vanish. By annealing at temperatures above 610±5 °C, the NW facets increasingly evaporate. The evaporation of parasitic islands at such annealing conditions are much faster than the NWs opening up the possibility to remove them in applications. Under cases i and ii (annealing without source or with arsenic), at an annealing temperature of 610±5 °C, several hours before full evaporation of the NWs, they become angularly unstable, vibrate/bend, and tilt. The NW tilt was quantified to vary between a fraction of a degree up to several degrees and eventually, the NWs lie down horizontally on the substrate. The in-situ μXRD data evidenced that in case iii (supply of both sources), the tilting process reverses and vibrations/bendings suppress. The high angular and sufficient temporal resolution of the μXRD setup provides us with the possibility to disentangle the tilting and vibrations/bending effects. In particular, minor tilts below 0.01° were resolved and, in our case, around 1 s temporal resolution was implemented with the possibility to increase the temporal resolution to millisecond ranges. The results are published in paper V.

1.1 Journal and conference presentations of this dissertation

The parts of this thesis are presented in journal papers and conference presentations as followed.

[Paper I] S. M. Mostafavi Kashani, "*Low Growth Rate Synthesis of GaAs Nanowires with Uniform Size*", in review for publication.

Contribution: This work has been an independent contribution (Section 4.1).

[Paper II] P. Schroth, J. Jakob, L. Feigl, S. M. Mostafavi Kashani, J. Vogel, J. Strempfer, T. F. Keller, U. Pietsch, and T. Baumbach, "*Radial Growth of Self-Catalyzed GaAs NWs and the Evolution of the Liquid Ga-Droplet Studied by Time-Resolved in-situ XRD*", Nano Lett. 18 (101-108), 2018.

Contribution: I was the responsible person for the NW growth sample based on paper I. I also contributed in the XRD experiments, where using a millimeter-sized X-ray beam, thousands of the NWs were simultaneously illuminated. Due to the size homogeneity of the NW sample, we could extract the statistical average of the NWs' size evolution. The XRD experiment details were designed and analyzed by the colleagues in the Karlsruhe Institute of Technology (the first three authors) (Section 4.1).

[Paper III] D. Bahrami and S. M. Mostafavi Kashani, A. Al-Hassan, A. Davtyan, U. Pietsch "*High yield of self-catalyzed GaAs nanowire growth on silicon (111) substrate templated by focused ion beam patterning*", Nanotechnology 31(18), 2020.

Contribution (*common first author*): I performed the NW growth, XRD measurements, and most of SEM characterization experiments. Further, I designed and developed the paper based on Section 4.2 of my Ph.D. thesis. Danial Bahrami performed the FIB patterning process, cross-sectional SEM imaging, and contributed to developing the corresponding sections in the paper. Danial and I are alphabetically ordered common first authors in this work (Section 4.2).

[Paper IV] S. M. Mostafavi Kashani, V. Dubrovskii, T. Baumbach, U. Pietsch "*In-situ Monitoring of the Growth of a Single Self-Catalyzed GaAs Nanowire by XRD*", in review for publication

Contribution: I mainly performed the work with theoritical insights from V. Dubrovskii, and I have performed the analysis of the data and writing of the paper with insights from the co-authors (Chapter 5).

[Paper V] S. M. Mostafavi Kashani, D. Kriegner, D. Bahrami, J. Vogel, A. Davtyan, L. Feigl, P. Schroth, J. Jakob, T. Baumbach, and U. Pietsch, "*XRD Analysis of the Angular Stability of Self-Catalyzed GaAs NWs for Future Applications in Solar Light Harvesting and Light Emission Devices*", ACS Appl. Nano Mater., vol. 2(2), no. 689-699, 2019.

Contribution: I proposed, designed, and performed the ex-situ annd in-situ experiments, and analyzed the data. I wrote the first draft of the paper together with Dominik Kriegner. The co-authors contributed in the in-situ beamtimes, discussed the results and contributed to the final manuscript (Chapter 6).

[Conference I] S. M. Mostafavi Kashani, et al., "*Towards time-resolved in-situ x-ray scattering of a single nanowire during growth*", DESY User Meeting, Hamburg, Germany (2015)

Content: I presented a poster about Section 4.1.

[Conference II] S. M. Mostafavi Kashani, et al., "*Thermal annealing and growth of a single GaAs nanowire studied by in-situ time-resolved x-ray diffraction*", 13th Biennial Conference on High Resolution X-ray Diffraction and Imaging, X-TOP, Brno, Czech Republic (2016)

Content: I presented a poster about Section 4.2 and Chapter 6.

[Conference III] S. M. Mostafavi Kashani, et al., "*Dynamics of annealing of GaAs nanostructures (nanowires and crystallites) by in-situ time-resolved X-ray diffraction*", NANOWIRES 2017, Lund, Sweden (2017)

Content: I presented a poster about Chapter 6.

[Conference IV] S. M. Mostafavi Kashani, et al., "*Time-resolved in situ X-ray nano-diffraction of a single growing GaAs nanowire by self-catalyzed MBE*", DGK 26th 2018, Essen, Germany (2018)

Content: I gave a talk mainly about Chapter 5.

1.2 Extra journal and conference presentations

During my work at Siegen University in collaboration with the Karlsruhe Institute of Technology, I led other projects as well as participated as a contributor in other works which were not included in the current Ph.D. thesis. The main corresponding international conferences and journal publications are as followed.

[i] Conference Poster: S. M. Mostafavi Kashani, et al., "*X-ray photoemission spectroscopy of GaAs/InAs core-shell nanowires*", Conference NANOWIRES 2014, Eindhoven, Netherlands (2014)

Content: Ex-situ X-ray photoemission spectroscopy on GaAs/InAs core-shell NWs with different shell thicknesses performed in MAX-LAB synchrotron source in Sweden.

[ii] Conference Poster: S. M. Mostafavi Kashani, et al., "*In-situ X-ray studies of GaAs nanowire growth onto silicon(111) substrate*", DGK 23rd, Bonn, Germany (2015)

Content: Time-resolved XRD characterization of ensembles of NWs (asymmetric reflections) was performed at Nano beamline in ANKA, KIT, Germany.

[iii] Conference Poster: S. M. Mostafavi Kashani, et al., "*Towards time-resolved in-situ x-ray scattering of a single nanowire during growth*", Conference III-V NW photonics, Bad Honnef, Germany (2015)

Content: Time-resolved XRD on an ensemble of NWs (symmetric reflections) during growth was performed in NANO beamline of ANKA, KIT, Germany.

[iv] Conference Poster: S. M. Mostafavi Kashani, et al., "*Thermal annealing of GaAs nanowires studied by in-situ time-resolved x-ray diffraction*", Conference NANOWIRES 2015, Barcelona, Spain (2015)

Content: In-situ XRD of an ensemble of NWs during annealing at asymmetric reflections was performed in P09, Petra III, DESY, Germany. Accordingly, a phase-dependent change of structure was found.

[v] Conference Poster: S. M. Mostafavi Kashani, et al., "*Time-resolved in-situ X-ray investigations of the MBE growth-process of semiconductor nanowires*", DESY User Meeting, Hamburg, Germany (2016)

Content: The work was focused on in-situ and ex-situ characterization of NWs during and after growth. Some aspects of the work are summarized as the following: i) time-resolved microstructure and shape of NWs; ii) time-resolved RHEED as a complementary tool; iii) post-growth time-resolved thermal annealing of GaAs nanowires; iv) ex-situ characterization at single nanowire resolution complementary to in-situ data.

[vi] Conference Talk: S. M. Mostafavi Kashani, et al., "*Thermal annealing of GaAs nanowires studied by in-situ time-resolved x-ray diffraction*", DPG, Regensburg, Germany (2016)

Content: In this conference talk, I presented the temperature-dependent effects of thermal annealing (within 300 − 660 °C) on an ensemble of GaAs nano-objects. In particular, a millimeter-sized beam illuminated thousands of NWs and parasitic islands, and asymmetric reflections were in-situ monitored. It was revealed that at a critical temperature of 445±25°C, the intensity of the ZB(200) Bragg reflection significantly drops, whereas the intensity of WZ(10.3) Bragg reflection stays stable. The WZ signal smoothly decreases even at 200 °C increased temperatures. Moreover, in the signal analysis, the contribution of nanowires and the parasitic islands were distinguished.

[vii] Conference Poster: P. Schroth, S. M. Mostafavi Kashani, et al., "*Time-resolved in-situ X-ray diffraction during growth of GaAs nanowires*", Conference Desy User Meeting, Hamburg, Germany (2017)

Content: Some aspects of the work are summarized as the following: i) first successful observation of NW shell growth by time-dependent in-situ asymmetric reciprocal space mapping; ii) clear identification of corresponding Bragg peaks; iii) determination of $\mathrm{InG}a_x\mathrm{A}s_{1-x}$ fraction and composition; iv) strong impact on WZ phase revealed.

[viii] Journal Paper: B. Krause, et al., "*Theoretical and Experimental Study of the Gradient Properties and the Resulting Local Crystalline Structure and Orientation in Magnetron-sputtered CrAlN Coatings with Lateral Composition and Thickness*", Journal of Applied Crystallography 50(4) (2017)

[ix] Journal Paper: A. Davtyan, et al., "*Threefold Rotational Symmetry in Hexagonally Shaped Core–Shell (In,Ga)As/GaAs NWs Revealed by Coherent X-ray Diffraction Imaging*", Journal of Applied Crystallography 50(3) (2017)

[x] Journal Paper: P. Schroth, et al. "*Lithography-Free Variation of the Number Density of Self-Catalyzed GaAs NWs and its Impact on Polytypism*", Journal MRS Communications 145, 1-7 (2018)

[xi] Journal Paper: S. M. Mostafavi Kashani, et al., "*Temperature-Dependent Thermal Expansion and Evaporation Kinetics of GaAs NWs*", paper in preparation

Chapter 2

Crystal structure and epitaxy

"I miss the old days, when nearly every problem in X-ray crystallography was a puzzle that could be solved only by much thinking." Linus Pauling, Princeton University Press, 1994

Epitaxy is a Greek word, where "epi" means above, and "taxis" means in an ordered manner. In epitaxial GaAs nanostructures (NWs or other nano-sized objects), the crystal orientation is similarly aligned with respect to the underneath substrate. In this thesis, Si(111) single-crystalline wafers are used as the substrate. Here, the crystallographic planes with a Miller index of (111) in the crystal of Si and epitaxial GaAs nano-objects orient parallel to each other. In Section 2.1, the crystal structures of Si and GaAs are introduced, and their epitaxial correlation is visualized. In Section 2.2, our epitaxy synthesis chamber is presented. In Section 2.3, our SEM approach is explained.

2.1 Crystal Structure of Si and GaAs Nanowires

In the following section, it is assumed that the reader knows the basic crystallography of Bravais lattices, Miller indices of planes and directions, and characteristics of face-centered cubic (FCC) and hexagonal lattices (e.g., 3D and 2D close-packing and ABCABC/ABAB stacking). The reader can find a thorough review of such topics in basic crystallography books, e.g., ref. [63]. In Figure 2.1a−l, from left to right, the atomic arrangements of diamond Si, zinc-blende (ZB) GaAs, and wurtzite (WZ) GaAs crystals are shown. From top to bottom, the Bravais lattice unit cell, a top-view, and a side view of the atomic arrangements are visualized. In particular, the atomic arrange-

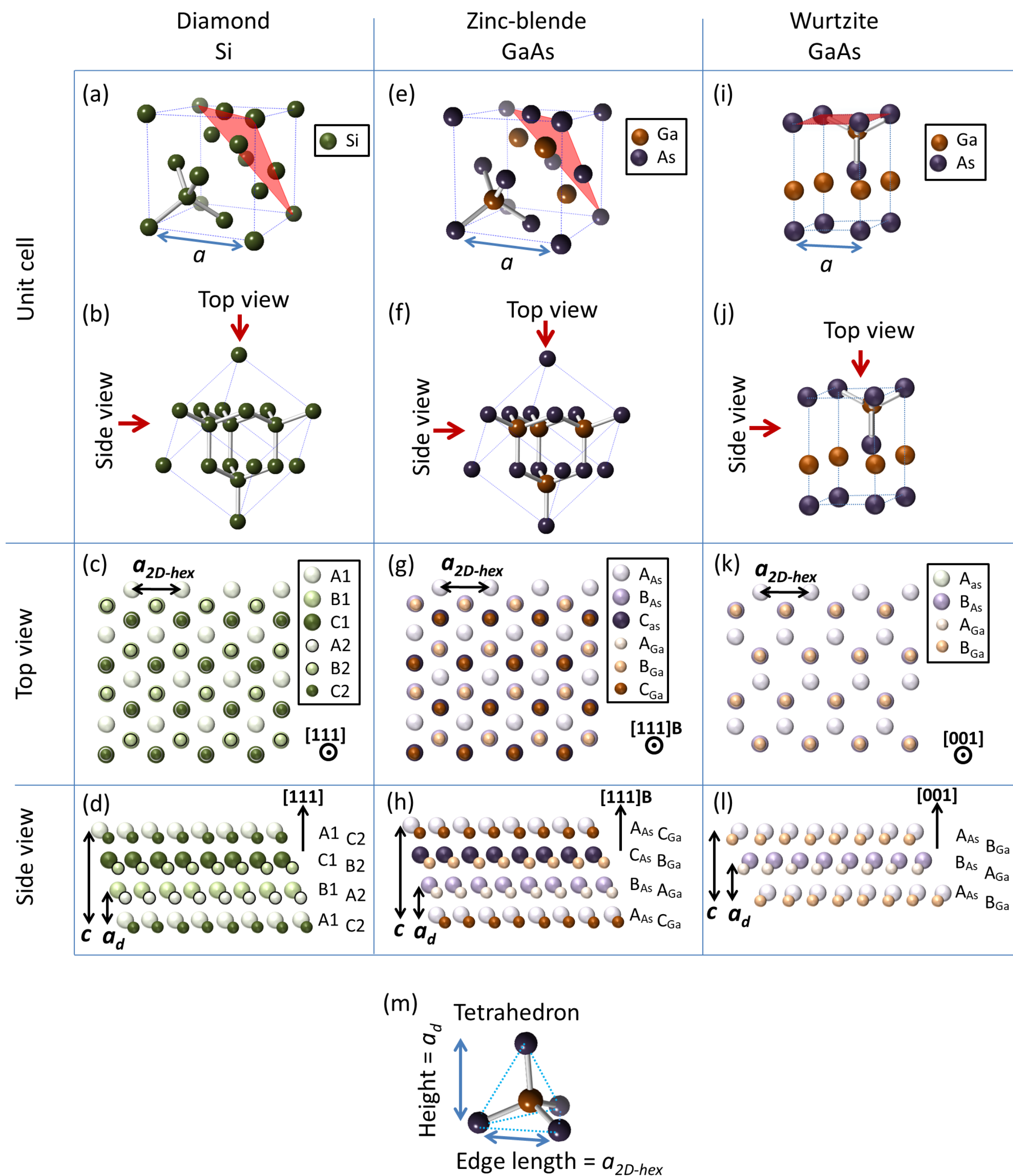

Figure 2.1: This figure illustrates the arrangement of atoms in diamond Si, zinc blende GaAs, and wurtzite GaAs. The unit cells of diamond Si and zinc-blende GaAs are depicted in cubic Bravais lattice and compared to hexagonal wurtzite lattice. The epitaxial correlation between GaAs and Si is visualized by showing the in-plane and out-of-plane atomic arrangements at the ABCABC and ABAB stacked planes. For details, see the text.

ments are shown along (top-view) and perpendicular (side view) to [111], [111]B, and [001] directions, in diamond, ZB, and WZ structures, respectively. Those Miller indices are the normal directions to the planes with ABCABC and ABAB stackings. The basis for comparison between those crystal structures is the stacking of the planes in which the atoms are 2D hexagonally arranged (equivalent to 2D close-packed (111) planes in FCC).

The arrangement of atoms in Si crystals is similar to the well-known structure of diamond. One could visualize the diamond structure by combining two FCC Bravais lattices: the first lattice at the main coordinate system, (0,0,0), and the second lattice at a translated center of coordinate to $(1/4, 1/4, 1/4) \times a$, where a is the Bravais axial distance parameter i.e., lattice constant (see Figure 2.1a). The stacking of (111) planes in FCC is ABCABC where the atoms at each plane type occupy a unique set of tetrahedral sites and appear identical from a projected view along [111] direction (see ref. [63]). In diamond structure, two types of "A" planes exist originating in those two FCC structures, and we denote them by A1 and A2 (the same applies for B1, B2 and C1, C2). The ABC stacking of (111) planes in FCC can be re-written in the diamond structure as following: A1A2B1B2C1C2. The indicated (111) plane within the diamond unit cell in Figure 2.1a is a C1 type which is parallel to other (111) planes (A1, A2, B1, B2, and C2). To better visualize the stacking of the (111) planes in diamond, the unit cell in Figure 2.1a is rotated and aligned in Figure 2.1b vertically along [111] (i.e., the normal of (111) planes). The top-view of diamond structure in Figure 2.1c shows the hexagonal arrangement of atoms where the (111) planes are stacked onto each other. Note that those atoms are not shown in a (111) 2D close-packed illustration. In fact, contrary to FCC, in the diamond structure, the 3D close-packing does not result in 2D hexagonal close-packing in (111) planes [1], [2], [3]. Nonetheless, here, the atoms are hexagonally arranged in 2D similar to FCC. At the top and side view perspective of diamond (along and perpendicular to [111]) in Figure 2.1c–d, the (111) atoms of the unit cell are extended for better visualization. It is worth noting that each atom in diamond structure is bonded with four atoms within a tetrahedral molecular geometry (see Figure 2.1m). A few tetrahedral molecular arrangements are highlighted within the unit cell in Figure 2.1a,b. As illustrated in Figure 2.1d, for example, A2 planes are sandwiched between A1 and B1 planes. Here, each atom in an A2 plane locates at the center of a tetrahedron with an atom of A1 and three atoms of B1 at the tetrahedron corners.

[1] The (111) planes have the maximum surface density in FCC but not in diamond. In diamond, density of surface atoms in (111) planes is $4/\sqrt{3}a^2$ and in (110) planes is $4/\sqrt{2}a^2$.

[2] The atomic packing factor of FCC is $\sim$0.74

[3] The atomic packing factor of diamond is $\sim$0.34

In perfect tetrahedral molecular geometry, we have $g_{tetrahedron} = \frac{\text{Height}}{\text{Edge Length}} = \sqrt{3/2}$ and the center of the tetrahedron (central atom) is at 1/4 of the height (see Figure 2.1m for a depicted illustration and ref. [64] for basic understanding about tetrahedral molecular geometry). As seen in Table 2.1, in diamond-structured Si, the distance between nearest neighbors in (111) planes (a_{2D-hex}) is 3.8403 Å corresponding to the tetrahedron edge length, and the distance between A1 and B1 (a_d) is 3.1356 Å corresponding to the tetrahedron height. In this chapter, $\frac{a_{2D-hex}}{a_d}$ is accounted as a geometry factor (g). For diamond $\frac{g}{g_{tetrahedron}} = 1$ which means that the atoms are arranged in an ideal tetrahedral molecular geometry. Moreover, each (111) plane is sandwiched between two other (111) planes at a relative height of 1/4 (see Figure 2.1d). For example, A2 is located at a height (along [111]) which is 1/4 of the distance between A1 and B1.

With the detailed visualization of the diamond structure, the GaAs structure can be pictured as follows. If one substitutes atoms of Ga and As in those above explained two FCC sub-lattices in diamond, the so-called ZB GaAs structure is constructed: in Figure 2.1e, As and Ga sub-lattices are coordinated at (0,0,0) and (1/4,1/4,1/4)×a, respectively. The stacking of (111) planes can be re-written as $A_{As}A_{Ga}B_{As}B_{Ga}C_{As}C_{Ga}$. The indicated plane in Figure 2.1e is a C_{As} plane. Similar to the visualization steps of diamond structure explained above, the unit cell is aligned to [111] in Figure 2.1f where the top and side views are indicated, and they are illustrated in Figure 2.1g and h. In the diamond structure, there is a 2-fold rotational symmetry along [111]. However, in the ZB structure, this symmetry is broken. The polarity of the surface is defined by the terminating element where group III is labeled as (111)A and group V is labels as (111)B. For example, the surface in Figure 2.1g and 2.1h is terminated by group V atoms (As), and it is called GaAs(111)B. Here, the surface normal ([111]B) is the growth direction of GaAs NWs on Si(111). Each Ga atom can be seen at the center of a tetrahedron where the corners are occupied by As atoms (and vice versa). The lattice parameters of Si and GaAs bulk materials are seen in Table 2.1 [65]. As seen in Table 2.1, $g/g_{tetrahedron} = 1$ meaning that the atoms are arranged in ideal tetrahedral molecular geometries in GaAs ZB. The lattice constant of Si in cubic structure is about 4.1% larger than that of GaAs in both in-plane (111) and out of plane directions (a_d).

Another possible structure of GaAs which has been so far only observed in nano-objects (not in bulk) is called GaAs WZ. As shown in Figure 2.1i–l, in GaAs WZ structure, the planes of the hexagonally arranged atoms are stacked onto each-other as following: $A_{As}A_{Ga}B_{As}B_{Ga}$. That can be compared with hexagonal Bravais lattice where the atomic stacking is ABAB. The indicated plane in Figure 2.1i is a A_{As} plane. As pointed out above, the top-view along WZ [001] is equivalent to that of [111]B in

ZB and [111] diamond structures. One type of tetrahedral sites stays unfilled in a hexagonal arrangement, which is also visualized by comparing Figure 2.1k and 2.1g. In the GaAs WZ structure, $g/g_{tetrahedron} =\sim 0.9903$ meaning that it deviates from an ideal tetrahedral molecular geometry (see Table 2.1). In particular, as compared to (111) GaAs ZB planes, in GaAs WZ, the distance between nearest neighbors within the (001) planes, a_{2D-hex}, is compressed ∼-0.0033% and the distance between consecutive (111) planes (e.g., A1−B1) ,a_d, is expanded ∼+0.0064% (compare a_{2D-hex} and a_d in Figure 2.1k,g and Table 2.1). This is the origin of distinguishing WZ from ZB GaAs in XRD measurements. It is interesting to note that as a result of the anisotropic change of the atomic arrangement, the relative height of the central atom deviates (increases) from the value $1/4$ in an ideal tetrahedral molecular arrangement.

	Lattice constant a (Å)	Atomic distance a_{2D-hex} (Å)	A1−A1 distance c (Å)	A1−B1 distance a_d (Å)	$g/g_{tetrahedron}$ $\frac{a_{2D-hex}/a_d}{\sqrt{3/2}}$
Si	5.43102	3.8403	9.4068	$c/3 = 3.1356$	1.0000
$GaAs_{ZB}$	5.6536	3.9977	9.7923	$c/3 = 3.2641$	1.0000
$GaAs_{WZ}$	3.9845	3.9845	6.5701	$c/2 = 3.2850$	0.9903

Table 2.1: Lattice parameters of diamond-structured Si and GaAs ZB: a is the lattice constant. a_{2D-hex} is the distance between the nearest neighbors in 2D hexagonal planes, i.e., (111) in diamond and ZB cubic lattices and (001) planes in WZ lattice. c is the distance between consecutive A1 planes in diamond and consecutiveA_{As} planes in ZB and WZ. a_d is the A1−B1 planar distance in diamond and A_{As}-B_{As} planar distance in ZB and WZ. $g = a_{2D-hex}/a_d$ is the geometry factor of the tetrahedral sites, which is the aspect ration between the atomic distance in the base and the height of the tetrahedron. $g_{tetrahedron}$ is $\sqrt{3/2}$. For details, see the text. Information of Si and GaAs ZB is taken from ref. [65] and GaAs WZ is taken from ref. [66].

2.2 Molecular Beam Epitaxy

The revolution in sub-nanometer (atomic) control of crystal growth started in the 1950s by the German scientist, K. G. Günther, using MBE [67]. MBE was initially known as the three-temperature method, where molecular beams of different constituents impinged onto a suitably heated clean substrate in ultra-high vacuum (UHV) conditions. That resulted in a controlled deposition of high-quality stoichiometric compound films [68]. Since then, this technique has been widely used to prepare innovative devices or new materials (e.g., multiple constituents/dopants). Moreover, because of the slow rates of growth and versatility of the system, MBE has been used to develop fundamental understandings of, e.g., thermodynamics, surface reaction kinetics and growth dynamics of different material systems. Nowadays, MBE is used in a wide range of

material research and commercial mass production (for more information see ref. [69]). The MBE system in this thesis is designed by the company Createc as a transportable machine with a small size of growth chamber as compared to common MBE reactors [70]. This compact equipment includes all the standard MBE components such as pressure gauges, vacuum pumps, cooling shroud, effusion cells with shutters, manipulator, manipulator shutter, and a storage chamber with the possibility of storing up to four growth samples. In Figure 2.2, a scheme of the portable MBE (pMBE) is illustrated. The combined weight of the growth chamber and storage chamber in Figure 2.2 is about 155 kg. This part is installed on heavy load diffractometers, as will be shown in Figure 3.1. In addition to this setup, a transport box (vacuum suitcase) was used for in vacuo sample transfer where several samples could be prepared elsewhere, stored, and UHV transferred. Our setup is based at the UHV-laboratory at the former synchrotron radiation facility ANKA, Karlsruhe Institute of Technology, where the growth calibrations in this thesis have been performed. For in-situ XRD measurements, the system was transported to the beamline P09 at PETRA III, DESY.

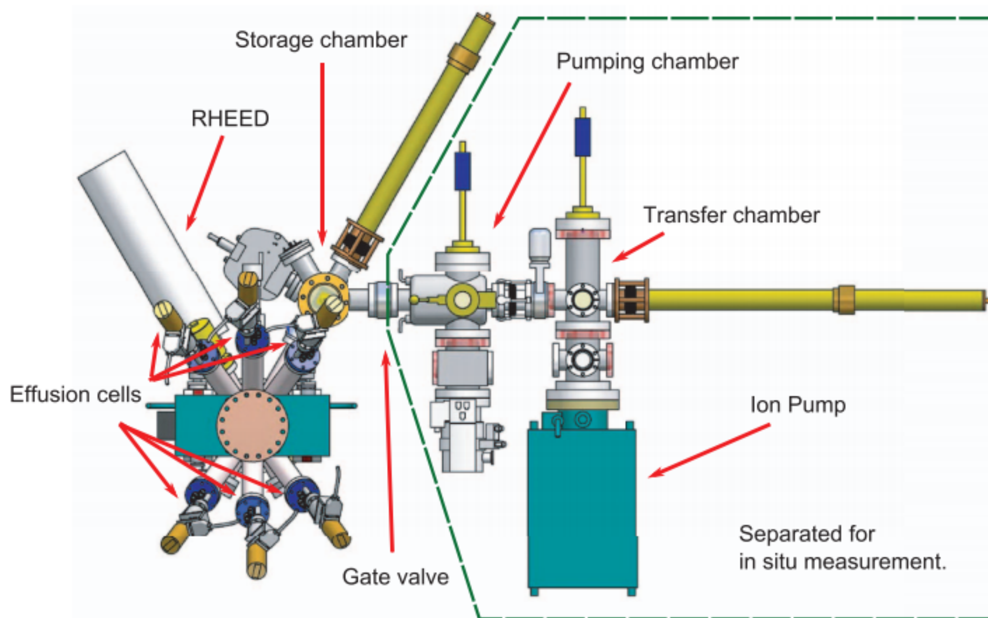

Figure 2.2: Schematic illustration of the portable MBE system taken from ref. [70]. The green box indicates the stationary part of the setup, which is separated from the portable part of the system during X-ray experiments.

2.3 Scanning electron microscopy characterization

Scanning electron microscopy was used to study the NW morphology after MBE growth. For that purpose, the samples were removed from the pMBE chamber and characterized using electron beams with 5 kV acceleration voltage and detecting secondary scattered electrons. The view angles to the substrates on the presented SEM images were 0°, 30°, and more than 85° away from the substrate surface normal. It is worth noting that the vertical scale is affected by tilting the substrate: for example, thirty-degree view angle results in the reduction of the apparent vertical scale of the upright NWs by a factor of $\sin 30° = 0.5$, on the corresponding SEM images. The cross-sectional SEM images are taken at substrate tilt angles more than 85°, where the vertical deviation of the image is negligible ($\sin 85° > 0.99$).

Chapter 3

X-ray diffraction

"*On a dark November evening in 1895, Wilhelm Conrad Röntgen was perplexed by a fluorescent screen in his laboratory that was glowing for no apparent reason. Röntgen's experiment on how cathode-ray tubes emit light appeared to be affecting something that was not part of the study. It took weeks spent eating and sleeping in his lab to identify the cause of this mysterious glow.*" [71]

The term "X-rays" was used to address some unknown (X) rays observed accidentally in the laboratory of the German physicist: W. C. Röntgen. He revealed some characteristics of the X-rays, which rewarded him a Nobel Prize in 1901. In 1912, Max von Laue investigated crystals for the first time using XRD which rewarded him the Nobel Prize in physics 1914 [72]. He discovered that the wavelengths of X-rays are in a similar range as the atomic distances in the solids. Accordingly, the field of X-ray crystallography was born to study the unseen 3D periodic atomic arrangements of matter. After 1914, one century of increasing attention to the field of X-ray crystallography is recognized by 13 more Nobel Prizes in multidisciplinary fields of physics, chemistry, or even medicine [73].

In this chapter, the capabilities of XRD is presented in the frame of our available equipment. First, in Section 3.1, a brief introduction is given to the type of XRD experiment presented in this thesis. In Section 3.2, we briefly present the kinematic theory of X-ray diffraction. The next chapters refer to Section 3.2 for the analysis of XRD data taken from nano-objects.

3.1 X-ray diffraction experiment

In Figure 3.1, a schematic illustration of the XRD setup is shown, where the pMBE chamber is installed on the heavy-duty diffractometer of the P09 beamline, Petra III, DESY [74]. The main components of this setup are the X-ray source, diffractometer, sample, and detector. The X-ray source is a storage ring emitting a white-light, meaning that it contains a spectrum covering a wide range of X-ray energies. The beam goes through various optic elements along the beamline to provide the suitable monochromatic X-ray beam for the experiment as described detailed in ref. [74]. The resulting beam approaches the experimental hutch depicted in Figure 3.1 and is focused to the center of the goniometer using compound refractive lenses (CRL) following some additional steps presented in the caption of the figure. The beam then passes through a Be-window on the pMBE chamber to illuminate a growth sample within the pMBE chamber. The sample is at the center of the pMBE chamber depicted in yellow in Figure 3.1b. Note that the sample is aligned to the center of rotation of the goniometer. The goniometer allows for adjustment of the sample and the detector positions. Figure 3.1b illustrates the accessible angular range considering spatial restrictions of the pMBE. Figure 3.1c illustrates the respective motors used to rotate the sample. In this way, time-resolved diffraction experiments are carried out to follow MBE processes in-situ. The samples, as presented in Chapter 2, are Si substrates with overgrown epitaxial GaAs nano-objects. The diffracted X-ray beam passes through the other Be-window on the pMBE and is monitored using a 2D detector. The experimental details are further introduced in the following.

X-rays

For the experiments, an intense monochromatic X-ray beam has been used with a beam flux of $\sim 1.4 \cdot 10^6$ photons$\cdot$s$^{-1} \cdot \mu$m^{-2}. This flux is by orders of magnitude more intense as compared to a conventional laboratory X-ray source. Therefore, the intensity (brilliance) is sufficient to study an individual nano-object. The X-ray photon energy (E) was 15 keV with an energy resolution of $\frac{\Delta E}{E} = 10^{-4}$. That is equivalent to a wavelength (λ) of 0.826 Å ($\lambda\,[\text{Å}] = \frac{12398}{E\,[\text{eV}]}$). The experimental hutch of the P09 beamline is located at a distance of 86.5 m down streams from the source providing a nearly planar X-ray wave with a beam cross-section of about 0.9 mm [74]. Moreover, together with our master student, Jonas Vogel, we developed the equipment to focus the original beam down to a micrometer-size using a set of beryllium compound refractive lenses

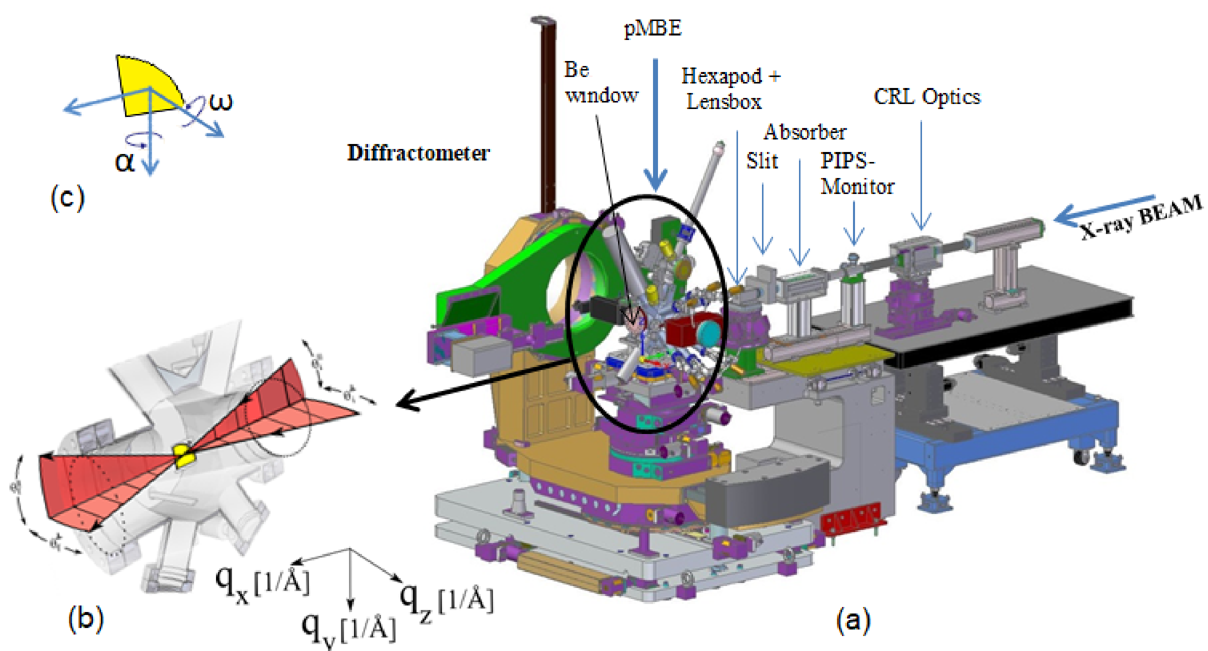

Figure 3.1: Panel (a) shows a schematic illustration of the components in the second experimental hutch in P09 beamline of the Petra III, Desy including the pMBE system installed on the heavy-duty Huber-table of the diffractometer. Here, the beam comes from the right, and it is focused using the compound refractive lenses. The intensity of the beam is monitored at passivated implanted planar silicon (PIPS) diodes. The beam is attenuated at an absorber box and collimated at an in-vacuum slit system. Panel (b) illustrates the illumination of a sample (depicted in yellow) within the pMBE chamber by X-rays (depicted in red). The X-ray beam passes through the Be-windows (dashed circles at right). The sample can be reached within a ~18° angular range in both $\vartheta\|$ and $\vartheta^{\perp}$ directions, as indicated. Panel (c) Illustrates the motor movements to fulfill the Bragg conditions. α rotates the goniometer around its surface plate's normal. Because the sample is always perpendicular to the goniometer surface in this geometry, α defines the angle between the sample surface and incoming beam. ω is a motor at the pMBE chamber, which rotates the sample around its surface normal.

(CRLs) [75]. The focused beam had a size of 1.8±0.2 µm in vertical and 6.0±0.4 µm in horizontal directions measured by scanning through a sharp edge (*knife-edge-method*). The maximum photon flux of the micrometer-sized beam was $\sim 4 \cdot 10^8$ photons$\cdot$s$^{-1} \cdot \mu$m^{-2}. At the photon energy of 15 keV, the focal distance of the focusing setup was about 75 cm, which gives a beam divergence of $\sim 0.068°$ [75].

Diffraction

The millimeter or micrometer-sized X-ray beams illuminated the samples in order to perform the XRD experiments. In order to understand diffraction at a solid, the simplest explanation is given by the Bragg equation. Here, it is assumed that the incident

beam reflects from parallel crystallographic planes. The reflected wave fields interfere with each other towards the direction of the detector. To satisfy constructive interference (diffraction condition), the difference between the pathways of the wave fields (rays) from consecutive crystallographic planes is an integer, n, factor of the beam wavelength:

$$n\lambda = 2d_{hkl}\sin\theta_B, \tag{3.1}$$

where d_{hkl} is the lattice spacing between the diffraction planes with (hkl) Miller indices. Thus, θ_B gives the angle between the incoming beam and the crystallographic planes under the diffraction condition. Bragg´s formula provided an epoch-making explanation of XRD and was rewarded by a Nobel Prize in physics in 1915, one year after the Laue's Nobel Prize [76]. Figure 3.2a shows schemes of symmetric and asymmetric diffraction set-ups. In symmetric diffraction, the crystallographic planes at which the X-rays are reflected are parallel to surface (yellow lines). Therefore, the angle between the surface and both the incoming beam and outgoing beam are equal to the Bragg angle (θ). $\overrightarrow{q} = \overrightarrow{k'} - \overrightarrow{k}$ is the momentum transfer wave-vector of a plane wave ($\overrightarrow{k}$) that hits the surface of a crystal; and $\overrightarrow{k'}$ is the diffracted wave-vector. In symmetric diffraction, $\overrightarrow{q}$ is perpendicular to surface. In an asymmetric diffraction geometry, as illustrated in Figure 3.2a, the Bragg diffraction planes (illustrated in green circles and red lines) are not parallel to the surface ($\overrightarrow{q}$ is not perpendicular to the surface). The accessible Bragg reflections are illustrated in Figure 3.2b on the basis of the momentum transfer wave-vectors $\overrightarrow{q}$. Here, the y-axis shows the components of $\overrightarrow{q}$ perpendicular to surface and the x-axis shows its component parallel to surface. The detailed calculations are presented in ref. [77]. In Table 3.1, the characteristics of the GaAs Bragg reflections studied in this thesis are presented; in particular, symmetric reflection (111). In a few experiments, asymmetric reflections, (220), $(10.3)_{\mathrm{hex}}$ [1], and (311) were studied. The detailed analysis of the results regarding the asymmetric reflections are not presented in this thesis.

Diffractometer and detector image

The diffracted beam was monitored using a 2D Pilatus 300k detector (487×619 channels) with a pixel size of 172×172 μm^2 mounted at a distance of 1100 mm apart from the sample. In order to fulfill the Bragg conditions at the symmetric (111) reflection, α

[1] The index of "hex" refers to the hexagonal surface coordinate system [63].

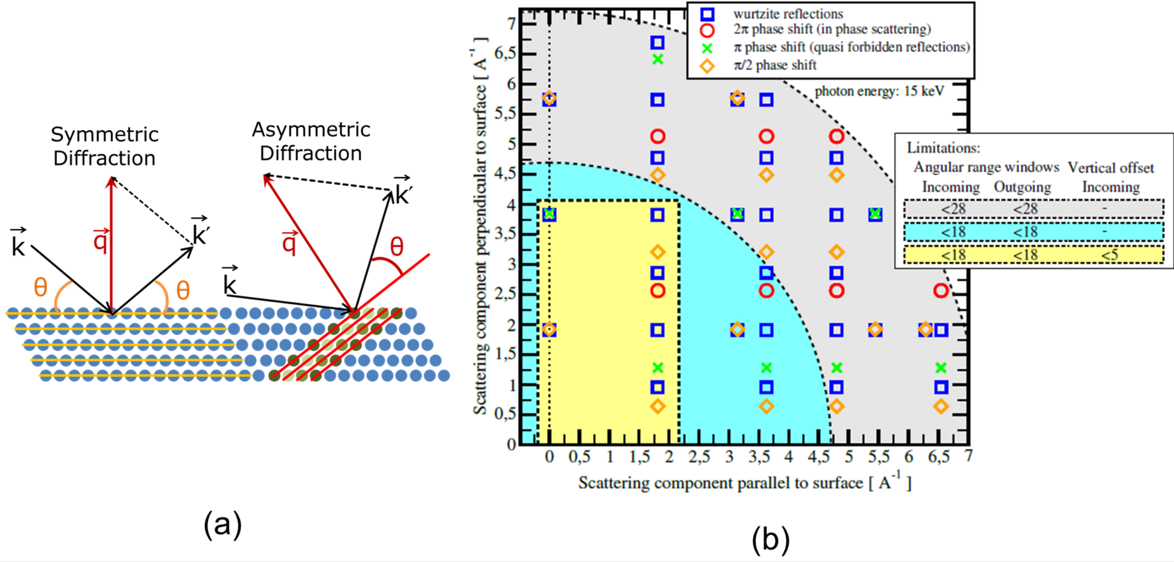

Figure 3.2: Panel (a) shows schematics of symmetric and asymmetric diffraction: $\vec{k}$ and $\vec{k'}$ are the incoming and outgoing wave-vectors, respectively; $\vec{q}$ is the transfer wave-vector, θ is the Bragg angle. Panel (b) shows the available Bragg reflections within pMBE chamber at an X-ray energy of 15 keV. The gray background with angular range window of 28° at the incoming and outgoing angles represent the new pMBE chamber and yellow and blue represent the former chamber at which all the experiments in this thesis were performed. At a typical vertical offset of the substrate within 5°, the yellow region is accessible within the pMBE. For details, see page 33 of ref. [77].

Reflection	θ_B [°]	β [°]
(111)	7.27	0
(220)	11.93	35.26
$(10.3)_{\text{hex}}$	13.17	32.14
(311)	14.03	29.50

Table 3.1: The characteristics of the GaAs Bragg reflections studied in this thesis at $\lambda = 0.826$ Å (E=15 keV): the "Reflection" column represents the Miller indices of the crystallographic planes, θ_B is the Bragg angle, β is the angle between the substrate surface and diffraction planes.

rotation was used (see Figure 3.1c) which is the rotation around the surface normal of the goniometer. Because the sample is always perpendicular to the goniometer surface in this geometry, the α goniometer motor defines the angle between the sample surface and incoming beam. On the other hand, for asymmetric reflections, rotations around both α and ω were used where ω is a pMBE motor and rotates the sample around its surface normal. The resulting detector image at the GaAs(111) Bragg peak is shown in Figure 3.3a. Accordingly, the detector image is transformed pixel by pixel into the reciprocal space coordinates, as seen in Figure 3.3b using the following relations [78]:

$$q_z = \frac{2\pi}{\lambda}(\sin\alpha_i + \sin(\alpha_f + c\cdot(i_z - i_{z0}))\cos\nu) \tag{3.2}$$

$$q_y = \frac{2\pi}{\lambda}(\sin\nu) \tag{3.3}$$

$$q_x = \frac{2\pi}{\lambda}(\sin(\alpha_f + c\cdot(i_z - i_{z0}))\cos\nu - \cos\alpha_i) \tag{3.4}$$

$$\nu = c\cdot(i_y - i_{y0}) \tag{3.5}$$

where α_i is the incidence angle of the X-ray beam to the substrate surface, and α_f is the exit angle of the central detector channel specified by the pixel number (i_{y0},i_{z0}). The variables, $i_{y,z}$, are the respective pixel numbers of the detector pixel for which the reciprocal space position is calculated, λ is the X-ray wavelength, and c=arctan(P/L) is a factor converting between pixel number and respective angular offset using the pixel size P and detector distance L.

Using the focusing optics, a few individual NWs were simultaneously illuminated on a growing sample. Usually, only a few of the illuminated NWs fulfilled the diffraction conditions for a given angle setting. That is because the NWs are slightly misoriented respecting to each other. Besides, that is also affected by the divergence of the incident beam. The diffraction experiment using the micrometer-sized X-ray beam is called micro XRD (μXRD) in this thesis. In Figure 3.3b, using μXRD, the Bragg condition for two NWs (NW1 and NW2) are simultaneously fulfilled. The diffuse slope of the Si(111) Bragg peak is observed at $q_z \approx 2$ Å^{-1}; and the GaAs(111) ZB phase is observed at q_z=1.925 Å^{-1}. The signal from tilted NWs lay on a sphere of constant $q = \sqrt{(q_x^2+q_y^2+q_z^2)}$ whose cut with the detection plane is labeled as Debye-Scherrer (DS) ring in Figure 3.3b. Deviation of NW orientation with respect to substrate surface normal is assigned to the tilt angle, β. Note that in Figure 3.3b, the β angle measures the projection of the NW tilt within the detector plane by:

$$\beta = \tan^{-1}\frac{q_y}{\sqrt{q_y^2 + q_z^2}} \tag{3.6}$$

where q_z and q_y are the center of the NW peak along the corresponding reciprocal axes. The two individual NW signals shown in Figure 3.3 are tilted by about 3° respecting to each other. Below each ZB spot, one observes a weaker signal attributed to WZ GaAs(002). For tilted NWs, the difference in the WZ and ZB peak positions is measured

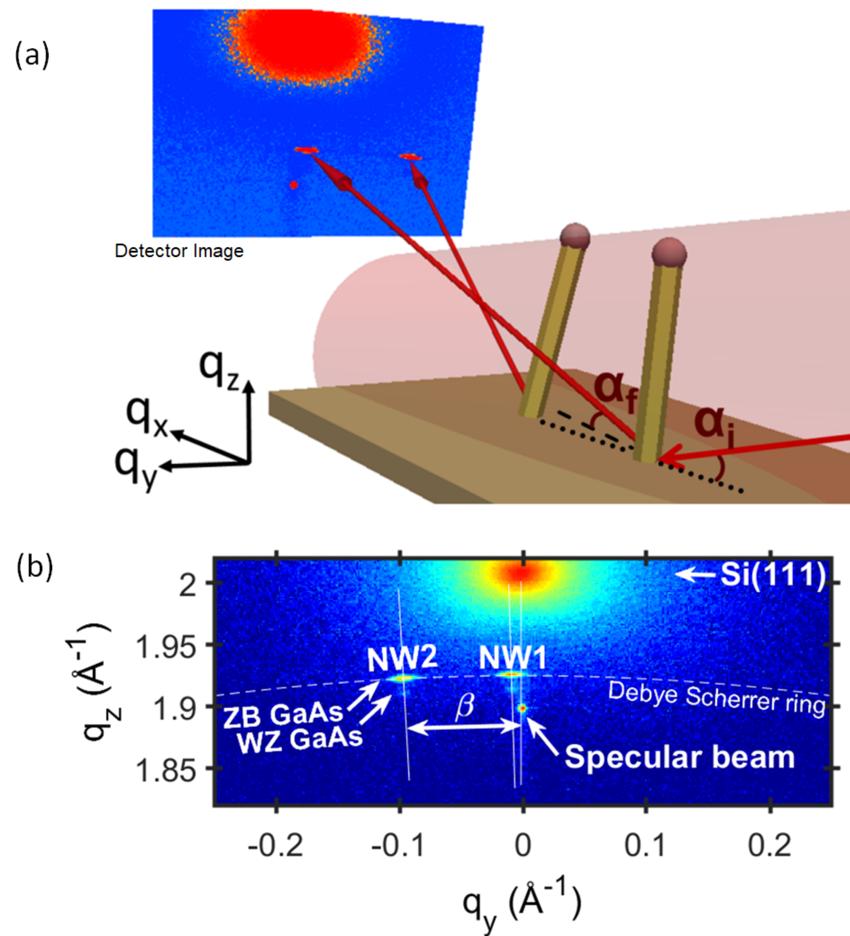

Figure 3.3: (a) Sketch of the experimental geometry of the micro X-ray diffraction experiment. Shown is the focused incoming beam which hits the surface under and angle of α_i. The extent of the beam (indicated by the transparent red area) is such that few NWs are illuminated simultaneously. From the tilted NWs diffracted X-ray beams propagate towards the detector. Outgoing beams have an angle α_f with respect to the surface and hit the detector at different q-positions depending on the tilt of the NW. The reciprocal space axes are indicated. (b) Detailed view of the intensity distribution in the detector plane transformed into the reciprocal space. The shown detector frame is acquired at the vicinity of the cubic (111) Bragg reflections of the Si substrate, including the diffracted signal of the mixed crystal phase GaAs NWs. Note that a logarithmic color scale is used in the plot and two NWs are simultaneously in Bragg condition. Labels define the tilt β along the Debye-Scherrer ring. Below the NW signal, a sharp spot is due to the specular beam of the substrate surface [79].

perpendicular to the DS ring/sphere and is related to the lattice constant mismatch between those phases [66].

3.2 Kinematic theory of X-ray diffraction

For a detailed analysis of the data in the frame of the experiment presented in Section 2.1, the kinematic scattering approximation is sufficient. That is a classical approach to interpret XRD, assuming weak-scattering. That means multiple scattering of X-rays and other diffraction effects that become considerable at large perfect crystals are neglected. The use of kinematic approximation in this thesis is reliable due to the small size of the diffracting objects and leads to a considerable simplification as compared to the dynamical theory of XRD [80]. Here, incoming X-ray plane wave is scattered at the NW only by elastic Thomson scattering. From the perspective of quantum mechanics, under the mentioned conditions, the Born approximation is valid, and the scattering event is a mere perturbation of the incoming wave. In the following, a brief breakthrough to the kinematic theory of XRD is described.

Reciprocal lattice

A 3D Bravais lattice is represented by $\overrightarrow{R} = n_1\overrightarrow{a_1} + n_2\overrightarrow{a_2} + n_3\overrightarrow{a_3}$, where $\overrightarrow{a_i}$ are the primitive vectors of the real space and n_i can be any integer [63]. Suppose that all the lattice points from a crystal with a Bravais lattice of $\overrightarrow{R}$ illuminate identical spherical waves. A linear combination of the spherical waves can be expressed as $f(\overrightarrow{r}) = e^{i\overrightarrow{G}.\overrightarrow{r}}$ at an arbitrary position, $\overrightarrow{r}$, in space [81]. At an infinitely large crystal, due to the periodicity, we have $f(\overrightarrow{r}) = f(\overrightarrow{r} + \overrightarrow{R})$ which follows:

$$e^{i\overrightarrow{G}.(\overrightarrow{R}+\overrightarrow{r})} = e^{i\overrightarrow{G}.\overrightarrow{r}} \longrightarrow e^{i\overrightarrow{G}.\overrightarrow{R}} = 1 \longrightarrow \overrightarrow{R}.\overrightarrow{G} = 2\pi m. \tag{3.7}$$

From a mathematical point of view, an infinite number of $\overrightarrow{G}$ vectors satisfy equation 3.7. The $\overrightarrow{G}$ vectors are related to $\overrightarrow{R}$ vectors as following:

$$\overrightarrow{G} = G_1\overrightarrow{a_1^*} + G_2\overrightarrow{a_2^*} + G_3\overrightarrow{a_3^*}, \tag{3.8}$$

$$\overrightarrow{a_1^*} = 2\pi\frac{\overrightarrow{a_2} \times \overrightarrow{a_3}}{\overrightarrow{a_1}.(\overrightarrow{a_2} \times \overrightarrow{a_3})}, \tag{3.9}$$

$$\overrightarrow{a_2^*} = 2\pi\frac{\overrightarrow{a_3} \times \overrightarrow{a_1}}{\overrightarrow{a_2}.(\overrightarrow{a_3} \times \overrightarrow{a_1})}, \tag{3.10}$$

$$\overrightarrow{a_3^*} = 2\pi \frac{\overrightarrow{a_1} \times \overrightarrow{a_2}}{\overrightarrow{a_3}.(\overrightarrow{a_1} \times \overrightarrow{a_2})}, \tag{3.11}$$

$$\overrightarrow{a_i} \cdot \overrightarrow{a_j^*} = 2\pi\delta_{ij}, \tag{3.12}$$

where $\overrightarrow{G}$ is the so-called reciprocal lattice and G_i is any integer; $\overrightarrow{a_1^*}$ are called the primitive vectors of the reciprocal lattice; δ_{ij} is Kronecker delta function which is 1 for $i = j$, and 0 for $i \neq j$.

X-ray diffraction from a large perfect crystal

Within the kinematic theory of XRD, when an X-ray beam hits a single free electron, re-emission of a spherical wave with the same frequency takes place. The electrons around the nucleus of an atom are considered as charge distribution cloud that is defined by a density function, $\rho(\overrightarrow{r})$. Here, the integration of the charge density, $\rho(\overrightarrow{r})$, in the whole space gives the number of electrons which refers to the atomic number, Z, in the periodic table of elements. The charge in space at position $\overrightarrow{r}$ is $-e\rho(\overrightarrow{r})dr$. Using this approach, the scattering amplitude from a single atom should be weighted by a phase factor, $e^{i\overrightarrow{q}\cdot\overrightarrow{r}}$, where $\overrightarrow{q}$ is the momentum transfer wave-vector as shown in Figure 3.2a. Scattering from a whole atom is expressed by the form factor, which is defined as:

$$f(\overrightarrow{q}) = \int \rho(\overrightarrow{r})e^{i\overrightarrow{q}\cdot\overrightarrow{r}}dr = \begin{cases} Z & |\overrightarrow{q}| \to 0 \\ 0 & |\overrightarrow{q}| \to \propto \end{cases} \tag{3.13}$$

where $|\overrightarrow{q}|$ is the length of the momentum transfer wave-vector. In a solid, when hit by X-rays, several atoms simultaneously re-emit spherical waves, and thus, a description of the wave propagation in space can be made by summing the spherical waves in the whole space. Here, the amplitude of the scattered wave, $A(\overrightarrow{q})$, at large detection distances (D) can be approximated by [82]:

$$A(\overrightarrow{q}) = \frac{r_0 P A_0 e^{ikD}}{D} \int \rho(\vec{r})e^{i\overrightarrow{q}\cdot\overrightarrow{r}}d\vec{r}, \tag{3.14}$$

where r_0 is the classical electron radius, P is the polarization factor relating to the scattering geometry, and A_0 is a constant. It is worth noting that the integration in this equation is within the coherently illuminated solid. It can be seen in equation 3.14 that the amplitude of the scattered wave is proportional to the Fourier transform of

the solid's electron density. It can be shown that the Bragg's condition in equation 3.1 can be rewritten in equation 3.15 for an infinite, defect-free crystal (within the 1st order Born approximation) neglecting multiple scattering and assuming a full coherent scattering [83].

$$\overrightarrow{R} \cdot \overrightarrow{q} = 2\pi m. \tag{3.15}$$

Equation 3.15 relates the momentum transfer wave-vector ($\overrightarrow{q}$) to the Bravais lattice ($\overrightarrow{R}$). By comparing equations 3.15 and 3.7, it is deduced that whenever the momentum transfer vector is equal to any of the reciprocal lattice vectors ($\overrightarrow{q} = \overrightarrow{G}$), a Bragg peak is expected. Ideally, any deviation from the absolute positions of the reciprocal lattice points will give zero intensity due to the destructive interference of the scattered waves.

The vector variable, $\overrightarrow{r}$, can be substituted by a sum of vectors $\overrightarrow{r_{cell}} + \overrightarrow{r_n} + \overrightarrow{r'_n}$ in equation 3.14, where $\overrightarrow{r_{cell}}$ is the position of the unit cells in the solid, $\overrightarrow{r_n}$ is the position of the n$^{\text{th}}$ atom within the unit cell, and $\overrightarrow{r'_n}$ is electron distribution around the n$^{\text{th}}$ atom in the unit cell. Accordingly, the amplitude of the scattered wave is written as:

$$A(\overrightarrow{q}) = F(\overrightarrow{q}) \cdot \sum_{cells} e^{i\overrightarrow{q}\cdot\overrightarrow{r_{cell}}}, \tag{3.16}$$

$$F(\overrightarrow{q}) = \sum_{n} f(\overrightarrow{q}) e^{i\overrightarrow{q}\cdot\overrightarrow{r_n}}, \tag{3.17}$$

where $f(\overrightarrow{q})$ is the atomic form factor (see equation 3.13), and $F(\overrightarrow{q})$ is the structure factor of the solid. According to the kinematic approach, XRD experiment measures the squared modulus of the amplitude; and the structure factor indicates the strength of different Bragg peaks. The term, $\sum_{cells} e^{i\overrightarrow{q}\cdot\overrightarrow{r_{cell}}}$, is called the lattice sum or geometrical factor which represents the locations of the allowed (Bragg/Laue) diffraction peaks in a solid. The resulting structure factors for the GaAs ZB and WZ structures, which are cubic and hexagonal unit cells presented in Section 2.1, are worked out in equations 3.18 and 3.19, respectively:

$$F\begin{matrix} ZB \\ hkl \end{matrix} = 4. \begin{cases} f_{As}(q) + f_{Ga}(q) & h,k,l \text{ even}; h+k+l = 4n;\ n \in \mathbb{Z} \\ f_{As}(q) - f_{Ga}(q) & h,k,l \text{ even}; h+k+l \neq 4n;\ n \in \mathbb{Z} \\ f_{As}(q) \pm f_{Ga}(q) & h,k,l \text{ odd} \\ 0 & \text{else} \end{cases}, \tag{3.18}$$

$$F\begin{matrix} WZ \\ hkl \end{matrix} = (1 + e^{i(2\pi/3)(2h+k)}e^{i\pi l})(f_{As} + f_{Ga}e^{i(3\pi/8)l})), \tag{3.19}$$

where $f_{As}(\overrightarrow{q})$ and $f_{Ga}(\overrightarrow{q})$ are the form factors of As and Ga.

X-ray diffraction from nanostructures

So far in this section, an infinitely large and perfect crystal is discussed. Natural effects such as finite size or the surfaces on a crystal can lead to a modification of the shape of the Bragg peaks compared to that measured from an infinite crystal [84]. Moreover, any deviation from the expected atomic distances can alter the angular position of the Bragg reflections, e.g., strain within a crystal or crystallographic defects [17]. The amplitude of the scattered wave can be recalculated typically by taking additional functions into the perfect crystal calculations. For example, for a strained finite crystal, such as a strained NW, equation 3.14 can be rewritten as:

$$A(\vec{q}) = \frac{r_0 P A_0 e^{ikD}}{D} \int \rho(\vec{r})\Omega(\vec{r})e^{i\overrightarrow{q}\cdot(\overrightarrow{r}+\overrightarrow{u(\vec{r})})}d\vec{r}, \tag{3.20}$$

where $\Omega(\vec{r})$ is the shape function which is one within the nano-object but zero elsewhere. The so-called displacement field function, $\overrightarrow{u(\vec{r})}$, defines displacement of the atoms with reference to their expected positions at a perfect crystal. The integrated diffracted intensity of a nano-object at a particular reciprocal lattice point is [85]:

$$I_{\overrightarrow{G}}(\overrightarrow{\triangle q}) = \frac{\left|F(\overrightarrow{G})\right|^2}{V^2} \left| \int \Omega(\vec{r})e^{i\overrightarrow{G}\cdot\overrightarrow{u(\vec{r})}}e^{i\overrightarrow{\triangle q}\cdot\overrightarrow{r}}d\vec{r}\right|^2 \tag{3.21}$$

where $\overrightarrow{\triangle q}$ represents the vicinity of the $\overrightarrow{G}$ Bragg reflection point, and V is the volume of the scattering object. For a strain-free finite-size object like a NW, the scattered amplitude is given by the Fourier transform of the object shape ($\overrightarrow{u(\vec{r})} = 0$ in equation 3.21). In Figure 3.4, the intensity distribution around the Bragg peak of a NW is simulated perpendicular to the NW growth direction. The cross-section of the MBE grown self-catalyzed GaAs NWs is normally hexagonal. Accordingly, the intensity distribution of the NW in the vicinity of a reciprocal lattice point is modeled by the Fourier transform of a 2-dimensional hexagon of constant electron density (see Figure 3.4a). The squared modulus of the Fourier transform is shown in Figure 3.4b, which is proportional to the expected intensity distribution around the reciprocal lattice points. In this work, q_z is

the scattering component perpendicular to surface; q_x and q_y are the scattering components parallel to surface. Characteristics of scattered objects (the nano-objects) in real space are extracted from the diffraction pattern of the object (reciprocal space). For example, the hexagonal shape is deduced by the angles between the fringes (see Figure 3.4b); and the size of the facets can be deduced from the line profile along each of the six size oscillation fringes (truncation rods). The fwhm (full width at half maximum) of the main Bragg peak is correlated to the scattering object's diameter, D (see Figure 3.4a) by

$$\text{fwhm} \approx \frac{1.68 \cdot \pi}{D}. \tag{3.22}$$

That is approximated by fitting a Gaussian function (see the red curve in Figure 3.4c). As seen in Figure3.4d, the spacing between the maxima along the truncation rod is equal to ${}^{2\pi}/_{D}$. In the experiments presented in this thesis, the size oscillation fringes are lost in the background of the signal, and therefore, the fwhm of the diffraction peaks from individual nano-objects is taken as the basis for extracting the objects' sizes [2].

[2]All the data processing in this thesis are performed by MATLAB programming language. The analysis includes, for example, the transformation of the angular diffractometer coordinates into the reciprocal space, data plotting and visualization, and curve fitting [86].

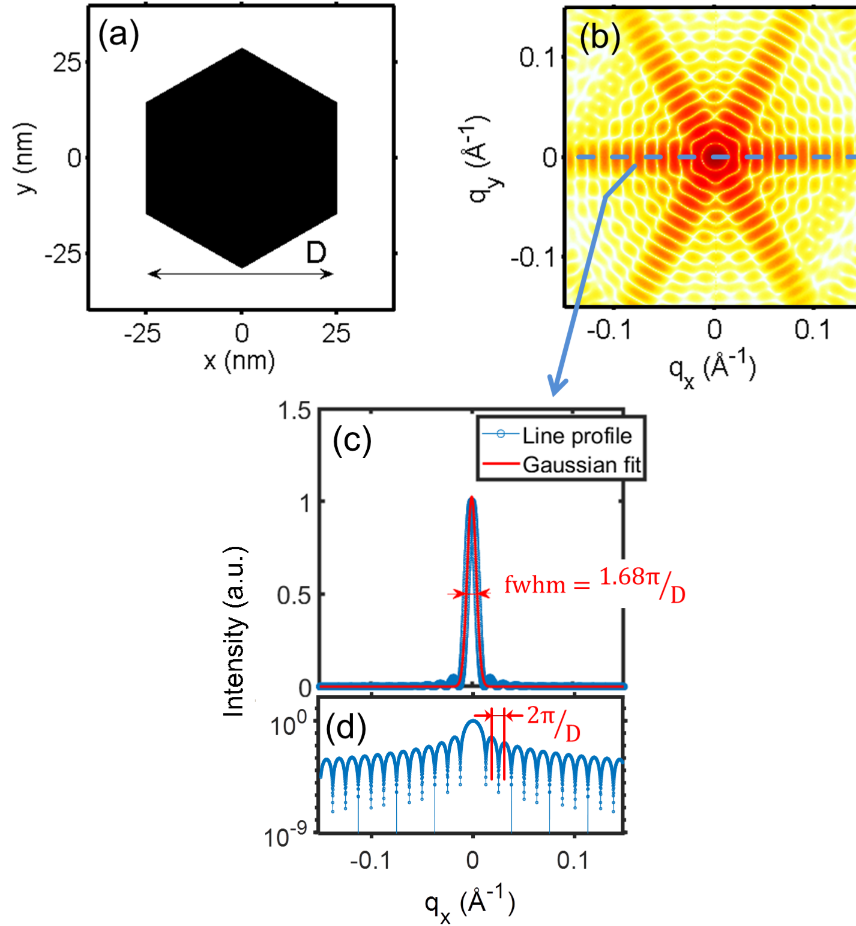

Figure 3.4: Panel (a) shows a hexagon with an arbitrary diameter (D) of 50 nm. Panel (b) is the squared modulus of the Fourier transform of the hexagon. The intensity distribution is depicted in a logarithmic color scale. In an XRD experiment from NWs with hexagonal prism shape, the intensity distribution around a Bragg reflection at the q_x-q_y plane ideally looks like panel b. Note that q_x and q_y are the scattering components parallel to surface. Panel (c) is a line profile along one of the truncation rods (size oscillation fringes) as indicated in panel (b). The fwhm of the central peak in panel c is extracted by a Gaussian fit function as indicated, where D is related to fwhm as indicated. Panel (d) is similar to panel c but with a logarithmic y-axis. Here, the size oscillation fringes are more visible, and the spacing between the consecutive maxima is related to D as indicated.

Chapter 4

MBE GaAs nanowire growth

In the last decades, the growth of self-catalyzed GaAs NWs on Si substrates has been significantly improved [27, 31, 33, 34, 38, 87-91]. Generally, the Si substrates are either covered by a thin Si oxide layer (∼1 nm native oxide) or a relatively thicker Si oxide (e.g., $>$ 15 nm thermal oxide). Growth on native Si oxide substrates takes place at random positions. Here, because of the complexity of the various mechanisms involved, there is still a demand to control the characteristics of the grown NWs [34, 35, 92]. The epitaxial NW growth on thermal oxide is normally fully suppressed, opening up the possibility to selectively remove the oxide to define the position and characteristics of NW growth. Substrate patterning has been so far the best method to define the growth of self-catalyzed GaAs NWs onto Si [91, 93, 94]. However, patterning techniques require a high demand in terms of equipment, expertise, and time. In this chapter, we report on the growth of self-catalyzed GaAs NWs on Si(111) using MBE. Our studies present attempts to tackle the demands mentioned above toward future mass production of NW growth on both native oxide and patterned substrates. In particular, we introduce fundamentally simple approaches, which are advantageous for applications in future engineering.

NW growth experiments were performed in March 2014 to Dec 2016 for the first time at the UHV laboratory in ANKA (the former synchrotron facility) at Karlsruhe Institute of Technology (KIT) using the pMBE chamber. The growth optimizations on native oxide substrate were continued till May 2015 by more than 80 growth runs, and followed by growth runs on patterned substrates till the end of 2016 by more than 40 growth runs. Our growth results were partly summarized in a Ph.D. thesis [95], and additional data are presented in this thesis. Moreover, the successful growth protocols resulted in several scientific papers, e.g., refs. [58, 79, 96]. We present the results of

several additional annealing runs performed in 2015-2017 using the pMBE chamber in Chapter 6.

In Section 4.1, we propose a new strategy to control the homogeneity of growth on the native oxide surface of Si. By this method, the statistical distribution of the length and diameter of the upright grown NWs decreased to about 3−6% of their averaged values. Besides, the ratio between the NWs and parasitic islands (PIs) significantly increased (> 30). The results of this section are in review for publication [Paper I].

In Section 4.2, an innovative lithography-free patterning method is introduced for the NW growth. Here, a FIB is employed to pre-define the position of the NWs on Si substrate. This patterning approach is detailed (for the first time) for reproducible high-yield (> 80 %) growth of self-catalyzed GaAs NWs. The results of this section are published in [97].

4.1 GaAs growth on Si native oxide

On silicon native oxide substrate, the most common approach to grow self-catalyzed GaAs NWs is by the simultaneous supply of As and Ga molecular beams. In this approach, one could tune the NW characteristics on a given sample by altering the substrate temperature, and source material fluxes. Therefore, NW density ($0.01 - 1$ μm^{-2}) and diameter ($10 - 200$ nm) can be manipulated in wide ranges. However, by this approach, it seems not possible to modify the mentioned NW characteristics independently; and normally, the number ratio between the NWs and PIs (NW/PI) can not be significantly improved [30, 32, 34, 98, 99, 100]. The PIs are undesired objects growing together with the self-catalyzed NWs on Si native oxide [101, 102].

It is widely known that natural openings (pinholes) on native Si oxide are the preferential nucleation sites for Ga and GaAs material [24]. Besides the growth optimization, another degree of freedom to manipulate the NW growth characteristics is by controlling the size of the oxide pinholes. To this end, in literature, it is suggested to treat the native Si oxide substrates prior to the growth by the following general approaches:

i) The oxide layer is thinned by wet etching or annealing. In this way, aside from a planar oxide removal, the oxide pinholes are largely affected [24, 88, 95, 101, 102].

ii) The oxide is removed at selective positions by a two-step process. First, nano-objects (GaAs crystals or Ga droplets) are grown on a substrate. The grown nano-objects interact with the oxide [103], which leads to the development of new/bigger nano-cavities. Second, by a high-temperature annealing step, the grown objects are

removed [35, 88, 87, 96]. In this way, the oxide layer is mostly affected at positions of the nano-objects (see ref. [88] for an atomic force microscopy analysis of the Si oxide surface morphology in this process). Homogeneity of the developing surface nano-cavities (pinholes) might be closely related to the growth characteristics of the nano-objects (e.g., density and size). Because of the improvements in manipulating the mentioned characteristics of the nano-objects, approach (ii) seems to be more controlled as compared to approach (i). The authors in refs. [87, 96] performed the substrate conditioning by growth and annealing of GaAs crystals. Tauchnitz et al. [88] performed Ga droplet positioning and removal. Koivusalo et al. have combined growth and removal of both Ga droplets and GaAs crystals resulting in a significant narrowing of the NW length distribution and also suppression of the PI nucleation [35]. However, in their case, an intermediate exposure of the substrates to air is used. The authors in ref. [88] have presented an attempt to achieve homogeneous NW sizes without exposing the NWs to air. However, their strategy suffers from consumption of a significant amount of source material. The latter is, in fact, the general disadvantage of this category of surface conditioning approach (e.g., in refs. [35, 87, 88, 96]) which is unfavorable toward industrial mass production.

As an alternative to surface conditioning, the NW growth characteristics can be controlled by performing a two-step growth protocol: first, nano-objects (Ga droplets or GaAs nano-objects) are pre-deposited; and second, selective growth of NWs takes place at the pre-deposited nano-objects. Following the literature, such approaches can be divided into two categories:

i) Relatively small GaAs islands are grown. Those nano-objects act as nucleation sites for a following selective nucleation of Ga droplets and a consequent NW growth [32, 104].

ii) Ga droplets are pre-deposited on the Si oxide substrate at high Ga fluxes. Then the Ga flux is decreased for NW growth to minimize further nucleation on the substrate [92].

In both latter categories, one could manipulate the size and number density of the NWs independently. The density of the NWs is related to the density of the pre-deposited nano-objects. The control in the density of the NWs can prevent shadowing effects [105], which is an essential factor in core-shell NWs. Further, one could achieve a high homogeneity in NW length and diameter.

The Ga pre-deposition in ref. [92] is, in principle, similar to the presented approach in this thesis, although the authors made the report in 2017 (2 years after my experiments). Küpers et al. concentrated on decreasing Ga flux to control nucleation. Nevertheless, a

report on the interplay of substrate temperature and Ga flux is missing. An increased substrate temperature can similarly prevent nucleation of the material on the substrate. We report that growth above a critical temperature of 580 ± 10 °C is advantageous due to the better interaction of Ga with the silicon oxide. Accordingly, a significant improvement in the NW/PI ratio is achieved. In terms of length homogeneity, the presented results shown in this section are comparable with those presented in refs. [35, 92]. Also, the diameter and number density of the NWs could be controlled, which are likewise in high demand [32, 35, 88, 92, 104]. Using the new insights in this thesis, the advantage as compared to the literature is that i) no ex-situ intermediate step of exposure to air is made; ii) a considerably lower amount of source material is consumed; iii) a technically simple approach is made. These are fundamental milestones toward future mass production.

This section is organized as follows. In Section 4.1.1, based on in-situ RHEED method, we introduce the MBE system calibrations and qualitative characterization of GaAs NW growth. In Section 4.1.2, sample preparation procedures are explained. In Section 4.1.3, NW growth on native oxide is presented. In particular, first, based on experimental results, the limitations of the most common approach of GaAs NW growth (simultaneous supply of Ga and As) is discussed. The alternative method is then experimentally worked out. That involves homogeneous Ga pre-deposition and a subsequent controlled NW growth from the deposited Ga droplets. In Section 4.1.4, further analysis of the samples is presented to highlight that the epitaxial growth and density of the over-grown GaAs nano-objects of different types have been highly controlled. In Section 4.1.5, we conclude the findings in this part.

4.1.1 Reflection high-energy electron diffraction

MBE calibration by RHEED

In this work, the pMBE chamber was transferred multiple times from Karlsruhe to synchrotron sites. During the transfer of the chamber, the system was not disassembled, and the vacuum was kept. However, due to vibrations during the transfer, few preinstalled parameters may change. Accordingly, the substrate temperature, as well as the molecular beam fluxes, had to be re-calibrated. Additionally, an inevitable system bake-out was required if the vacuum broke during the transfer.

Temperature/flux calibrations in the MBE are usually performed by means of in-situ RHEED monitoring. Here, the thermal decomposition temperature of a known

epiready native oxide is the basis of the temperature calibration, e.g., 590 ± 10 °C for GaAs oxides. In particular, the RHEED pattern shows pronounced truncation rods from the GaAs surface after removal of the native oxide layer.

Under an excessive arsenic flux, by supplying Ga, a layer by layer growth of smooth GaAs is initiated on GaAs(100) substrate. In this case, the Ga flux determines the 2D growth rate. During the layer by layer growth, the intensity of the RHEED signal at Bragg reflections oscillates. The frequency of the oscillation determines the growth rate of a single ML of planar ZB GaAs(100). By increasing the Ga flux (at initially excessive As), the transition between 2×4 to 4×2 surface-reconstructions indicates the switch from arsenic-rich to gallium-rich incorporation of Ga and As species onto the surface [106, 107]. The latter procedure ascertains the 1 to 1 incorporation of Ga and As atoms for 2D growth and therefore determines the As flux [108]. In this thesis, the fluxes are given in quantities of the material to form GaAs 2D MLs onto the GaAs(100) surfaces at a substrate temperature of 580 °C. Notably, the NW axial growth rate is significantly higher than such equivalent 2D growth rates under similar fluxes. For more detailed information about calibrations see ref. [109].

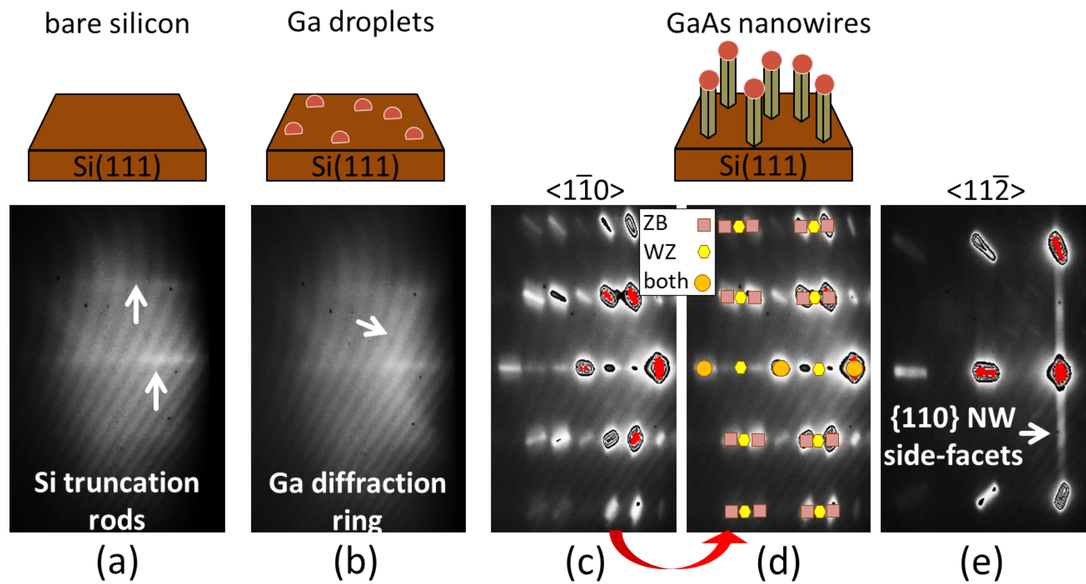

Figure 4.1: The RHEED patterns containing: horizontal streaks from Si(111) truncation rod in panel (a); Ga diffraction ring originating from the Ga droplets on the substrate in panel (b); reflection spots originating from ZB and WZ crystallographic structures in the grown GaAs nano-objects in panels (c—d); vertical streaks originating from the NWs' side-facets in panel (e).

Qualitative characterization of GaAs nanowire growth by RHEED

Back in the 1970s, RHEED was used to follow the growth of GaAs thin films [110, 111]. That is in particular because of surface sensitivity of RHEED were a grazing incidence angle enhances the cross-section of an electron beam with the surface atoms leading to resolving diffraction signal from a single ML of material [111]. Since the 2000s, this technique is employed to study the epitaxial growth of GaAs NWs on Si [112, 113]. For growth experiments reported in this thesis, in addition to the flux calibrations explained above, RHEED was used for in-situ characterization of the growth of Ga and GaAs nano-objects in a qualitative manner. To do so, a monochromatic electron beam (25 KeV) with about 100 μm cross-sectional width illuminated the samples at a grazing angle of incidence. The diffracted electron beam illuminated a phosphorous screen (fluorescence effects) videotaped by a camera. Here, the mean growth characteristics were observed from an about 0.2 square centimeter footprint, illuminating about $10^5 - 10^8$ NWs.

Figure 4.1 illustrates the nano-object characteristics extracted from the RHEED data. The Si substrate covered by a thin oxide layer shows streaks originating from the Si truncation rods [111] as seen in Figure 4.1a (horizontal lines). After deposition of Ga droplets on the surface, a diffraction ring appears [114, 115], as seen in Figure 4.1b. The signal originating from the Ga droplets was visible only if the Ga number density was higher than about $\sim$0.1 μm^{-2} (Ga diameter $>$ 40 nm). This ring can be related to the droplet correlation and form factor peaks in grazing-incidence small-angle X-ray scattering as reported by Wang et al. in ref. [116]. The quantitative analysis of position and shape of the Ga diffraction ring, in principle, provides information about the average size of the Ga droplets and their statistical uniformity [116]. The RHEED spots in Figure 4.1c usually appeared after a few mins of GaAs crystal growth using my growth parameters on native Si oxide. During growth, the RHEED spots evolved at the diffraction angles corresponding to GaAs WZ and/or ZB phase, as indicated in Figure 4.1d. The orientation of the electron beam with respect to the sample in Figure 4.1c−d is along the $<1\bar{1}0>$ crystallographic directions of the Si(111) substrate. Here, the alignment of the GaAs diffraction spots are along the Si truncation rods (compare panels c−d with panel a) indicating that the GaAs overgrown material is epitaxially aligned to the Si substrate. In the case of non-epitaxial growth of the GaAs material with Si, diffraction rings appear (see Figure 4.13). At the $<11\bar{2}>$ azimuths, as shown in Figure 4.1e, vertical streaks appear originating from the NW side facets and indicating a successful NW growth. It is worth mentioning that the NW facets can appear at

different azimuths in other material systems depending on the type of the NW facets, e.g., in GaN NWs, the NW side facets come into view at the $<2\bar{1}.0>_{hex}$ and $<1\bar{1}.0>_{hex}$ azimuths [117].

4.1.2 Sample preparation

The characteristics of the Si native oxide samples were as followed: quarter cuts from 2-inch circular Siltronix Si(111)±0.5° n-doped (Ph) wafers covered with a thin epiready layer of Si oxide. By performing a few growth runs, we found that a typical wafer-cleaning procedure could improve the uniformity of the growth density around the samples. In particular, we performed two rounds of ultrasonic bathing at a frequency of 35 kHz in acetone, isopropanol, and deionized water for 5 min at each solvent. This procedure efficiently removes the micrometer-sized aerosol particles and organic contaminants which stick to the wafer surfaces during processing and transferring of the wafers [118, 119]. Afterward, using nitrogen blowing, water was removed from the substrates. The whole ex-situ sample preparation procedure was performed in a flow box with cleanroom class 5 (manufacturer Laflow). Then the samples were loaded into a pre-heating chamber and annealed at 300 °C for 1 hour in order to remove the remaining water and volatile carbon species.

After transferring the sample to the pMBE chamber, the temperature was ramped up to 660±5 °C, and the sample was annealed for 35 min. Typically, this annealing step is aimed to remove GaAs material from the sample holders. That is required because a previous growth run can deposit crystalline GaAs material on the sample holder which may induce unknown deviations of partial pressures of source material during a next growth run. The temperature of 660°C is about 30°C above the congruent temperature and therefore, the material rapidly evaporate [120, 121]. This was approved by additional experiments where annealing of about 30 min lead to efficient evaporation of grown GaAs crystallites (see Chapter 6).

4.1.3 Nanowire growth

We investigated the impact of several growth parameters on the quality of the growth. The data was acquired basically in years 2014-2015 and selectively presented in this chapter. At the first attempts, after the preparation steps explained above, Ga and As molecular beams were simultaneously supplied. Here, mainly, effects of As flux, Ga

flux, substrate temperature, and growth duration are presented at otherwise optimized preparation/growth parameters. In the next experiments, Ga was pre-deposited before the simultaneous supply of Ga and As. The Ga deposition was controlled, aiming for narrowing the size distribution of droplets. NW growth was followed, endeavoring for suppression of growth between the Ga droplets. It has been reported [34, 101] and observed by us that the NW growth characteristics (e.g., density, sizes, NW/PI ratio) change from wafer to wafer as a result of the deviations of the silicon oxide properties. Accordingly, the NW growth runs were repeated by nominally identical growth protocols to verify the reproducibility.

Nanowire growth by simultaneous supply of As and Ga sources

After the ex-situ and in-situ preparation steps (Section 4.1.2), As and Ga are simultaneously supplied to initiate the NW growth. The influences of either the As or Ga fluxes were investigated by keeping the other flux as well as the substrate temperature (570±5 °C) and growth time (1 h) constant. The results of a few selective growth runs are shown in Figure 4.2. Here, panel a and b show the length and diameter evolution of the NWs as a function of As and Ga flux rates, respectively. The corresponding SEM images are shown in panels A−C, and D−F related to panels a and b, respectively. By increasing the As flux, the length of the NWs increases (see Figure 4.2a and A−C). Such a dependency typically suggests the VLS mechanism of NW growth as reported in ref. [100]. At the same time, the maximum As flux results in 100% upright orientation of the grown NWs (cf. Figure 4.2A, B, C). Russo-Averchi et al. have reported that small V/III ratios result in the occurrence of 3D twinning and a large percentage of discrete growth directions in MBE based self-catalyzed GaAs NWs on Si [30]. They reported that the NW growth with 100% percentage upright orientation takes place only at the optimal growth parameters, which highlights the achievement in Figure 4.2C. In the present work, the average diameter of the NWs within the error bars does not show a significant change by increasing the As rate similar to ref. [100]. In a VLS mechanism of NW growth, first Ga droplet forms on the substrate; and by the influx of As atoms into the droplet, supersaturation takes place. Finally, GaAs nucleates preferentially at the heterogeneous sites (the solid substrate surface) [24, 89, 122]. The initial size of the droplet determines the initial NW diameter that is grown. The authors in refs. [90, 95] predict a decreasing NW diameter by increasing the As flux. That is likely because of the accelerated supersaturation rate of the Ga droplet at a higher As influx, meaning that the Ga droplet has less time to grow after Ga droplet nucleation (decreased

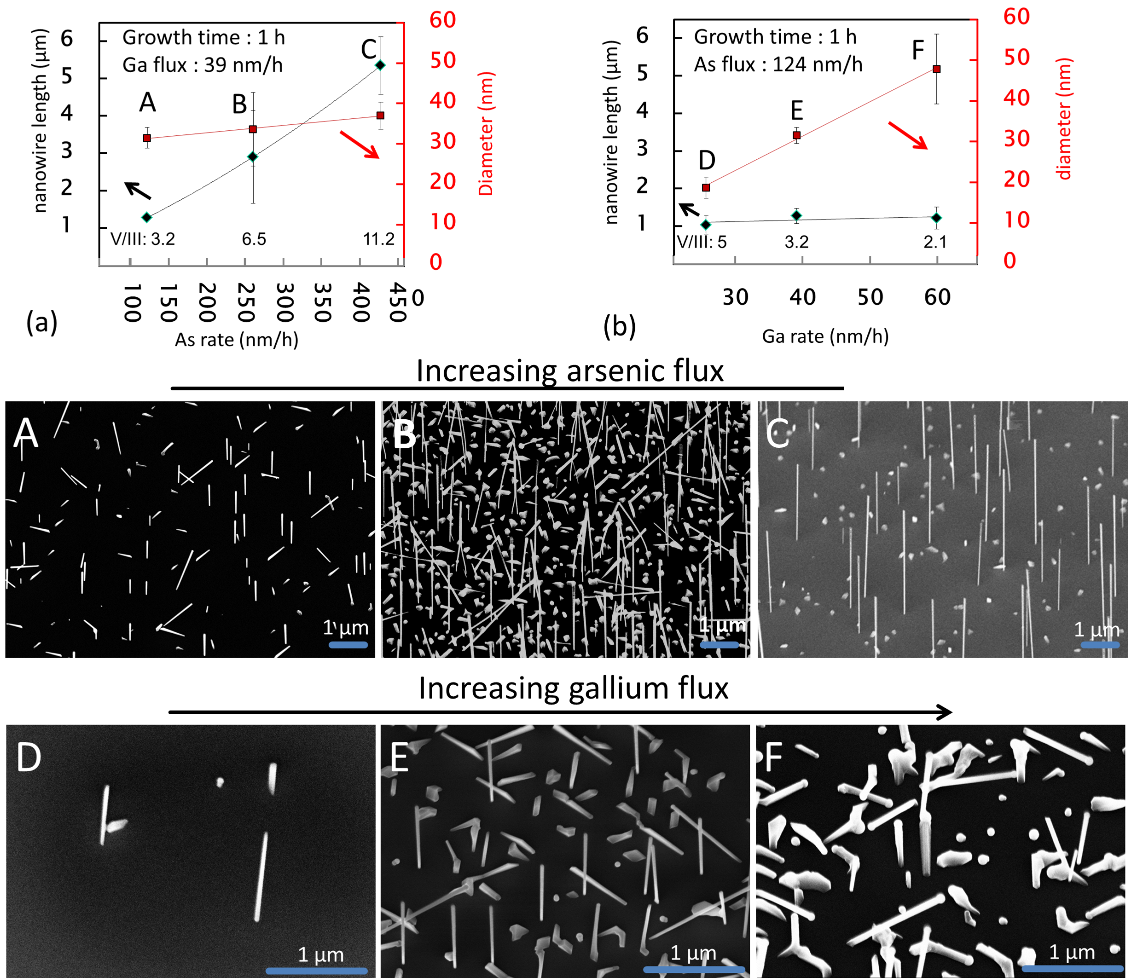

Figure 4.2: The evolution of the NW length and diameter as a function of As flux in panel (a) and Ga flux in panel (b) by keeping the other flux constant. The growth temperature and duration are constant at 570±5 °C and 1 hour, respectively. A−F show SEM micrographs taken at a 30° tilted substrate. SEM images in panels A−C and D−F correspond to data points in panels a and b, respectively.

incubation time). However, the interplay of the radial growth at an extended growth duration can not be neglected in self-catalyzed VLS growth [58, 123]. Therefore, the proposed trend in refs. [90, 95] explains the initial stages of NW growth. In contrast, the probability of incorporation of diffusing Ga adatoms onto the side-walls of the NW can increase (enhanced radial growth) by increasing the As flux [89, 124]. Therefore, the interplay of the two mentioned mechanisms can explain the tendency of the observed diameter evolution in Figure 4.2a. In other words, the decreased initial NW diameter and increased radial growth rate has flattened the diameter curve in Figure 4.2a. In Figure 4.2b, by increasing the Ga flux from about 25 to 60 nm/h, the NW diameter

increases whereas the NW length does not change within the error bars. That is in agreement with the findings in refs. [90, 100]. As explained above, the initial diameter of the NW is directly related to the supersaturation time; and at a constant As flux, the increasing Ga influx into the Ga droplet (stable nuclei) increases the initial diameter of the NW [100]. On the other hand, the axial growth rate is affected mainly by arsenic supply and therefore stays unchanged in the present case.

The effects of the substrate temperature on the NW growth can be seen in Figure 4.3. The substrate temperature changes within a range of 550±5−630±5 °C at otherwise constant conditions (growth duration 1 hour, Ga flux 39 nm/h, As flux 124 nm/h). The overall deposited material decreases by increasing the substrate temperature (cf. Figure 4.2A−D). Spirkoska et al. have reported that above a temperature of 570 °C, the sticking coefficient of GaAs material on Si oxide drastically decreases [125]. That explains the abrupt decrease in the growth density above 570±5 °C in Figure 4.2. On the other hand, by increasing the growth temperature, both NW length and diameter decrease, as shown in Figure 4.3. This can be related to the degrading flux efficiency (both As and Ga), which is in agreement with the results in Figure 4.2. The NW/PI ratio increases from 1 at a growth temperature of 550±5 °C up to 3 at 590±5 °C.

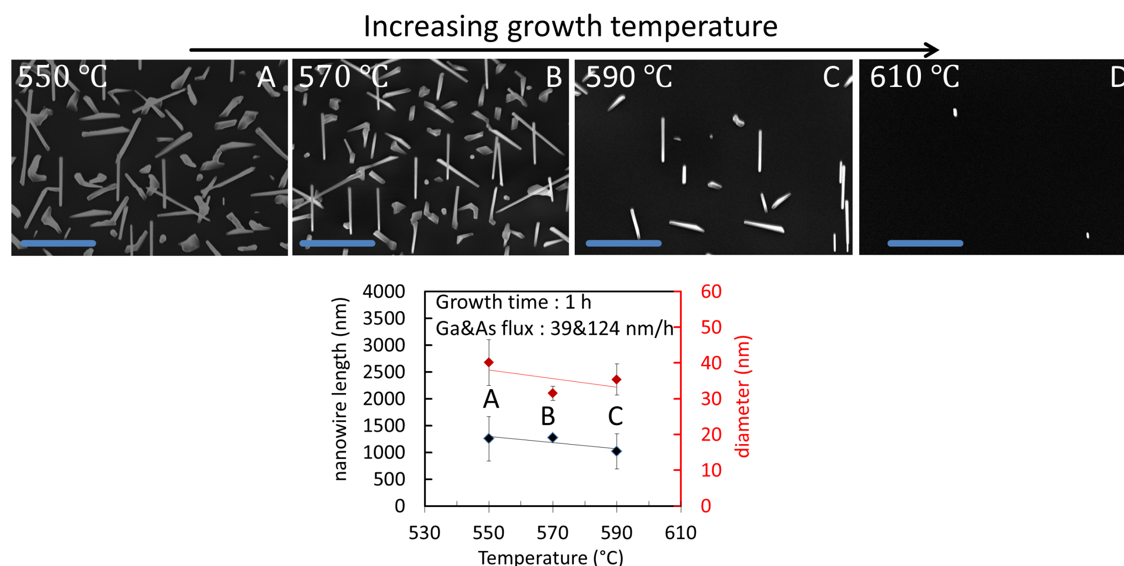

Figure 4.3: The influence of the growth temperature on the growth characteristics (growth duration of 1 h, Ga&As flux of 39&124 nm/h). A−D are the aftergrowth SEM micrographs at 30° tilted substrate where the scale bars are 1 μm. The plot (below) shows the evolution of the length and diameter of the upright NWs in A−C. The analysis of the density of the grown objects on the samples is shown in Table 4.2.

The evolution of the NW characteristics along growth was investigated by extending the growth duration up to different growth times. The time series studies were performed at different growth conditions. After NW growth, the samples were characterized by SEM, which consistently showed that both the diameter and length of the NWs increase during the growth i.e., radial and axial NW growth. However, because of the large error bars at the data points due to NW size distributions, the actual radial/axial growth dynamics could not be extracted (similar to that in Figure 4.2). In the following, one example is presented in order to show the interesting a priori information from such time series studies. At Ga and As fluxes of 25 and 195 nm/h, and growth temperature of 570±5 °C, the first GaAs signal in RHEED appeared after about 2.5 min of growth with no indication of NW side-facet streaks (see Figure 4.1e). This signal can be originated from the initial stages of growth (few MLs) from the NWs or PIs. By extrapolation of the NW length curve as a function of time, an incubation time of 3.5±0.6 min was revealed for the NW growth. That means that the critical supersaturation of the Ga droplets occurs after about 3.5 min of growth resulting in the crystallization of the GaAs. The average diameter of the NWs is calculated to be about 20±4 nm at the incubation time. That is calculated by extrapolation of the diameter vs. time curve. In other words, this corresponds to the final size of the Ga droplet before supersaturation under the given experimental conditions. By the time series studies at different growth conditions, it was observed that the incubation time and the initial diameter of the NWs were affected by As and Ga fluxes, as discussed above in Figure 4.2.

To conclude, at the presented growth scheme (simultaneous Ga and As supply), the initial diameter of the NW depends on Ga and As fluxes. By growth optimizations, we could elaborate a growth window with controlled NW size and density (not independently in this approach). Moreover, 100% of uprightly standing NWs is achieved at high V/III ratios. Nevertheless, the growth of PIs could not be suppressed. The quality of the presented results is comparable with previous reports in the literature using the same approach of growth [30, 34, 95, 100]. To further control the NW growth, an additional Ga pre-deposition step was implemented. That could manipulate the NW diameter, independent from the Ga and As fluxes, and manipulate the NW density, independent from the growth temperature. Moreover, PI growth could be significantly suppressed.

Ga pre-deposition

After the preparation steps (Section 4.1.2), the substrate temperature was stabilized at a temperature within 600±5−620±5 °C for Ga pre-deposition. Here, only Ga was supplied for a duration of 10 min. At a substrate temperature of 610±5 °C, Ga was supplied with the fluxes of 25, 39, and 59 nm/h. The resulting density and diameter of the deposited Ga droplets were 0.03 ± 0.01 μm^{-2} and 48 ± 5 nm, respectively, at a Ga flux of 59 nm/h. Below this Ga flux, the deposition was negligible. Based on the experimental and theoretical reports, Ga droplet formation on Si in vapor phase epitaxy has several steps: i) formation of atomic Ga (adatoms) from molecular Ga (gas) on the substrate, ii) surface diffusion of the Ga adatoms, iii) Ga droplet formation [126, 127, 128]. The highest Ga flux (Ga vapor pressure) results in an increasing adatom concentration on the Si surface. In other words, the reaction, $Ga_{gas} \longleftrightarrow Ga_{adatom}$, goes to the right side by increasing Ga_{gas}. The formation probability of a stable liquid droplet nucleus increases by increasing the adatom concentration on the surface [129], which qualitatively explains the higher formation probability of the Ga droplets at higher Ga fluxes. It is reported that increasing the temperature above 600±5 °C can drastically affect the overall volume of deposited Ga [125]. Therefore, for Ga pre-deposition at higher temperatures, significantly higher Ga fluxes may be required.

As explained above, the pre-annealing step was used to clean the surface and stabilize the pressure. However, during our experiments in 2014−2015, we speculated that an annealing step could also condition the surface. Therefore, the effects of the pre-annealing step prior to Ga pre-deposition are studied at a temperature of 660 °C by varying the annealing duration to 1, 17, and 35 min. The results of the following Ga deposition were compared with the results obtained from a sample without a pre-annealing step. It was discovered that a pre-annealing step significantly increases the density of the deposited Ga droplets (a factor of $10 - 20$). After our finding, in 2017, Tauchnitz et al. [88] published a study about this effect, which is in agreement with our results. In the latter ref., the authors studied the Si oxide surface utilizing atomic force microscopy and X-ray photoemission spectroscopy. They showed that at a fixed annealing time of 30 min within a temperature range of 690 to 770 °C, the morphology of the surface changes without altering the oxide chemistry. That could be attributed to the presented annealing conditions where the openings on the Si oxide are increasingly influenced by prolonged annealing times. On the other hand, the size distribution of the Ga droplets was narrowed as a result of pre-annealing. That suggests an enhanced homogeneity in the distribution of the oxide openings [24].

Pre-deposition of the Ga droplets at higher substrate temperatures showed a narrower droplet size distribution (see Figure 4.4) [1]. That can be explained by the enhancement of Oswald ripening at higher temperatures [127]. In simple words, a higher temperature provides the activation energy for the diffusion of the Ga adatoms. Here, the bigger droplets are more stable than the smaller ones because of the decreasing number of dangling bonds at the surface atoms in bigger droplets. Therefore, diffusion of Ga adatoms occurs from the smaller droplets toward the bigger ones. That results in an eventual fading of the small droplets in favor of larger ones leading to larger droplet sizes with a more homogeneous size distribution.

Annealing of the droplets results in even better diameter homogeneity as also observed in ref. [92]; and it provides a longer reaction time for interaction of Ga with Si oxide along with enhanced Ga etching above a temperature of 580±5 °C [103, 130]. The latter facilitates the epitaxial connection of GaAs nano-objects with Si substrates, which decreases the formation energy of GaAs crystals.

In order to manipulate the Ga droplet size, it is suggested to change the pre-deposition time as reported in refs. [92, 131], which was outside our scope.

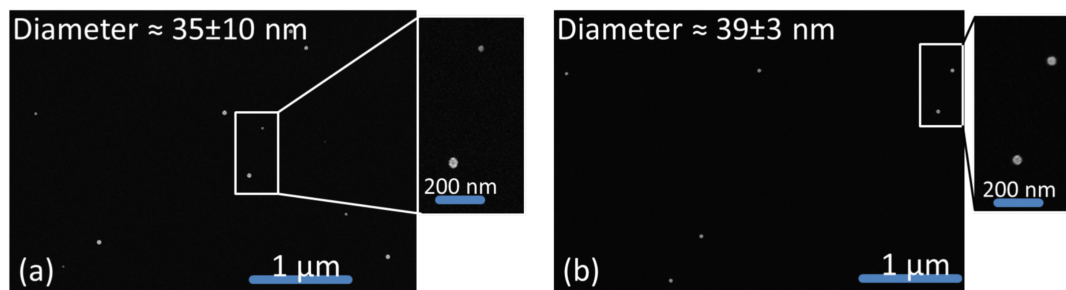

Figure 4.4: Ga droplet pre-deposition on Si(111) native oxide for 10 min with a Ga flux of 59 nm/h at a substrate temperature of (a) 600±5 °C and (b) 610±5 °C. Increased substrate temperature results in better size homogeneity visually observed in the panels (see the insets) and statistically reflected in the error bars of the diameter. In panel (a) and (b) the average diameters are 35 ± 10 nm and 39 ± 3 nm, respectively, where the error bars are the statistical standard deviation.

The best Ga pre-deposition result was achieved using a pre-annealing step for a duration of about 35 min followed by Ga pre-deposition at a substrate temperature of 610±5 °C at a Ga flux of 59 nm/h for 10 min. The sample was then annealed for about 20 min at a temperature of 600±5 °C. The diameter of the deposited droplets, as shown in Figure 4.4b, is 39±3 nm, and the number density is $0.1 - 0.5$ μm^{-2}.

[1] In order to exclude the uncertainty related to growth on different wafers, the presented results in panels a and b of Figure 4.4 are from two different positions on one growth sample. The pyrometer temperature reading revealed that those respective positions on the pMBE manipulator have about 10° difference in temperature.

Nanowire growth after Ga pre-deposition

After a homogeneous Ga pre-deposition, the samples were grown at different growth conditions. Figure 4.5 illustrates the overall MBE conditions at a protocol of growth, including Ga pre-deposition. Here, the evolution of substrate temperature, Ga and As cell temperatures, and background pressure are shown. After loading the sample into the chamber, the substrate was ramped up to the pre-annealing temperature (660±5 °C, 35 min). Then, the substrate temperature was decreased to a temperature within 600±5−620±5 °C for Ga pre-deposition (see above) and afterward, changed to a temperature within 570±5−620±5 °C for NW growth. The Ga cell temperature (flux) was decreased after Ga pre-deposition for the NW growth. The vertical dashed lines in Figure 4.5 indicate the periods of Ga supply (pre-deposition) and simultaneous As and Ga supplies (NW growth). Due to the implemented setup of the As effusion cell (no valve), the background pressure increases at high As cell temperatures even at a closed shutter. This background As pressure was shown to result in recrystallization of Ga droplets during the Ga pre-deposition. Therefore, the As cell temperature was kept at low temperatures during Ga pre-deposition and ramped up afterward. After reaching the desirable fluxes, the shutters were opened to initiate the NW growth (see the vertical dashed line indicated by As&Ga supply in Figure 4.5). The fluctuations of the background pressure during the growth run are explained in the caption of Figure 4.5.

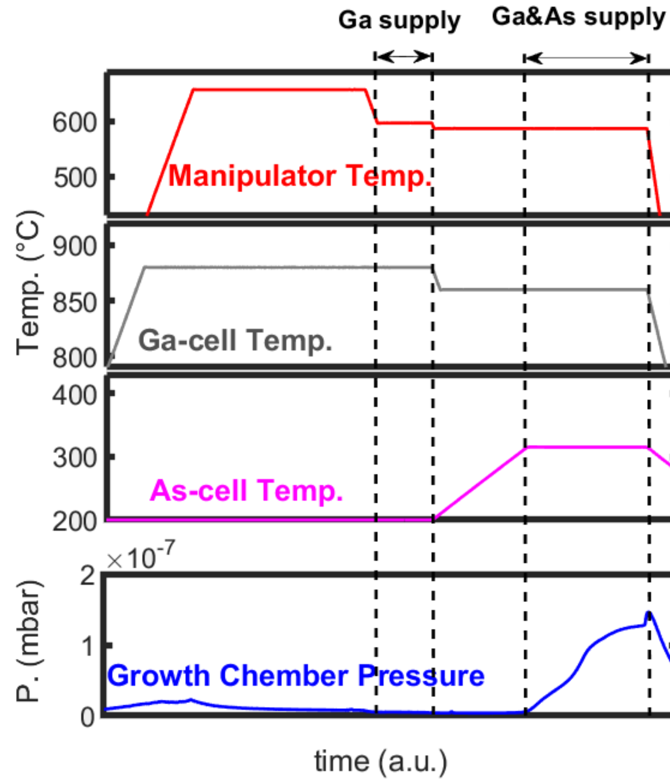

Figure 4.5: The conditions of the pMBE all along our typical protocol of GaAs self-catalyzed NW growth: panel (a) shows the growth chamber pressure; panel (b) shows the substrate temperature; panels (c) and (d) show the temperature of Ga and As effusion cells, respectively. The sample is first pre-annealed at 660±5 °C. Then the substrate temperature decreases to a temperature within 600±5−620±5 °C for Ga pre-deposition. As indicated by the vertical dashed lines, the Ga shutter is kept open only for 10 min. Afterwards, the substrate temperature is decreased down to a temperature within 570±5−620±5 °C for NW growth °C for NW growth. At the same time, the As effusion cell temperature is ramped up to achieve the corresponding desired flux. Then, the Ga&As shutters are opened for NW growth. The initial background pressure is in 10^{-10} mbar range. The pressure increases up to 2×10^{-8} mbar range during the pre-annealing step due to evaporation of material from the hot surfaces and stabilizes down to 5×10^{-9} mbar range along 35 min of annealing. During the Ga pre-deposition, the pressure stays in 10^{-9} mbar range. By simultaneous supply of As and Ga for NW growth, the pressure increases up to 10^{-7} mbar range. Notably, the pressure of the growth chamber is directly related to the temperature of the As cell (even at a closed As shutter). That is because of the high volatility of As.

In Figure 4.6, the aftergrowth SEM micrographs are taken from the samples grown with and without Ga pre-deposition at otherwise identical conditions (compare panel a with b, and c with d). Figure 4.6a and b illustrate two samples grown at a substrate temperature of 570±5 °C. Here, the density of the uprightly standing NWs is 0.6±0.2 μm^{-2} without Ga pre-deposition, and that increases up to 1.8±0.5 μm^{-2} with Ga pre-deposition. Even if one assumes that the pre-deposited Ga droplets (with a density of 0.1−0.5 μm^{-2}) have fully transformed into NWs, the density of the nucleated NWs

between the pre-deposited Ga droplets (1.5±0.6 μm^{-2}) is by a factor 2 larger compared to that without pre-deposition. The enhanced NW nucleation between the Ga droplets can be related to the conditioning of the Si oxide substrate by its interaction with Ga-adsorbed voids (2D Ga). During Ga pre-deposition, the 2D Ga layers nucleate on the defects at the Si oxide surface, leading to the formation of nano-cavities [103]. These nano-cavities are preferential nucleation points for further Ga formation and NW growth during the simultaneous supply of source materials. The 2D Ga layers can be detected by STM as reported by Nitta et al. [103] but are invisible in SEM inspection. With Ga pre-deposition, the density of tilted NWs, as well as PIs, is significantly decreased. As a result, the overall number density of the crystallized nano-objects decreased (a full sample density analysis will be presented in Table 4.2). At the same time, NWs grow 50% longer (see Table 4.1). That indicates a higher local As influx for the existing NWs (see effects of As flux on the NW growth in Figure 4.2). In other words, the As quota for the NWs increases by decreasing the number density of the PIs. As observed in the inset of Figure 4.6b, at the right below, thick NWs (37±4 nm) and thin NWs (22±4 nm) are simultaneously present. The average diameter of the thick NWs is comparable with the diameter of the pre-deposited Ga droplets (39±3 nm), and the average diameter of the thin NWs is comparable with the average diameter of the NWs grown on the sample without Ga pre-deposition. Therefore, NWs have nucleated between the pre-deposited Ga droplets along with the NW growth i.e., interstitial NWs. Consequently, as seen in Table 4.1, at a growth temperature of 570±5 °C, the distributions (standard deviation) of the NW diameters and lengths do not significantly change with or without Ga pre-deposition (∼20 % diameter and $>$ 30% length). The large standard deviations (distributions) are due to the continuous interstitial NW nucleation during the growth.

Growth Temp	550±5 °C no Ga dep.	570±5 °C no Ga dep.	570±5 °C with Ga dep.	590±5 °C no Ga dep.	600±5 °C with Ga dep.	
					Growth time =	
					35 min	4h, 15 min
avg. NW diameter (nm) standard deviation %	45±9 ∼20%	22±5 ∼23%	23±4 ∼17%	42±5 ∼12%	52±3 ∼6%	158±5 ∼3%
avg. NW length (μm) standard deviation %	1.2±0.5 ∼40%	1±0.4 ∼40%	1.5±0.5 ∼33%	1.2±0.1 ∼8%	0.4±0.03 ∼6%	4±0.12 ∼3%

Table 4.1: The diameter and length of the grown NWs at different growth temperatures. The growth duration is 1 hour, otherwise, pointed out. The statistical distribution of the NW diameter and length at higher growth temperatures get narrower. Note that at a growth temperature of 600±5 °C, without Ga pre-deposition, nano-object nucleation is suppressed (see Figure 4.6c). The data is acquired by averaging within a few mm around the growth location on the sample.

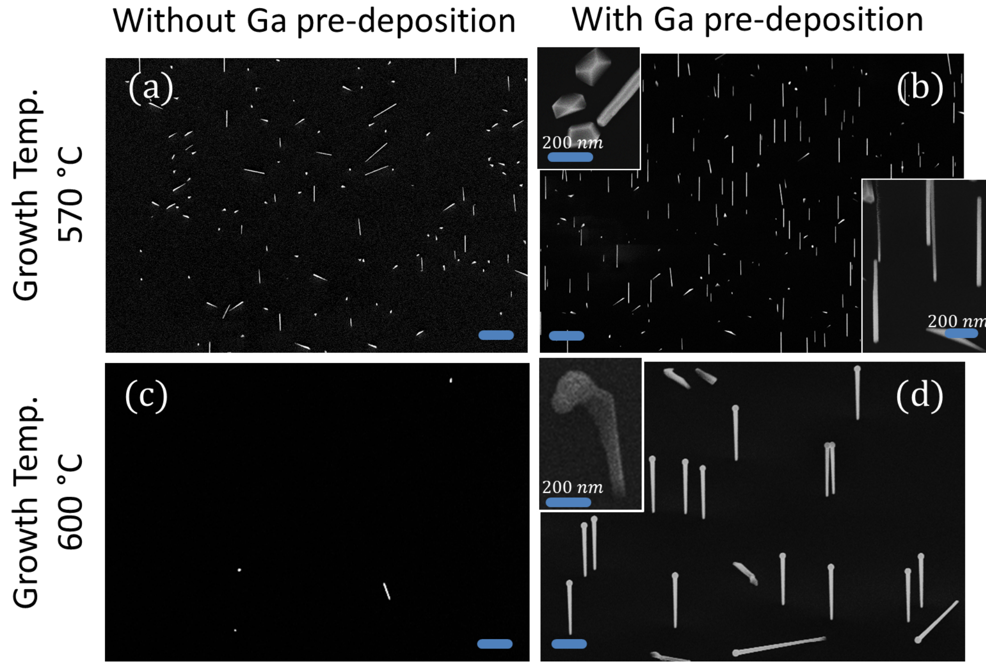

Figure 4.6: SEM micrographs at 30° tilted substrate from four samples after GaAs NW growth at an As flux of 124 nm/h with and without Ga pre-deposition. The samples in panels a and b are grown at a substrate temperature of 570±5 °C without and with Ga pre-deposition, respectively. The growth duration is 1 hour and Ga flux is 24 nm/h for both samples. The inset of panel b at top left, is a SEM top-view image of PIs showing crystallographic facets; and the inset at below right, is a high magnification at 30 ° tilted NWs showing NWs with different diameters. Panels c and d are 2 samples grown at a substrate temperature of 600±5 °C without and with Ga pre-deposition, respectively. The growth duration of the sample in panel c is 1 hour and in panel d is 4 hours and 15 min, both at a Ga flux of 39 nm/h. The inset of panel d is a top-view image of a PI. The scale bars in the panels are 1 μm otherwise indicated.

The substrate temperature was increased aiming to suppress the interstitial nucleation of NWs, i.e., to hinder the crystallization of material anywhere except at the pre-deposited Ga droplets (see Figures 4.3 for effects of substrate temperature on growth). SEM characterization after the growth indicates negligible NW growth at the sample in Figure 4.6c grown at a substrate temperature of 600±5 °C[2]. Similar growth conditions after Ga pre-deposition show NW growth with a number density similar to that of pre-deposited Ga droplets (see Figure 4.6d). That indicates that the main limiting factor for NW nucleation at 600±5 °C is the Ga supply. The SEM cross-sectional side view of this sample is shown in Figure 4.7a−b. The sample is grown for 4 h and 15 min. Figure 4.7c shows the SEM image from another sample grown under identical

[2] The growth position has been about 1 cm away from the center of the sample. The pyrometer temperature reading revealed that the corresponding position on the pMBE manipulator had a temperature of about 600±5 °C.

conditions but for a duration of 34 min. More than 80% of the grown objects on both samples in Figure 4.7 are epitaxially oriented NWs (density analysis will be fully presented in Table 4.2). The NWs/PIs number ratio is significantly increased compared to growth at lower substrate temperatures. Moreover, the standard deviation of the diameter and length decreased to about 3−6% (see Table 4.1). That means that the nucleation of the nano-objects is suppressed during the NW growth. In other words, the supplied material contributes mainly to the growth of the NWs from the pre-deposited Ga droplets.

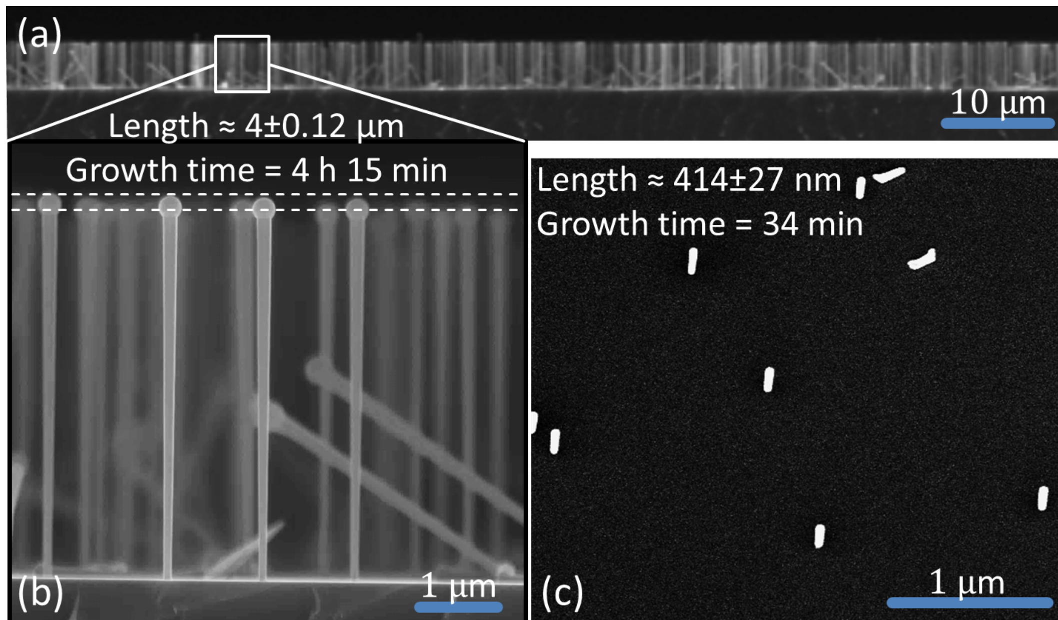

Figure 4.7: SEM micrographs of the NW growth at the growth temperature of 600±5 °C with Ga pre-deposition. Panels a and b are side view images at 89° tilted substrate showing the length homogeneity of the grown NWs. The sample is presented above in Figure 4.6d where the growth time is 4 hours and 15 min, and the average length of the NWs is 4 ± 0.12 μm. Panel c shows a sample grown at identical growth conditions but for a growth duration time of 34 min.

4.1.4 Further analysis

Epitaxial alignment of the overgrown GaAs

The epitaxial III-V NWs on Si grow mostly in the direction of [111] [16]. Additionally, the GaAs NWs can grow on Si along the family of <111> [132] and <112> directions [38]. Figure 4.8 illustrates the epitaxial alignment of the overgrown GaAs nano-objects on Si(111). Here, panels a−b show a top-view SEM image (zero degree tilted substrate) of the sample presented in Figure 4.6b. The fast Fourier transform (with 90° rotation)

at the inset of Figure 4.8a indicates the elongation direction of the majority of the overgrown objects. The red ellipsoid in Figure 4.8a indicates an object which does not fit the majority growth directions. Figure 4.8b is a high magnification of panel a. The NW facets are extracted from the top-view of the NWs and redrawn by a red hexagon. The NW side-facets in self-catalyzed GaAs NWs are reported to be 6 planes from the {110} family [26, 58]: $(\bar{1}10)$, $(1\bar{1}0)$, $(\bar{1}01)$, $(10\bar{1})$, $(0\bar{1}1)$, and $(01\bar{1})$, which are perpendicular planes to (111) plane. In Figure 4.8c, the corresponding NW side-facet surface normals are indicated (from the family of <110> directions). Figure 4.8d shows two examples from the in-plane directions of the NW side-facets (horizontal) and edges (vertical). As indicated, the in-plane directions along the NW edges are the following directions from the family of <121>: $[\bar{2}11]$, $[1\bar{2}1]$, $[11\bar{2}]$, $[2\bar{1}\bar{1}]$, $[\bar{1}2\bar{1}]$, and $[\bar{1}\bar{1}2]$ (see Figure 4.8e). Aside from the in-plane directions of growth, there are three members of the family of <111> ($[\bar{1}11]$, $[1\bar{1}1]$, and $[11\bar{1}]$), which project towards the same direction along [111]. That means that the corresponding objects grow outward the Si(111) with an angle of 19° with respect to the surface. From a top-view, those directions project onto the mentioned family of <121> directions. At the cross-sectional view, they can have an angle of $19-90°$ depending on the in-plane rotational status of the sample in SEM. The cross-sectional SEM imaging revealed that we have NWs grown in both <111> and <121> directions (see Figure 4.8f). In Figure 4.8, the NW indicated by a red ellipsoid in panel a, as well as the nano-objects at the inset of panel b, does not follow any of the above-mentioned crystallographic directions and therefore, they are considered as non-epitaxial, i.e., without an epitaxial relation to the Si(111) underneath substrate. Details on how the tilting of the NWs affects the growth process can be found in ref. [133].

Parasitic island growth

Table 4.2 shows the number density of the grown nano-objects as a function of growth temperature and Ga pre-deposition. The number density of the non-epitaxial nano-objects decreases from 0.5±0.4 μm^{-2} at a growth temperature of 550±5 °C down to zero at a growth temperature of 590±5 °C.

On single-crystalline Si, a passivated layer of native Si oxide forms after exposure to air [94]. Notably, NW growth on an amorphous layer like Si oxide is non-epitaxial. Previous STM studies have revealed that on Si oxide, natural holes exist. These holes are preferential site for heterogeneous nucleation of Ga droplets [103, 129]. The interaction of Ga droplets with the Si oxide results in formation of bigger nanometer-sized

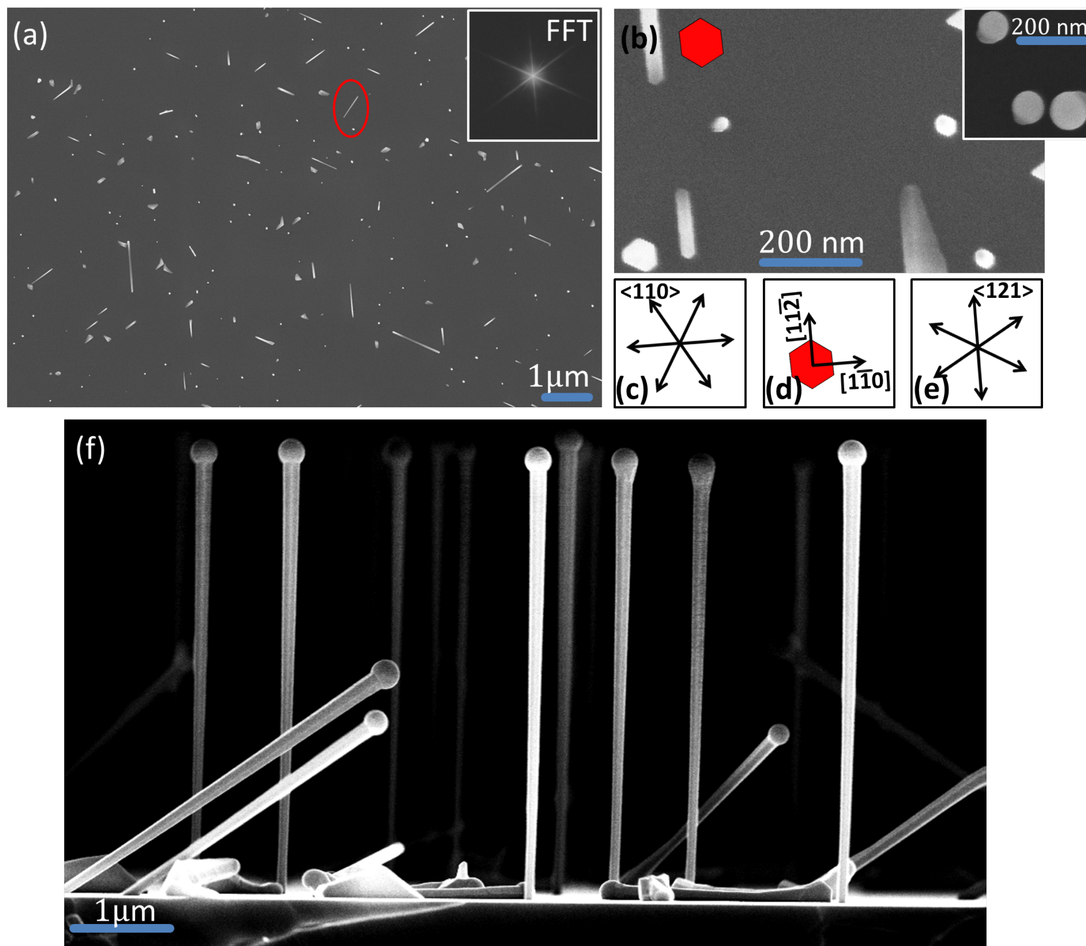

Figure 4.8: Alignment of the GaAs nanostructures along epitaxial crystallographic orientations: (a) top-view SEM image of the sample in Figure 4.6b: the inset of panel a shows the fast Fourier transform (FFT) of the SEM image in panel a with 90° rotation. The FFT highlights the orientations of the majority of the nano-objects. The indicated red ellipsoid shows a nano-object which is nonparallel to the other objects considered as non-epitaxial in the text. (b) High magnification SEM from panel a showing a few NWs and PIs: the red hexagon shows the extracted NW facets. The inset of panel b shows PIs with no epitaxial alignment with the substrate. Panel (c) shows 6 directions from <110> family. Panel (d) shows that [11$\bar{2}$] and [1$\bar{1}$0] directions lay at the in-plane NW facets. Panel (e) shows 6 directions from the <121> family. (f) Side view SEM micrograph of the sample in Figure 4.6d at the sample edge, which has about 10 °C lower temperature during growth. The density of PIs and tilted NWs are higher as compared to the sample center. NWs are grown parallel to the (111) plane and at the alternative <111> directions explained in the text. Note that the rotation of the sample around its surface normal changes the visible angle at the side view within 19−90°.

holes underneath the droplets [103]. Sublimation of Si oxide layer can be enhanced at temperatures lower than its evaporation temperature (900 °C) because of the chemical reactions in equations 4.1−4.3 [24, 134, 135].

$$2\mathrm{Ga}\,(\mathrm{liquid}) + \mathrm{SiO_2}\,(\mathrm{solid}) \rightarrow \mathrm{SiO}\,(\mathrm{gas}) + \mathrm{Ga_2O}\,(\mathrm{solid/gas}) \tag{4.1}$$

Density \ Growth Temp	550±5 °C	570±5 °C	570±5 °C with Ga pre-dep.	590±5 °C	600±5 °C with Ga pre-dep.
Upright NWs (μm^{-2}) (Percentage%)	0.6±0.1 ~7%	0.6±0.2 ~10%	1.8±0.5 ~57%	0.5±0.2 ~31%	0.07±0.04 ~57%
Tilted NWs (μm^{-2}) (Percentage%)	3.6±1 ~43%	2.4±0.5 ~40%	0.5±0.1 ~16%	0.7±0.2 ~44%	0.05±0.03 ~40%
Epitaxial PIs (μm^{-2}) (Percentage%)	3.6±0.7 ~43%	2.8±0.5 ~45%	0.8±0.2 ~26%	0.4±0.1 ~25%	0.003±0.002 ~3%
Non-epitaxial objects (μm^{-2}) (Percentage%)	0.5±0.4 ~6%	~0.3±0.2 ~5%	0.07±0.07 ~1%	0	0
NW/PI yield	1	1	2.6	3	33

Table 4.2: The density and overall percentage of the grown nano-objects as a function of growth temperature and Ga pre-deposition. By increasing the growth temperature, 1) the overall density of the deposited nano-objects decreases (sum of the density values at the columns); 2) the PI percentage decreases; 3) the non-epitaxial growth decreases and fully hinders above 580 ± 10 °C; 4) the number ratio NWs/PIs increases. By adding a Ga pre-deposition step to the protocol of growth, the number ratio NWs/PIs further increases (up to 33), and the PI percentage further decreases. The data is acquired by averaging within a few mm around the growth location on the sample.

$$4\mathrm{Ga}\,(\mathrm{liquid}) + \mathrm{SiO_2}\,(\mathrm{solid}) \rightarrow \mathrm{Si}\,(\mathrm{in\,Ga}) + 2\mathrm{Ga_2O}\,(\mathrm{solid/gas}) \tag{4.2}$$

$$\mathrm{SiO_2}\,(\mathrm{solid}) + \mathrm{Si}\,(\mathrm{in\,Ga}) \rightarrow 2\mathrm{SiO}\,(\mathrm{gas}) \tag{4.3}$$

Ga droplets oxidize at their interface with Si oxide based on equations 4.1 and 4.2. The resulting gallium oxide is volatile in vacuum increasingly at temperatures above 580 °C as reported by Cho in ref. [136]. This process can explain the zero number density of non-epitaxial growth at growth temperatures above 580 °C in our results. On the other hand, the resulting Si oxide evaporates; and the atomic Si is soluble into the Ga droplet above 500 °C based on the Ga-Si phase diagram [137]. The atomic Si can also further react with the Si oxide layer to form volatile species based on equation 4.3 [136]; and it eventually can etch the Si substrate likely limited to the solubility of Si in Ga [135, 138].

4.1.5 Conclusion

Commonly, GaAs self-catalyzed GaAs NWs are grown on Si by a simultaneous supply of Ga and As source material. In this growth scheme, the NW size and number density could not be independently modified. Moreover, PI growth can not be suppressed (NW/PI < 5). A Ga pre-deposition step before NW growth provides a new degree

of freedom in order to control the NW average diameter. Moreover, after a Ga pre-deposition step and by an interplay of high growth temperature and low Ga flux, the interstitial growth of nano-objects between the Ga droplets is suppressed. In this way, we could narrow the length distribution of the NWs. A high temperature of growth (above 580±10 °C) also fully suppresses the non-epitaxial growth of NWs as a result of an enhanced Ga etching effect. Ga etches the Si oxide increasingly above 580 °C [136], which increases the probability of epitaxial correlation between the GaAs overgrown material with the Si(111) substrate. Moreover, by our proposed strategy, the NW/PI ratio increases (> 30). It is worth noting that the absolute values of the optimum growth parameters are closely related to the Si oxide morphology and thickness. The reproducibility runs on different wafers showed that the oxide morphological uncertainties seem to be an uncontrolled aspect of the GaAs NW growth on native Si oxide substrates. Therefore, our growth parameters shall be considered rather qualitative; and a small window for "trial and error" is required for each batch of wafers.

4.2 Patterning Si Substrates by Focused Ion Beam

In Section 4.1, a successful attempt was made to grow GaAs NWs on Si native oxide substrates. There, Ga droplets form at random positions of the Si oxide nanocavities [28]. Out of the droplets, NWs grow while the neighbored nanoparticles compete for the source material. Because the spacing between the NWs is random, there are local differences in source supply at different NWs. Consequently, the diameter, crystal phase structure, and growth orientation may differ comparing NWs grown on the same substrate. For better control of these NW properties, substrate patterning can be deployed to achieve a regular arrangement and therefore uniform NW properties. Moreover, substrate patterning facilitates the fundamental growth studies by excluding the surrounding effects. The latter is addressed in chapters 5 and 6.

Lithography based patterning is the most widely used approach for defining NW growth: e.g., electron beam lithography [91], nano-imprint lithography [139], nano-sphere lithography [140, 141], and laser-interference lithography [142]. These techniques require multiple processing steps, and consequently, they are time-consuming. Moreover, lithography techniques widely use oxygen- and carbon-based contaminants, which can degrade the performance of NWs in devices [143]. As an alternative, we report on lithography-free pattering of Si oxide for NW growth using a focused ion beam. In our proposed approach, we reduced the patterning process to a single step of ion

beam exposure. Using the current FIB technology, each nucleation point at the sample is drilled once after another. By a few mins of FIB patterning, a few square mm of sample area could be prepared for further NW growth. Despite some recent reports on FIB patterned self-catalyzed GaAs NWs [144, 145, 146], detailed understanding of the mechanism behind this technique for reproducible high yield of NW growth is missing.

The data in this chapter is published in ref. [79, 97]. In this work, we report on the interaction of the ion beam with Si substrates and address the critical aspects of this interaction to optimize NW growth. For evaluating the NW growth, we used SEM and μXRD. The SRIM software assists our experimental findings (*Stopping and Range of Ions in Matter*) [147]. Because of its destructive nature, a FIB can efficiently remove the material at any position of exposure. High ion doses can eliminate the Si oxide and displace (amorphize) the Si atoms below the oxide. Our experimental data indicate recrystallization of Si lattice along with the NW growth protocol. As a result, epitaxial NW growth takes place, which can be explained by recrystallization of the Si lattice. On the other hand, the diameter of the FIB patterned holes plays the central role to achieve a high yield of vertical NWs. Holes with a small diameter can not provide sufficient area for NW growth whereas holes with large diameter initiate parasitic islands (PI)s growth and the growth of multiple NWs. At the FIB holes of intermediate size, we achieved a NW growth yield higher than 80%.

4.2.1 Experiment

Figure 4.9 shows a schematic illustration of the FIB process used in this study. N-type 2 inch Si wafers with thermal Si oxide of $\sim 16 \pm 2$ nm thickness were used as the template. The FIB was used to drill defined positions at the substrate. In the next step, Ga droplets were pre-deposited at the FIB holes using the pMBE. As a result, the NW growth was initiated at positions of the deposited Ga droplets.

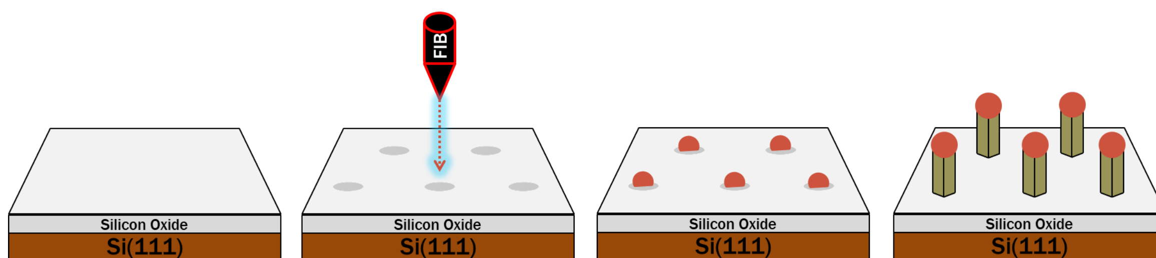

Figure 4.9: Schematic illustration of the NW growth employing FIB patterning. The substrate is Si(111) covered by a 16±2 nm layer of Si oxide. The FIB patterning process is limited to only one step where the holes are drilled at pre-defined positions by a Ga^{+} ion beam focused at a cross-section of 6 nm (30 keV, 93 pA). At the pMBE chamber, Ga is first pre-deposited and formed at the holes. NW growth is followed by supplying both As and Ga fluxes.

Patterning by a focused ion beam

Danial Bahrami performed the procedure of FIB patterning as follows. First, the thickness of the oxide layer was determined to be 16 nm by X-ray reflectivity and ellipsometry measurements [148]. The uncertainty of the oxide thickness across the Si wafer appeared to be ±2 nm. The FIB process was performed using a Helius Nanolab Dualbeam 600 FIB-SEM FEI machine at Siegen University. The employed ion beam was focused onto a cross-section of about 6 nm at the focal point using a beam energy and current of 30 keV and 93 pA, respectively. Using these conditions, the Si(111) wafers were patterned by the FIB where several subregions of 10×10 holes were placed on a square grid with 5 μm distance between the holes. The patterned region of the sample includes 9×9 arrays of the square grids patterned using different ion doses, as illustrated in Figure 4.10. Here, each hole is drilled by a single dot exposure of FIB. The dot dwell time for patterning was $10^{-3}-0.45$ ms per hole resulting in implantation of 0.1−45 fC equivalent to about 600−280,000 $^{Ga^{+}}/_{\text{point}}$.

Nanowire growth

After the FIB procedure, the samples were etched for 1 min in 0.5 % hydrogen fluoride (HF) acid diluted in water. The samples were HF treated because the NW growth was performed few days after the FIB patterning process. Then, the samples were boiled in deionized water for 10 min to flatten the oxide and reduce the probability of parasitic growth between the FIB patterned holes [93]. The samples were then directly loaded into a pre-chamber and degassed at 300 °C for 30 min (background pressure

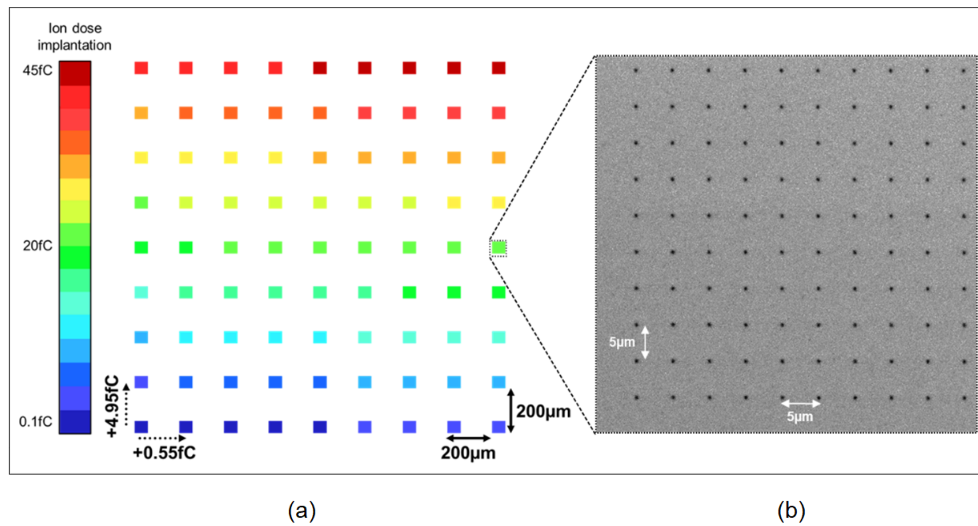

Figure 4.10: (a) Reference design created by FIB schematic illustration of the FIB process: matrix of implemented ion doses 0.1−45 fC at 9×9 regions. (b) Each array included 10×10 holes with 5 μm spacing.

$< 5 \times 10^{-7}$ mbar). The samples were transferred into the MBE chamber and then heated up to 700±5 °C for 10 min and ramped down to the growth temperature of 560±5−630±5 °C. At the growth temperature, an amount of Ga equivalent to about 45 2D GaAs mono-layers were deposited. As a consequent, Ga droplets nucleate at the FIB patterned holes. Out of these droplets, NW growth was performed by VLS mechanism of growth at a Ga flux of ∼50−150 nm/h and a V/III ratio of ∼1−2 for 1 hour. The resulting diameter and length of the NWs were 15−150 nm and 1−4 μm, respectively (see Figure 4.2 for effects of growth conditions on NW size). It will be shown in the following that the FIB hole diameters determine the quality of NW growth. Therefore, the author studied the influences of HF and high-temperature treatments in altering the hole diameter. Such procedures usually are parts of protocols of patterning\growth, and we will highlight that their fundamental effects should be considered in order to achieve a high yield of NW growth.

SEM characterization

In order to access the in-depth characteristics of the FIB holes, a cross-sectional SEM imaging procedure was performed by Danial Bahrami (see Figure 4.11). In order to systematically access to the diameter of the holes, the author inspected the top-view SEM micrographs. The image analysis was performed by taking an intensity distribu-

tion along a line through the center of a hole. The fwhm of the line profile peak was estimated as a measure of the hole diameter. Note that due to non-sharp side-walls of the holes (see Figure 4.11c), the extracted hole diameter is highly sensitive to SEM settings (e.g., contrast and brightness). That can result in deviations of the diameter reading at the SEM top-views. By keeping the SEM settings constant, different patterned subregions were investigated. Since extracting absolute values of the hole diameter is rather challenging, the reader shall concentrate on the qualitative effects of the studied parameters: ion dose, wet etching duration, high-temperature annealing.

4.2.2 Results and discussion

Ion-solid interaction

Using the SRIM software [147], we simulated the interaction of Ga ions with a Si substrate covered by 16 nm of SiO_2. Our simulations revealed that the mean stopping distance of 600 - 280000 impacting Ga^+ ions at the substrate varies from 21 nm to 27 nm in-depth and from 6 nm to 30 nm laterally. The results addressing the interaction of ions with Si agree with those shown in ref. [144].

Figure 4.11 shows the cross-sectional imaging procedure (see the caption of the figure for details). In Figure4.11c, a high magnification cross-section of a FIB hole is shown. The dark region is the Si substrate covered by oxide, and the gray zone is the supportive platinum layer. The depth of the FIB drilled hole in Figure 4.11c is about 28 nm. Given that the Si oxide layer is about 16±2 nm, Si bulk material is removed by about 10±2 nm. That indicates damage of Si substrate at the bottom of the holes, which is in agreement with our simulations. Moreover, molecular dynamics simulations have shown that at an acceleration voltage of 30 keV, about 1000 ions are sufficient to displace the Si atoms from their lattice points by about 2 nm at a depth of several nm [143]. Therefore, we conclude that the FIB patterning at high ion doses will amorphize the Si wafer below the holes. Note that the cross-sectional SEM image in Figure 4.11c also shows that the edges of holes are non-sharp, as mentioned above. As a consequence, the diameter of the hole can not be precisely determined.

Ga droplet formation

Implantation of 600−280,000 $^{Ga^+}/_{\mathrm{point}}$ at 30 keV (regardless of back-sputtered ions) corresponds to a local Ga concentration of $1.1 \times 10^{19} - 5 \times 10^{21}$ $^{Ga^+}/_{cm^3}$ [144] in the Si region

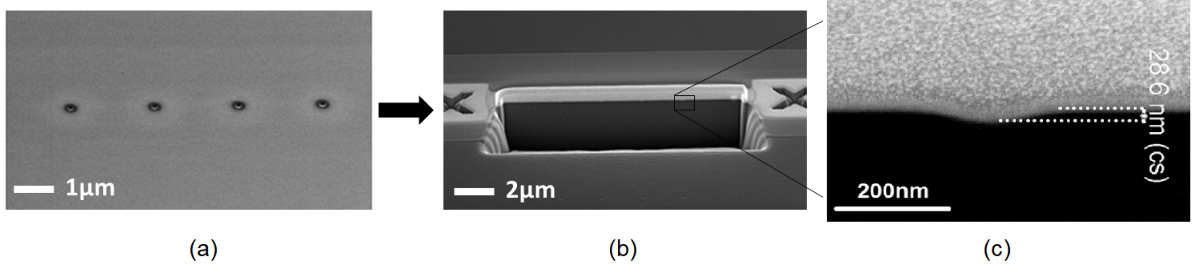

Figure 4.11: Cross-sectional SEM imaging procedure of the FIB patterned holes (performed by Danial Bahrami). The employed ion dose is about 280,000 $^{Ga^+}/_{point}$ at the shown holes. (a) Patterned holes at 30° tilted substrate after FIB drilling. (b−c) The sample is cut by FIB milling after a typical TEM lamela preparation procedure. For preparation, a supportive platinum layer is deposited on the substrate and FIB milling is performed through roughly the center of the holes. Panel c shows the topographical morphology of a single hole at about 89° tilted substrate. The dark region is the Si substrate. It is observed that the depth of the hole is about 29 nm with respect to the Si surface. Notably, the edges of the holes are not sharp and therefore, the diameter of the hole cannot be precisely determined.

underneath the patterned holes. The solubility limit of Ga in Si is $4.5 \cdot 10^{19}\ cm^{-3}$ based on ref. [149]. Because the solubility limit is surpassed at the high ion doses, by annealing of the specimen, the implanted Ga atoms can diffuse from the bulk Si toward the surface. We disregard the temperature-dependent solubility and assume that all the implanted Ga atoms diffuse toward the Si surface and contribute to Ga droplet formation. With this assumption, the volume of liquid Ga at the holes after annealing is:

$$V_d = \frac{nM}{\rho N_a} \tag{4.4}$$

where n is the ion dose, M is the atomic mass of gallium ($^{g}/_{mol}$), ρ is the volume mass of the gallium in a liquid droplet ($^{g}/_{cm^3}$), and N_a is the Avogadro's number. Assuming that a single Ga droplet with a geometry of half a sphere forms at each hole, the resulting diameter of the droplets at the implemented ion doses would be about 3−28 nm. This motivated me to perform an annealing step at 600 °C for 15−60 min after Ga implantation. Within the resolution of SEM, we could not detect any Ga droplet at the holes. Detz et al. drilled holes into Si wafers using ion doses of $6.2\times10^4 - 3.1\cdot10^5$ $^{Ga^+}/_{point}$ at 5−30 KeV [144]. The authors observed Ga aggregation and/or droplet formation by annealing at 600±5 °C for 10 min. One could explain this discrepancy with our results by evaporation of Ga at the UHV chamber. The Ga vapor pressure at 600±5 °C is $5.5 \cdot 10^{-8}$ mbar [150] whereas the pressure of the UHV chamber during annealing was in the range of 10^{-9} mbar. That means that the Ga atoms can continuously evaporate and leave the Si surface after diffusing toward the surface.

It was discussed in Section 4.1 that Ga positioning is advantageous for achieving uniform NW characteristics. As shown above, the implanted Ga was not sufficient for droplet positioning at the holes. Therefore, we deposited 45 MLs of Ga at a substrate temperature of 630±5 °C (Figure 4.12a−d). Figure 4.12 in panels a−d shows different holes on the same growth sample by increasing ion dose from left to right. At low ion doses, associated with small hole diameters, no Ga droplet is formed (see Figure 4.12a). By increasing the ion dose (hole diameter), Ga droplets form in the holes (see Figure 4.12b). By further rising the ion dose (hole diameter), the volume of the deposited Ga per hole increases (see Figure 4.12c). The simulations indicated that Si oxide is fully removed at the holes. However, after the consequent HF treatment (explained above), the samples are shortly exposed to air. That can result in formation of a native oxide layer at the holes (∼1nm). It has been reported, that the impinging Ga vapor at bare silicon [139], as well as silicon oxide with thinner oxide thicknesses [101], has higher sticking coefficients as compared to thicker oxide layers. Therefore, the collection area of the impinging Ga vapor increases at increased hole diameters. Further increasing of the ion doses up to the upper range of the values resulted in aggregation of Ga (see Figure 4.12d). Ga aggregation cannot be explained merely by a bigger collection area, because such a phenomenon was not observed in my experiments on native oxide with comparable Ga densities ($50-100\ \mu m^{-1}$). Moreover, lithography based approaches also have reported on multiple Ga droplets at large patterned holes (e.g., see ref. [139]), but such a Ga aggregation as in Figure 4.12d is not reported. Therefore, this phenomenon is likely related to the FIB process itself and also observed by the authors in ref. [144]. The interaction of FIB with the surface might results in changes of the sticking and diffusion of Ga adatoms increasingly at higher ion doses. Therefore, we conclude that an increase of the ion dose is not advantageous in FIB patterning for NW growth due to multiple Ga formation and Ga aggregation at the holes.

At some of the samples after Ga pre-deposition, Ga droplets form on Si oxide between the FIB holes (interstitial Ga formation). Other groups e.g., refs. [91, 101] found a similar observation. This could be explained by the roughness of the Si oxide surface providing preferential nucleation sites for Ga droplets. Intact controlling of interstitial Ga formation seems to be still a challenge despite the advancements [93]. However, full technical control on this phenomenon seems to be still a challenge. We will show that the interstitial Ga droplets remain not crystallized after NW growth. To fully remove the Ga droplets from the substrate, based on this thesis, we suggest performing an annealing step at temperatures above 510±25 °C (see Chapter 6). It will be shown in Chapter 6 that, exposure of the samples to air accelerates evaporation of Ga droplets.

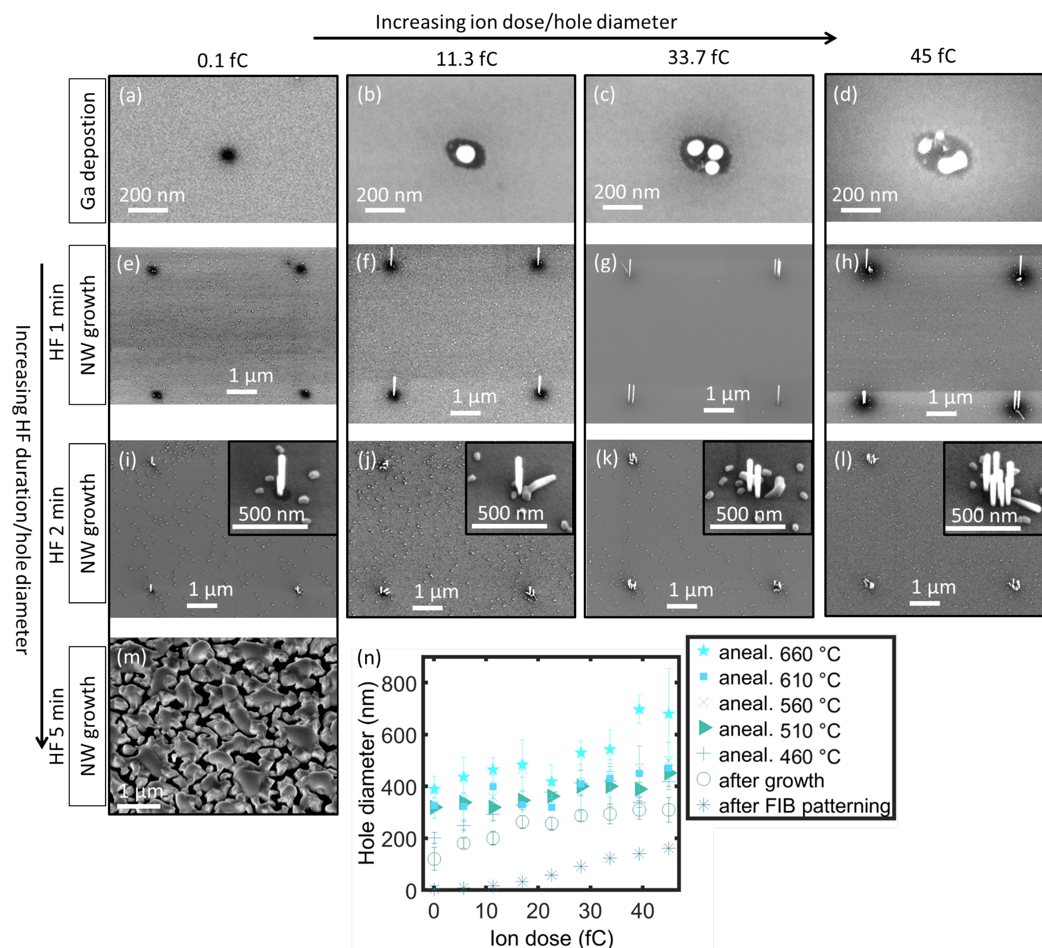

Figure 4.12: SEM micrographs at a 0° tilted substrate in panels a—d and 30° tilted substrate at panels e—m. Each row of SEM images is from a different growth sample. From left to right the columns show increasing ion dose, as indicated. Panels (a—d) show a sample after Ga pre-deposition at a substrate temperature of 630±5 °C ($1 - 5 \times 10^{-8}$ mbar background). The sample was HF treated for 1 min. Ga was deposited at a Ga flux equivalent to 0.32 ML/s for 140 s ($\sim$ 45 Ga MLs deposited). Panels (e—h), (i—l), and (m) show three NW growth samples HF treated for 1, 2, and 5 min, respectively. After Ga pre-deposition, NWs were grown on the samples at a Ga flux of 150 nm/h and a V/III ratio of 2 at a substrate temperature of 610±5 °C. (n) Hole diameter extracted from top-view SEM as a function of ion dose: 1) after FIB patterning; 2) after NW growth procedure; 3) after annealing for 1 hour consequently at 450±5—650±5 °C with 50 °C steps.

Nanowire growth

Panels e−h in Figure 4.12 show a sample of NW growth after Ga pre-deposition at FIB patterned sub-regions corresponding to panels a-d. At low ion doses where no Ga was formed during Ga pre-deposition, also no grown NWs are observed (cf. Figure 4.12a,e). In regions with single Ga droplets, about 80% of the FIB holes have single upright NWs (80% yield) (cf. Figure 4.12b,f). By increasing the ion dose, multiple NWs grow inside each hole, which is expected due to the appearance of multiple Ga droplets after Ga-predeposition (cf. Figure 4.12c,g). The probability of PI formation increases at bigger holes (cf. Figure 4.12d,h). Formation of PIs versus NWs can be explained by the wetting effects of the Ga droplets colliding with holes with different geometries [102]. Additionally, the aggregated Ga likely forms PIs (cf. Figure 4.12d, h). Therefore, in this method the intermediate hole diameters are optimal for NW growth.

Effects of wet etching on the FIB holes

Each row of SEM micrographs in Figure 4.12e−m shows a specific growth sample, which from top to bottom, the samples are HF treated for 1, 2, and 5 min, under otherwise identical preparation/growth conditions. In each row from left to right, the ion dose increases. By extending the HF treatment time at constant ion doses, the diameters of the patterned holes consistently increase. The increasing HF treatment duration has a similar effect on the NW growth quality as for increasing ion dose. In particular, by increasing the HF treatment time from 1 to 2 min, NWs can grow at the patterned region with an ion dose of 0.1 fC (cf. Figure 4.12e,i). At the same time, at the higher ion doses, the probability of nucleation of multiple NWs and PIs increases (compare Figure 4.12f−h with j−l). By 5 min HF treatment, the pattern is entirely removed, and the sample is covered by PIs (see Figure 4.12m). The formation of PIs is related to Ga droplet wetting angle as Matterini et al. have shown in ref. [28]. The authors have shown that NW growth is not favorable if the Si oxide is entirely removed from the Si substrates [102].

Effects of high-temperature annealing on the FIB holes

Figure 4.12n shows the diameter of the FIB patterned holes after i) FIB patterning, ii) NW growth, and iii) annealing of the sample in MBE without any supply of source material (pressure of 10^{-9} mbar). The annealing was repeated step by step starting

from a temperature of 460 °C up to 660 °C in 50 °C steps and for 1 hour at each temperature. After each annealing step, the author characterized the sample by SEM. Then, a typical procedure of degassing was performed at a pre-chamber at 300 °C for 1 hour and transferred to the MBE chamber for the next annealing step. As seen in Figure 4.12n, the hole diameters significantly increase after the NW growth procedure as compared to those after FIB patterning. we reported the detailed effects of the high-temperature treatments at different temperatures on the GaAs nanostructures in Chapter 6. In the present section, the highlight is that the FIB hole diameters increase at temperatures above 510 °C in the presence of GaAs NWs (see Figure Figure 4.12n). It is widely known that the evaporation temperature of the Si oxide is around 900 °C. However, it has been shown by scanning probe microscopy that, the Si oxide surface morphology can be affected at the nanoscale by annealing at temperatures as low as 690 °C [88]. In Chapter 6, we reported that the Ga droplets decrease size or vanish by annealing in MBE without supply of source material at temperatures as low as 510 °C. The Ga atoms can diffuse along the NW facets toward the substrate through a reverse reaction growth. The diffusing Ga on the surface can interact with the Si oxide substrate which has been formerly shown to enhance Si oxide evaporation as reported by Nitta et al. [103]. Therefore, we speculate that along GaAs NW growth, the diffusing Ga on the Si substrate can also have a similar effect in interacting with the Si oxide at the holes leading to continues increase in the hole diameter along NW growth as shown in Figure 4.12n (compare the hole diameters after FIB patterning with that after NW growth).

Interstitial growth

The Ga droplets, which nucleate between the holes, could not initiate GaAs nucleation during the NW growth, in contrast to the Ga droplets inside the holes. Heterogeneous nucleation onto crystal surfaces has lower formation energy compared to nucleation on an amorphous material [129, 151]. That is because of interaction between substrate surface atoms with the atoms of the overgrown material leading to decreasing size of the minimum stable nuclei [129]. Solidification of GaAs crystals at the interstitial Ga droplets could be, in principle, initiated by increasing the As flux or decreasing the temperature [152]. To explain, the increased As flux provides more atoms to the surface that can form a stable nuclei of GaAs crystals within the Ga droplet. In addition, decreased temperature results in decreasing size of the minimum sable nuclei. Therefore, both mentioned parameters can increase the probability of nucleation of GaAs crystals

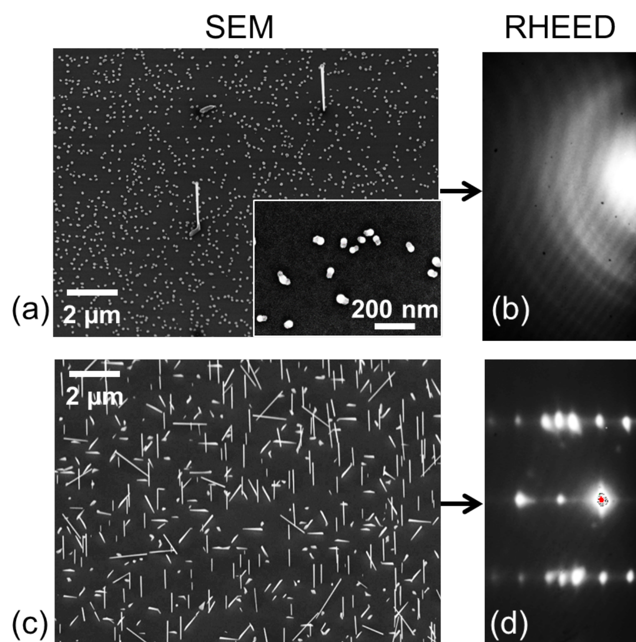

Figure 4.13: (a) SEM image at the FIB patterned region at 30° tilted substrate. The uncontrollable roughness characteristics of the oxide have resulted in the nucleation of non-epitaxial GaAs crystallites between the holes together with epitaxial NWs at the holes. (b) RHEED imaging of the sample shows DS rings originating from the non-epitaxial growth between the FIB holes. (c) SEM at 30° tilted substrate of a sample of Si(111) covered by native Si oxide with a considerable amount of GaAs NW growth, and in panel (d) the corresponding RHEED pattern shows distinct Bragg reflections as a characteristic of epitaxial growth.

on the amorphous oxide. In Figure 4.13a, the sample is supplied with As during the aftergrowth cool-down. As seen in the inset of Figure 4.13a, GaAs crystals have formed. SEM image analysis, similar to that in Section 4.1.4, indicates non-epitaxial growth of these crystals. During the cool down (with a rate of 20 °C/min) at a temperature range of 450−550°C, GaAs DS rings appeared in RHEED (see Figure 4.13b). Note that the yield of NW growth at the holes on this sample is low. That leads to a loss of epitaxial GaAs signal (RHEED spots) in the background of the RHEED signal. For comparison, the aftergrowth SEM and RHEED image of a NW growth on Si native oxide is shown in Figure 4.13c−d (see the density of epitaxial growth in panel c and the distinct RHEED spots in panel d).

Epitaxial nanowire growth on damaged Si

It was shown above that, epitaxial NW growth is fully suppressed between the FIB holes (see Figure 4.13). On the other hand, the nano-objects at the FIB holes epi-

taxially correlate with the substrate as we will show in Chapter 5 and 6. In order to evaluate the epitaxial correlation of overgrown nano-objects under extreme conditions of FIB, we patterned a cross-shaped area on the sample, as shown in Figure 4.14a. In particular, this region is patterned by illuminating a grid of spots with 5 nm spacing using a high FIB dose of 45fC (30 keV, 93 pA, 6 nm beam width). Note that on this cross-shaped area, the neighbored illuminated points overlap leading to complete removal of the oxide. In addition, cross-sectional SEM imaging showed that more than 10 nm of the underneath Si substrate is removed. Here, the SRIM simulations indicated that the crystallinity of the Si substrate is affected down to a depth of the 50 nm (for 10000 $^{Ga^+}/_{\mathrm{point}}$). However, SEM image analysis, as well as μXRD evaluation of the crystal orientation of the overgrown objects, shows epitaxial relation between the overgrown nano-objects and the underneath Si substrate. In particular, the orientation of a significant portion of the grown NWs on this area is perpendicular to the substrate, which is a characteristic of epitaxial correlation between GaAs NWs on Si(111). Parasitic growth objects also showed distinct and aligned facets. The μXRD experiment was performed at this region using the micrometer-sized X-ray beam. The μXRD experiment details were discussed in Chapter 3. The diffraction pattern indicates that the growth is epitaxial. In particular, a range of misorientations within few degrees is naturally expected between the crystal orientation of the overgrown objects and the underneath substrates. Such a natural misorientation in epitaxial growth is discussed in Chapter 5 and 6 and formerly reported on native oxide by the authors in ref. [153]. In XRD Bragg reflections, such misorientations are visible by elongation of Bragg spots along their Debye-Scherrer rings. This behavior is in contrast to non-epitaxial growths, where the diffuse scattering of Bragg peaks contributes to a homogeneous intensity distribution along Debye-Scherrer rings. Therefore, it is evident that damage of Si is not an issue in FIB patterning. That can be explained by recrystallization of amorphous Si. Proust et al. have reported that amorphous Si layers recrystallize along their (111) planes by annealing at temperatures between 578 – 658 °C [154].

4.2.3 Conclusion

In this work, a lithography-free patterning method is used to define regular arrays of nanometer-sized holes on silicon substrates. In particular, defined positions at a thermal oxide layer on Si(111) are drilled using a focused Ga+ ion beam. At the drilled holes, first, Ga droplets were positioned, and then self-catalyzed GaAs NWs were grown. Our

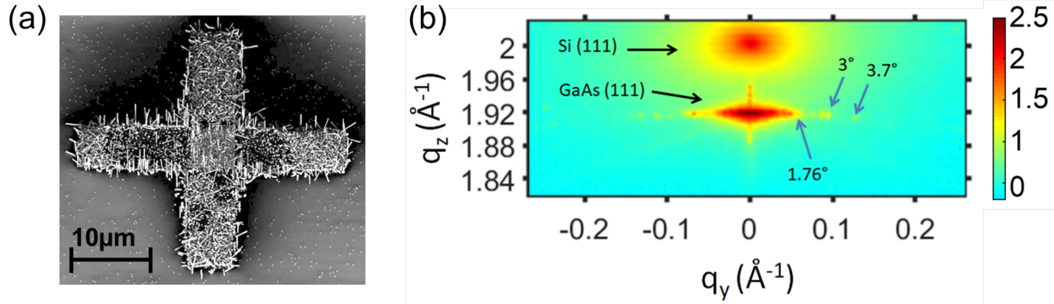

Figure 4.14: (a) SEM micrographs at 30° substrate showing parasitic islands together with upright NWs oriented perpendicular to the surface, which is the characteristic of epitaxial GaAs NWs. (b) XRD image of the cross-shaped region shown in panel a at the vicinity of the cubic (111) Bragg reflections of the Si and GaAs. The XRD experiment is performed using a micrometer-sized beam illuminating a footprint of 1.8×50 μm^2 on the sample at GaAs(111) Bragg conditions. Here, a geometry similar to that in Figure 3.3 is used. The indicated blue arrows show the corresponding tilting angle of the GaAs(111) planes as compared to Si(111) orientation of the substrate. The XRD image shows a characteristic epitaxial relation of the overgrown GaAs material on the Si the substrate.

experimental and theoretical understanding behind this patterning process revealed that the exposure process induces damage to the crystalline structure of the underlying Si substrate. However, μXRD shows epitaxial growth of GaAs NWs at the holes indicating recrystallization of the damaged Si. In agreement with our results, a previous report has documented that damaged Si can recrystallize at temperatures above 580 °C [154]. Our study shows that the diameter of the drilled holes plays a crucial role in optimizing the vertical yield of NW growth. The hole diameter could be manipulated by deviating the focused ion beam dose (600−280,000 Ga^+ per hole) at otherwise constant ion characteristics. The top-view SEM images showed that the diameter of the FIB patterned holes vary within a rough approximate range of 6−200 nm after the FIB patterning procedure. Moreover, hydrogen fluoride etching (1−5 min) and the high-temperature steps involved in the protocol of growth (450−650 °C) can significantly change the hole diameter. In the present study, at the patterned holes with a mean diameter within ~200−240 nm, we obtained more than 80% of vertical NW yield. Increasing the hole diameter resulted in the growth of parasitic islands and multiple NWs at the holes. We explain this diameter dependency by increased collection area of source material at the substrate as well as unfavorable wetting of the Ga droplets at the bigger holes. However, the optimum hole diameter may vary for different growth parameters and silicon oxide intrinsic characteristics. FIB patterning can attract significant attention in the future because a lithography-free single-step of hole drilling completes the patterning procedure. Moreover, our report can be qualitatively considered for other material sys-

tems of NW growth to substitute other patterning techniques. To translate our results, one has to consider a window of trial and optimization by implementing a range of ion doses at each growth protocol on each batch of samples. In this way, a small window of trial and error can efficiently optimize the hole diameters for a high yield of growth.

Chapter 5

In-situ monitoring of nanowire growth

In Chapter 1, it was pointed out that the performance of NW devices is optimal when the nano-objects have uniform size [91, 37], composition [155], and orientation [153]. To this end, it is highly desired to develop the fundamental understanding of the NW growth mechanisms by in-situ monitoring of their synthesis [42]. In the present chapter, the first μXRD of an individual growing NW is reported. First, patterned Si substrates are used (see Section 4.2) in order to identify the position of NW growth on the sample. Second, the micrometer-sized synchrotron X-ray beam, presented in Section 3.1, is used to resolve XRD signal from individual NWs. Finally, the position of the beam on the sample is stabilized in order to monitor the growth of an individual NW. During the NW growth, the evolutions of the crystal structure, size, and orientation of the NW are extracted. The chapter is organized as follows. In Section 5.1, the experimental approach is presented. In Section 5.2, the results and analysis approaches are shown. The acquired results are discussed in Section 5.3. The chapter is concluded in Section 5.4. The outcome of this chapter is in review for publication in paper IV.

5.1 Experimental details

Attempts to study individual NWs during growth are hampered by the fact that it is not apriori known where NWs nucleate. Therefore, the author decided to use a sample with existing NWs. In this way, one could find the position of the NWs. The NWs were then removed by annealing, and another growth step was performed while hoping that new NWs appear at the same location. In order to increase the probability of success, a FIB patterned sample of NW growth was used as the template. However, as shown in Section 4.2, an annealing step could change the yield of NW growth at the patterned

holes, which was the uncertainty of the approach.

Using the μXRD setup (see Figure 3.1), the following sequential steps were performed in order to prepare for the in-situ time-resolved study of an individual NW growth:

(Step 1) A preferential position is located on the GaAs NW sample grown onto a pre-patterned Si(111) substrate by means of X-ray beam detection. The sample contained several subregions of squared grids of FIB patterned holes, as shown in Chapter 4, Figure 4.10. This initially grown sample was ex-situ characterized by SEM. Then the sample was re-inserted into the pMBE, and using the μXRD, certain NW arrays were located.

(Step 2) The sample was heated up in order to evaporate and entirely remove the GaAs NWs from the Si substrate. During this step, instrumental instabilities and thermal drift were studied. Accordingly, a stable condition for initiation of the NW growth was established.

(Step 3) The growth conditions were satisfied, and a newly growing NW was monitored employing in-situ time-resolved μXRD. Schematic sketch of the scattering geometry using the micrometer-sized X-ray beam at the GaAs substrate is illustrated in Figure 5.1. Here, a few nano-objects are simultaneously illuminated, which were angularly resolved on the detector plane.

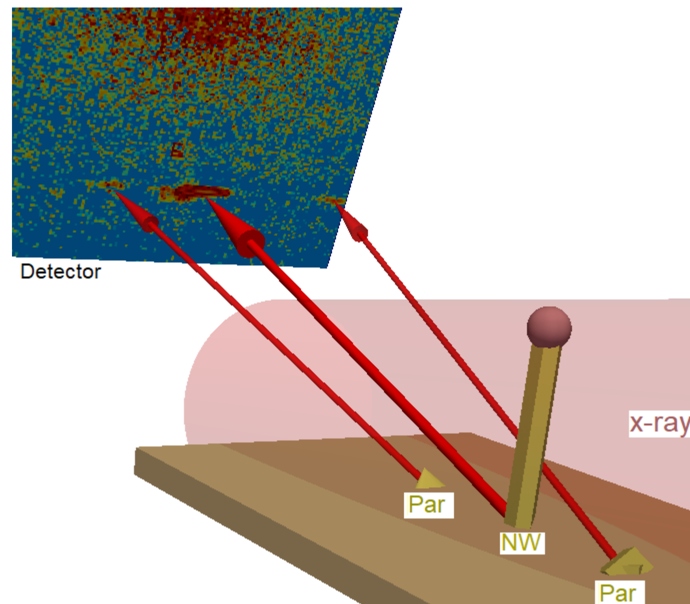

Figure 5.1: Sketch of the scattering geometry in this experiment at (111) Bragg reflection: the μm sized X-ray beam is illuminated from the right and focused at a specific growth region. The Bragg's condition is fulfilled for a NW and a few PIs (Par), respectively.

Step 1: Alignment of the X-ray micro beam onto pre-patterned nanowire sample

A FIB patterned Si sample after successful NW growth was used for alignment of the μm sized X-ray beam onto a NW growth region. An SEM micrograph of the sample at a subregion of NW growth is shown in Figure 5.2a with a yield of NW growth above 80%, NW mean diameter=47±10 nm, and NW length=1.18±0.12 µm. The details of the NW growth protocol are presented in the caption of Figure 5.2a. After SEM characterization, the sample was degassed (1 h, 300 °C, 10^{-7} mbar), and reloaded back into the pMBE chamber. The sample was used for positioning the X-ray beam at a certain NW array of interest (Figure 5.2a). The footprint of the beam at this scattering geometry could cover up to 10 holes due to the shallow angle of incidence at GaAs (111) (α_i = 7.274° at 15 KeV). Setting the GaAs(111) Bragg's condition (see Figure 3.3), the substrate was mapped by a raster scan (RS) in both sample in-plane directions. The angular positions of the goniometer were transformed into the coordinates of the reciprocal space (see Figure 3.3b and the corresponding text in Chapter 3). Therefore, the GaAs signal could be identified. Each pixel in Figure 3.3b corresponds to the integrated GaAs signal at each frame: GaAs scanning μXRD map of the sample (see caption of Figure 5.2b for more details). In this way, the X-ray beam was precisely positioned at a NW growth region on the sample.

Step 2: Prolonged Annealing for GaAs material removal and stabilization

After aligning the micrometer-sized X-ray beam onto a specific subregion on the sample, the NWs were entirely removed by a prolonged annealing step at a vacuum pressure within $1 - 5 \cdot 10^{-8}$ mbar consecutively first at 550±5 °C for 30 min and then at 610±5 °C for 2 hours. The complementary SEM studies proved that the GaAs material could fully evaporate from the patterned holes (cf. Figure 6.3a,c). However, GaAs material was more stable to thermal annealing at the marker regions. The FIB patterning details at the marker regions are discussed in Section 4.2.2 (see Figure 4.14). At the marker regions, a high density of epitaxial PI growth is observed after growth. After the annealing step, a small amount of GaAs residual material remains at the markers (see 5.3d). The GaAs residuals after annealing were detectable by both complementary SEM ex-situ studies, as well as the in-situ μXRD. In the latter, a visible but weak GaAs signal was received at the marker regions. On the other hand, the subregions of NW growth did not show any XRD GaAs signal after the annealing step (in agreement

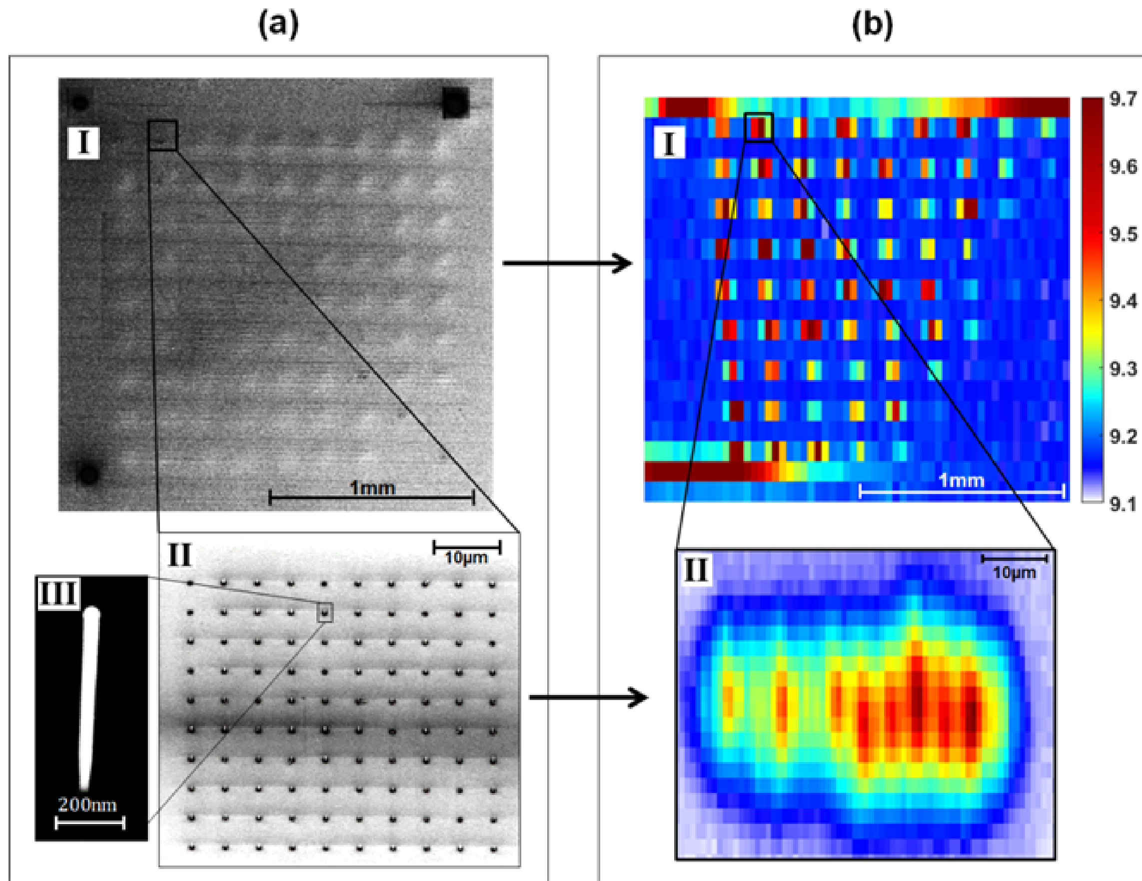

Figure 5.2: Panel (a) shows SEM images of the sample after the first growth run. The procedure of substrate preparation followed by HF 0.5% treatment, boiling the samples in deionized water for 1 min, degassing at a separated annealing chamber for 1 h at 300 °C within the 10^{-7} mbar range, and then transferring into the MBE chamber. Here, a second annealing step was performed (10^{-8} mbar range, 700±5 °C, 10 min). After ramping the substrate temperature down to a growth temperature of 590±5 °C, firstly, 45 ML of Ga was deposited, resulting in Ga droplets preferentially located in the FIB patterned holes. The NW growth was then followed by supply of As with a V/III ratio of 2 in order to initiate GaAs growth with a 2D growth rate of ∼50 nm/h. Panel (a-I) shows a low magnification top-view image from 81 subregions of growth onto which NWs are grown (compare that with Figure 4.10). Panels (a-II) and (a-III) show SEM images at 30° tilted substrate on the indicated subregion with $>$ 85 % yield of NW growth. Panel (b) shows the scanning μXRD map corresponding to the NW growth (sub)regions indicated in panel (a) with a logarithmic color bar. Here, each pixel contains the sum of GaAs(111) signal from 1−10 NWs at each frame. The scanning map in panel (b-I) is coarse (285 points.mm^{-2}), and in panel (b-II), that is fine ($26 \cdot 10^4$ points.mm^{-2}).

with the ex-situ SEM results in Figure 5.3a,c). Therefore, the GaAs signals from a few marker regions around the sample were used to study the behavior of the temporal drift. It was observed that the temperature-induced drifts were maximum during the temperature ramp-up and decreased by prolonged annealing duration. After 2 hours of annealing at 610±5 °C, the drift effects turned out to become sufficiently negligible.

Moreover, position and intensity of the Si peak (see Figure 3.3b) were studied all along the experiment which assured sufficient angular stability of the beam with respect to the sample. Because of the particular design of the patterned region, the relative distances of the marker to NW growth subregions were known. Therefore, the author used that to quickly relocate the micrometer-sized beam onto the patterned subregion of interest after stabilizing the system.

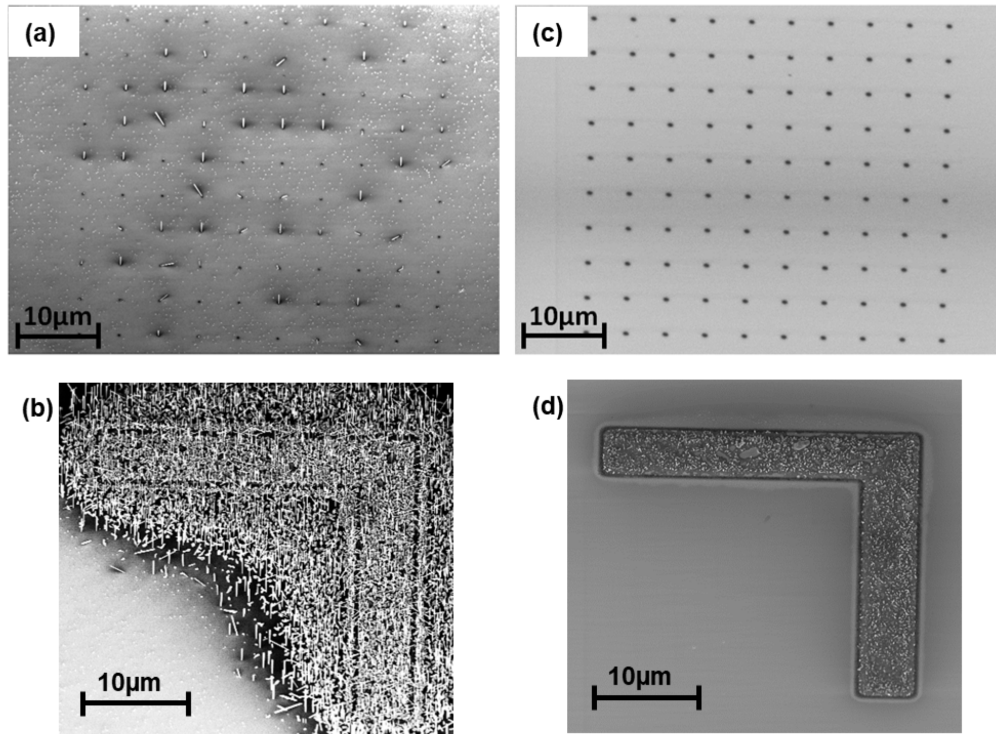

Figure 5.3: (a,b) SEM image of the 30° tilted FIB patterned substrate on which GaAs NWs were initially grown by the following procedure: after ex-situ and in-situ sample preparation with 1 min of HF treatment (see Chapter 4), 45 ML of Ga was deposited at 610±5 °C. Then NWs were grown at a Ga 2D rate of ~150 nm/h and a V/III ratio of ~2. Panel (a) shows the patterned holes and panel (b) shows a highly dosed FIB patterned region with uncontrolled growth, which is called "marker" in the text. (c,d) SEM image of the 30° tilted substrate grown at identical conditions as the sample in panel (a,b), then cooled down and stabilized at room temperature. The sample was then ramped up to 610±5 °C and annealed for 2 hours at a background pressure of $1 - 5 \cdot 10^{-8}$ mbar. The grown material fully evaporates at the subregions of NW growth and partially evaporates at the marker after the annealing step.

Step 3: Monitoring an individual growing nanowire using in-situ micro X-ray diffraction

At the FIB patterned subregion of interest, the NW growth was initiated by keeping the substrate temperature at 610±5 °C and introducing As molecular beam first up to a stabilized background pressure of $\sim 4{\cdot}10^{-7}$ mbar and followed by the supply of Ga. The growth was performed at a Ga rate of ~150 nm/h and a V/III ratio of ~2. After opening the Ga shutter, the growth was continued for a duration of 55 min. When a weak visible NW single appeared, raster scans in both in-plane directions of the sample were conducted to optimize the position of the X-ray beam with respect to the NW. Moreover, a 3D reciprocal space map (RSM) was performed to optimize the angular position of the NW with respect to the detection plane [1]. The μXRD was followed by keeping the position of the beam, sample, and detector constant. The exposure time at each frame was 1 s and considering the digital processing time (0.44 s per frame), the effective measurement time at each frame was 1.44 s. In order to check for any undesirable drift during the growth, beam realignment to the NW signal was repeated a few times along growth which re-confirmed that no drift was happening (see below for the analysis of data in Figure 5.13). By analysis of the signal, we will see that the angular orientation of the beam onto the sample was sufficiently stable during growth up to time=47 min. At this point, an RSM was performed. It appeared that the angular motor movement was not sufficiently reproducible in this type of experiment in signal intensity analysis but accurate enough in signal width (NW diameter) and position (angular misorientation) analysis (see Section 5.3). In Figure 5.4, two RSMs are shown from time=23 min and 47 min. Here, one could see the pixelized position of detection plane in the reciprocal space with respect to the NW signal. During growth, the evolution of the NW volume and length (reliable up to time=47 min), diameter, tilt angle, and crystal structure are extracted from the diffraction pattern of the NW signal.

[1] Since a 2D pixel detector is used, each detector frame cuts a slice in the reciprocal space. Accordingly, the angular position of each detector pixel approximately corresponds to a point within a gridded 3D matrix of q values along the conventional q_x, q_y, and q_z directions [156]. By rocking the sample, the incident angle of the beam on the sample changes. As a consequence, the slice position of the detector in the reciprocal space also changes. Notably, rocking the sample does not necessarily result in equally spaced volumetric pixels in the reciprocal space. Therefore, in order to visualize the data, the gridded transformed points at the reciprocal space are linearly interpolated in 3D.

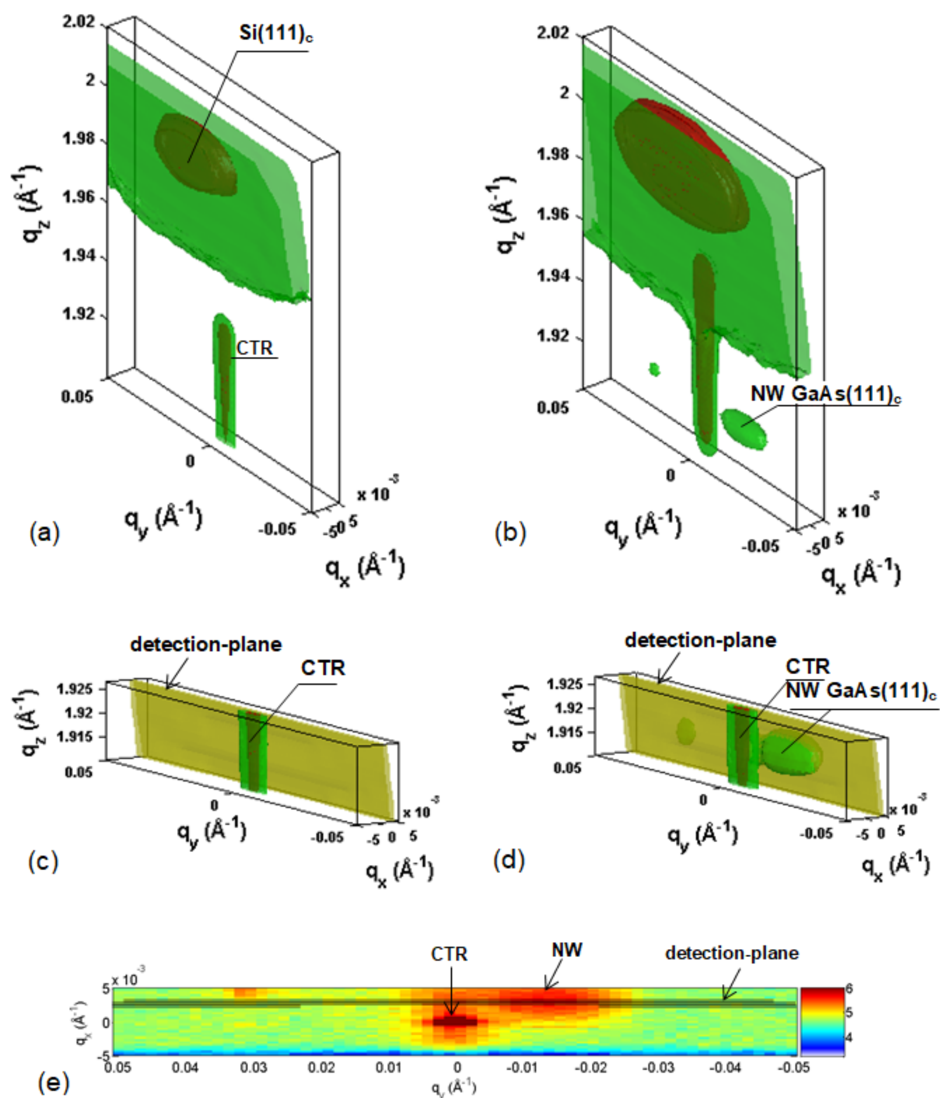

Figure 5.4: Three-dimensional diffraction intensity distribution close to the GaAs (111) reflection. The reciprocal space mapping covers a diffuse intensity of Si(111) at q_z close to 2 $\mathring{A}^{-1}$. The red and green structures represent iso-intensity surfaces. Panel (a) is taken before growth showing Si(111) and a part of the crystal truncation rod. Panel (b) is taken after ~47 min of growth showing an emerging GaAs NW signal at GaAs(111) reflection. Panel (c) and (d) are similar to panels (a) and (b), respectively, at a more narrow q_z range around the NW signal. The pixelized detection plane is shown in the reciprocal space. Panel (e) shows the integrated intensity of the full box in panel (d) along q_z axis where NW signal, crystal truncation rod, and the detection planes are indicated.

The subregion of interest after the in-situ growth experiment is shown in Figure 5.5a. Here, using the XRD mapping, the NW of interest was precisely located on the sample (blue circle in Figure 5.5a with high magnification in Figure 5.5b). The footprints of the X-ray beam at the μXRD geometry are indicated with red ellipsoids. The diffraction patterns corresponding to the red ellipsoids are shown in Figure 5.5c–d. As observed in Figure 5.5a the growth on the sample includes 7% of vertical NWs and 93% of tilted NWs and PIs. That can be related to the increased diameter of the holes after annealing, as discussed in Section 4.2. SEM images from a few PIs are shown in Figure 5.6. XRD signal from the PIs can be distinguished from the signal from NWs because PIs have much smaller lengths, which means an extended signal along q_z [157]. The XRD signal in Figure 5.5d includes several objects elongated along q_z which perfectly fit the SEM image from the corresponding region. In Figure 5.5c, the XRD signal is mainly from a single NW (concluded by signal analysis, see Section 5.3). The SEM image in Figure 5.5a at the inset of top red ellipsoid shows that a few other nano-objects are illuminated which are mainly tilted NWs. As is shown in Chapter 6, the Bragg conditions for tilted NWs (even in case of epitaxial correlation with substrate) can angularly deviate from that of straight NWs.

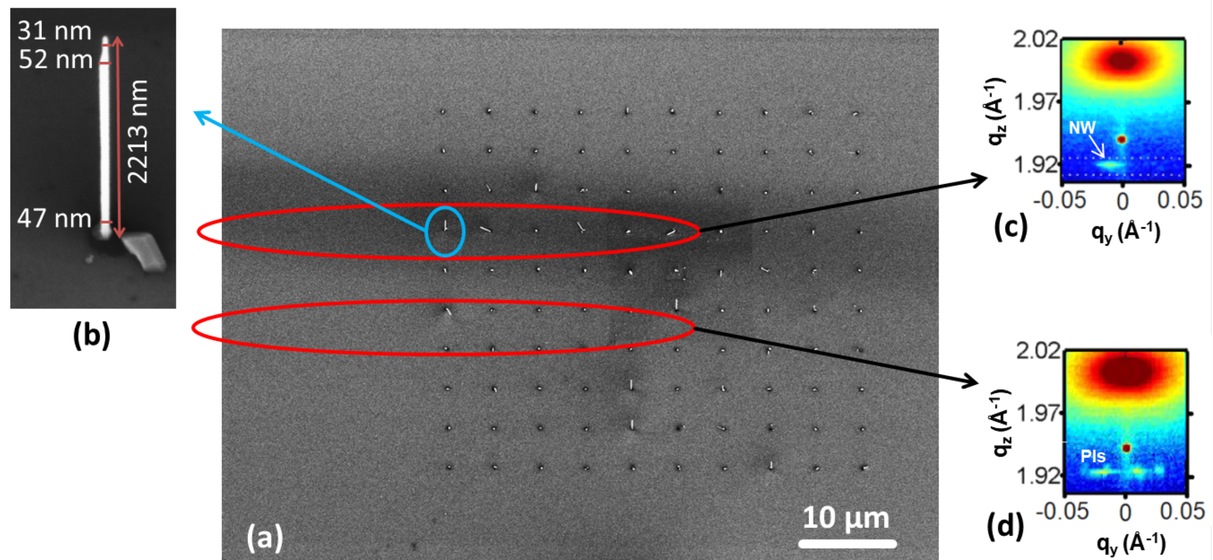

Figure 5.5: (a) Aftergrowth SEM image of the NW region at 30° tilted substrate. The blue circle in panel a indicates the NW of interest which was monitored during the in-situ study with a magnified SEM image at panel (b). The red ellipsoids in panel a are the footprints of the X-ray beam at the μXRD geometry. Panels (c) and (d) show the intensity distribution of the corresponding detector images transformed into the reciprocal space from regions within the red ellipsoids. Panel c shows that the Bragg conditions are satisfied mainly for a single NW, and panel d shows that several PIs are at Bragg conditions. The detector images in panels c and d are acquired at the timestamp of 47 min.

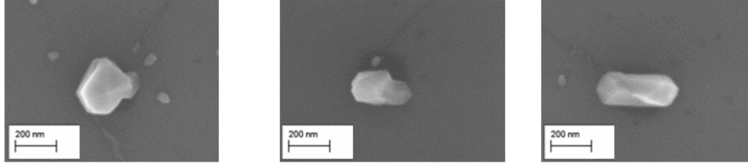

Figure 5.6: Top-view SEM image of the PIs grown on the FIB patterned holes. The diameter and height of the PIs are in the range of 200 nm which means that in the reciprocal space they have smaller q_y and larger q_z elongation as compared to the NW signal with close to 50 nm diameter and few μm length.

5.2 Results and analysis

Evolution of the intensity distribution around GaAs (111) Bragg reflection at the NW of interest are shown in Figure 5.7a–d in some selected detector frames. At $q_y = 0$ the crystal truncation rod of the Si is observed. The NW signal appears near GaAs(111) Bragg reflection identified by elongated strikes along q_y and narrow elongation along q_z (see Figure 5.7b). The NW peak is located at q_y<0 meaning that the NW is slightly tilted (see Figure 3.3). In a symmetric Bragg reflection, the magnitude of the momentum transfer wave-vector is:

$$|\overrightarrow{q}| = q_z = {}^{2\pi}/_{a_d}. \tag{5.1}$$

where a_d is the interplanar spacing between diffraction planes. As discussed in Chapter 2 (Table 2.1), interplanar spacing of GaAs ZB(111) and WZ(002) are $a_{d-ZB(111)} = 3.2641\,\text{Å}$ [158] and $a_{d-WZ} = 3.285\,\text{Å}$ [66]. Therefore, we have: $q_{z\,ZB(111)} = 1.925\ \text{Å}^{-1}$ and $q_{z\,WZ(002)} = 1.9127\ \text{Å}^{-1}$. Along q_z, as indicated in all panels in Figure 5.7b–d, the NW signal lays between pure ZB and WZ marked by dotted lines. This is due to mixture of phases within the NW [57]. The 2D intensity distribution acquired at the timestamp of 22 min was accounted as the background signal, and therefore, it was subtracted from all the detector frames (see Figure 5.7e–f). Note that the 2D intensity maps at each frame are normalized to the X-ray beam current which had < 1 % fluctuations.

In order to analyze the NW signal, a 2D Gaussian [159] was fitted to the NW and Si signals at each frame (see Figure 5.8a). The integrated intensity of the NW GaAs(111) signal as well as the diffuse Si(111) is plotted as a function of time in Figure 5.8b. Here, the overall trend of the Si(111) intensity is constant except for some small deviations. Angular instabilities of the X-ray beam are probably responsible for the latter. The minor fluctuations, seen in the Si(111) signal, are reflected in the trend of NW integrated intensity but without a significant impact on the general trend/functional behavior of

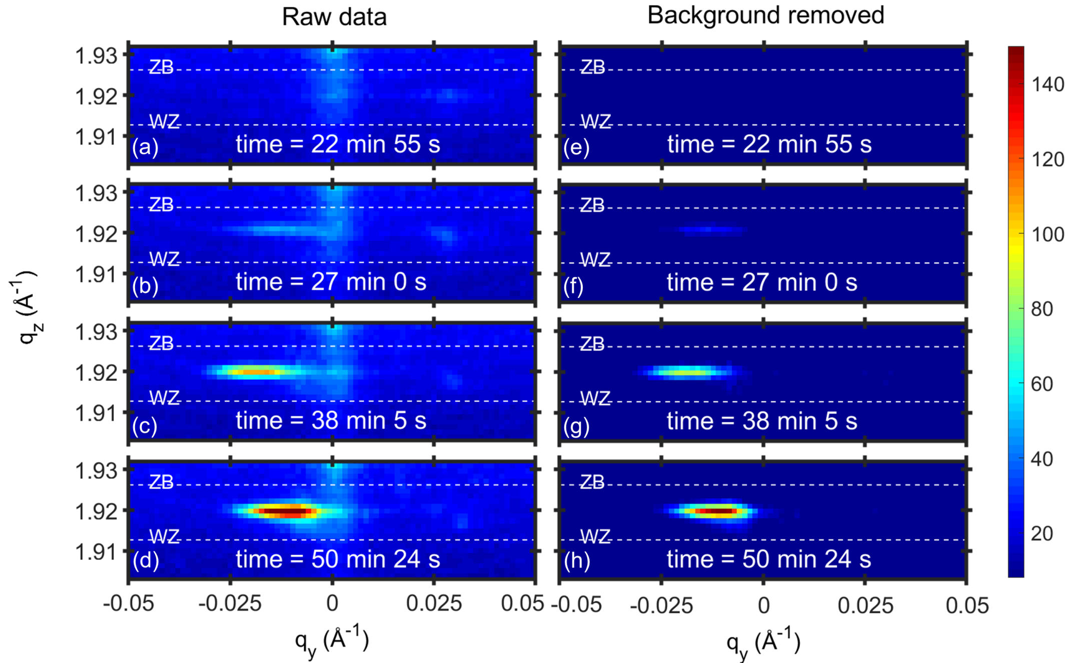

Figure 5.7: Panels (a−d) show four representative detector frames transformed into the reciprocal space. Panels (e−f) show the detector frames after background removal. 2D intensity distribution at about time=22 min was accounted as the background and subtracted from all detectors. The color bar at the right is linearly scaled and belongs to all detector frames.

the NW growth (e.g., cf. Si and GaAs signals in Figure 5.8b at time $>$ 50 min). As one observes in Figure 5.8b, the uncertainty around the data points are relatively high originating in the signal to noise ratio. In order to gain a higher signal to noise ratio, ten frames were integrated and averaged, leading to 14.4 s effective integration time per frame and reduced error bars.

In Figure 5.9a, the intensity distribution around GaAs(111) is plotted in a logarithmic color scale (cf. Figure 5.8b and Figure 5.9a). An additional signal is indicated in Figure 5.9a and assigned to a PI. Note that this PI signal is not visible in a linear color scale in Figure 5.8b since its intensity is at least 10 times less than the NW signal. The curve fitting procedure in Figure 5.8 was repeated with 1D Gaussian fitting. Here, the 2D intensity distributions at each frame is integrated along q_y or q_z within a box around the NW signals in order to generate 1D line profiles. Due to integration, the signal to noise ratio considerably increases, causing access to the PI signal along growth. The integration along q_z and q_y are referred to as q_y and q_z profiles, respectively, exemplified in Figure 5.9b and 5.9c, respectively. It is clearly observed in Figures 5.9b−c that the NW is broader along the q_y profile and narrower along the q_z profile as compared to

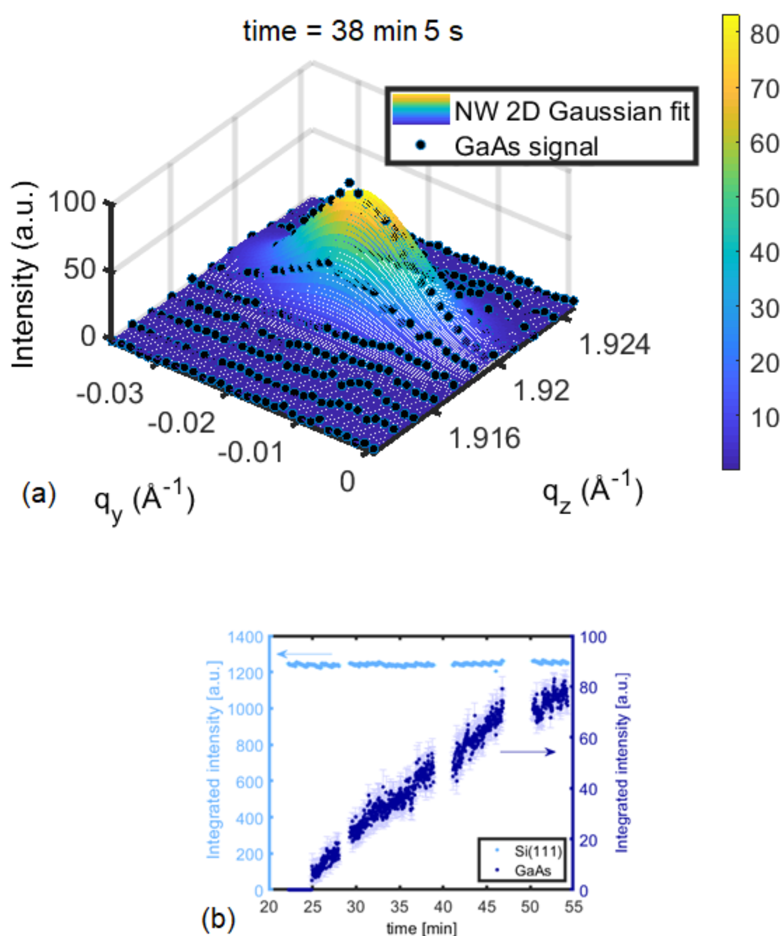

Figure 5.8: (a) Two-dimensional Gaussian fitting of the GaAs signal at the q_y-q_z intensity distribution at the detector frame acquired at time=38 min and 5 s. (b) The integrated intensity of the NW signal during growth: 1.4 s effective time per frame. Here, light blue is the Si signal (left axis); dark blue is the GaAs NW signal (right axis). On the gaps, RSM and/or RS is performed.

the PI signal. That is in agreement with the expectation as revealed from the SEM results shown above. From each 1D profile along q_z and q_y, the NW and PI contributions were extracted as shown in Figure 5.9 and compared to the 2D Gaussian fit parameters along both q_z and q_y directions. The NW peak characteristics extracted from both approaches were in perfect agreement; however, the PI characteristics could be extracted better from the 1D profiles, as explained above. Therefore, the 1D profile fitting is the basis of the analysis below.

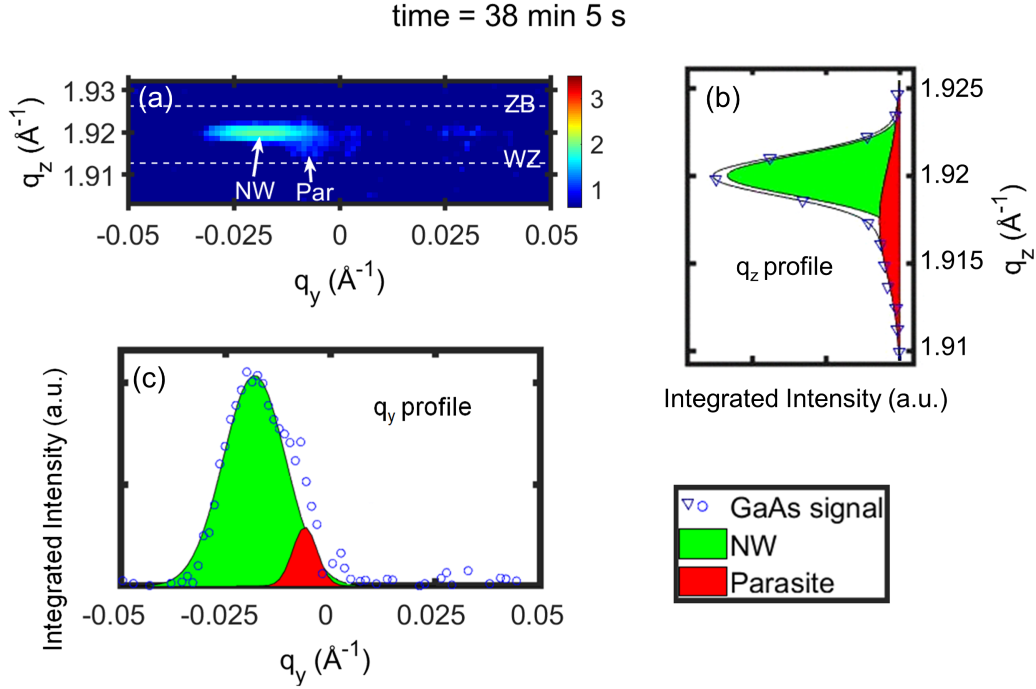

Figure 5.9: Signal analysis at time=38 min and 5s: (a) detector frame around the NW signal at a logarithmic color bar (see Figure 5.8b for a linear color bar). The GaAs peak analysis is performed by 1D Gaussian fitting after integrating the signal within a box along q_y in panel (b) and along q_z in panel (c). The peaks assigned to a NW and a PI are indicated in green and red, respectively.

q_z – profile analysis (structural evolution):

The q_z–profile analysis is not the main strength of the implemented experiment. However, we give an insight into the NW structural evolution. Figure 5.10a depicts the evolution of the q_z–profiles after background removal along growth. The time-resolved central position of the NW and PI Gaussian fits are plotted in Figure 5.10b (blue data points). The dotted lines are the nominal pure WZ and ZB q_z values. The central position of Si diffuse scattering is plotted in red (left axis) where $\triangle q_z$ is deviations of the Si signal from its nominal value ($q_z = 2.002\,\text{Å}^{-1}$) at each detector frame. Note that the left and right axes are equally scaled which shows that the Si peak is stable all along the experiment (the setup is stable). However, the NW peak position continuously decreases in q_z by increasing the time. In the case of a mixture of different polytypes, the phase contributions can convolute to one common peak [77]. Here, two types of phases are assumed within the NWs as normally observed in TEM studies of self-catalyzed GaAs NWs [155, 58, 29, 160]. Accordingly, one can define a super cubic lattice distance, d_{sc}, as following:

$$d_{SC} = \mathrm{X}{\cdot}a_{d-\mathrm{WZ}(111)} + (1-\mathrm{X}){\cdot}a_{d-\mathrm{ZB}(111)}, \tag{5.2}$$

where X is the number ratio of planes with WZ stacking in the NW. In the next step, $d_{SC} = {}^{2\pi}/_{q_{NW}}$ is substituted based on equation 3.22 where q_{NW} is the center of the NW q_z profile. Thus, the evolution of X during growth can be evaluated from the measured peak position by:

$$X = \frac{{}^{2\pi}/_{q_{NW}} - a_{d-\mathrm{ZB}(111)}}{a_{d-\mathrm{WZ}} - a_{d-\mathrm{ZB}(111)}}. \tag{5.3}$$

Figure 5.10d shows the temporal evolution of X during NW growth. Here, the increasing WZ percentage by time from an initial value of 27% up to about 45% indicates that the newly growing GaAs has higher probabilities for nucleation of WZ phase. On the other hand, the PI signal appears at a different q_z value indicating a different polytypism with little deviation along the growth.

q_y – profile analysis (nanowire volume, diameter, length, and angular misorientation)

The time evolution of the q_y-profiles after background removal is illustrated in Figure 5.11a. In Figure 5.11b,c, and d, the Gaussian fitting parameters of integrated intensity, fwhm, and center along the q_y-profiles are presented, respectively (see the y-axes on the right). These fitting parameters are related to volume, diameter, and β tilt angle, as shown at the left axes of Figure 5.11b,c, and d, respectively. Considering the NW volume and diameter, the NW length is extracted.

The minimal scattering volume corresponding to ZB(111) and WZ(002) reflection for the given μXRD scattering geometry is estimated in ref. 75 to be $V_{ZB} = 1.96 \times 10^4 \pm 0.55 \times 10^4$ nm^3 and $V_{WZ} = 4.16 \times 10^4 \pm 1.10 \times 10^4$ nm^3, respectively. Here, the characteristics of the X-ray beam at P09 beamline are taken into account to extract the dependency between the scattering intensity and volume. Given that the NW structure is approximated by a mixture of WZ and ZB phases, the minimum scattering volume is estimated to be:

$$V_{NW} = X{\cdot}V_{WZ} + (1-X){\cdot}V_{ZB}, \tag{5.4}$$

where V_{NW} is the minimal scattering volume of NW with X% of WZ content. The initial signal of the NW appears at $q_z = 1.922\,\text{Å}$ leading to an approximated content

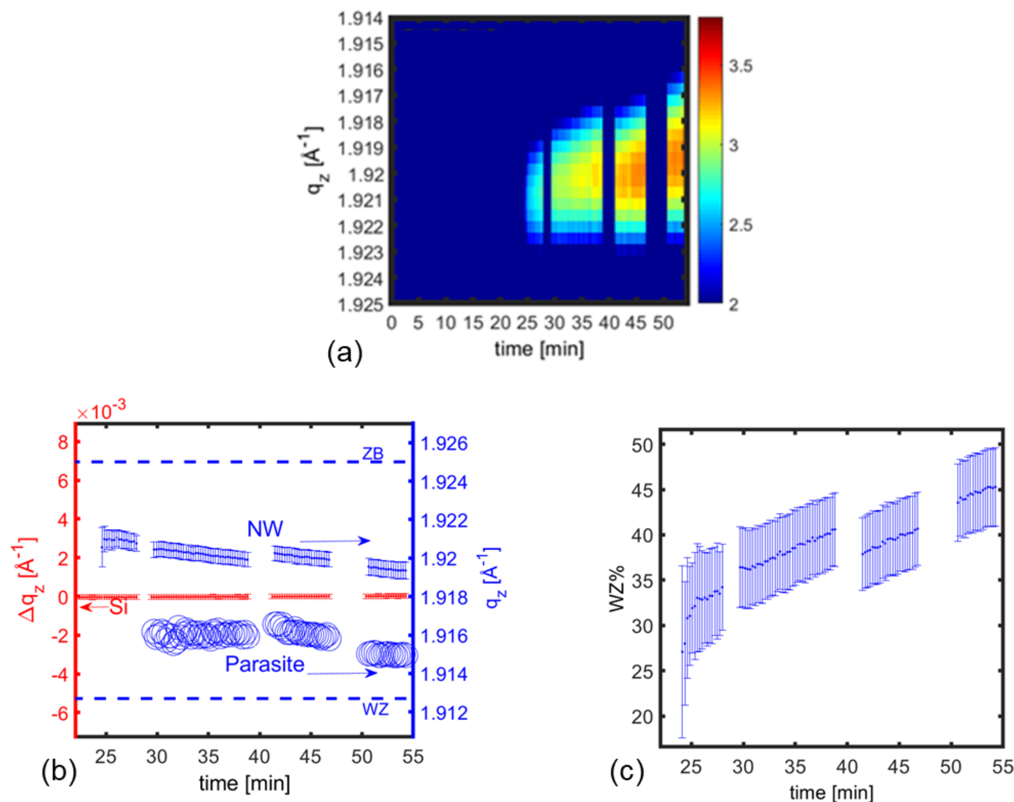

Figure 5.10: (a) Time-resoled intensity distribution of the q_z–profiles after background removal: 14.4 s effective time per q_z–profile. On the gaps, RS and RSM are performed. The color scale is logarithmic. (b) Time-resolved evolution of the central position of q_z–profile Gaussian fits for the Si (red) at the left axis and for NW and PI signals (blue) at the right axis. Nominal positions of pure WZ and ZB are indicated in dash lines. (c) Time-resolved WZ% at the NW along the growth.

of 27% WZ within the NW (see Figure 5.10b−c). The minimum scattering of the NW at 27% WZ is about $2.36 \times 10^4 \pm 0.91 \times 10^4$ nm^3. The integrated intensity of the first GaAs signal (at about 24 min) is accounted to be the mentioned value of the minimum scattering volume. Accordingly, the overall integrated intensity curve is normalized and related to the scattering volume of the NW in Figure 5.11b [2].

Considering the finite shape of the NW, the width of the diffraction peak is related to NW diameter. Because the width of the probing beam is larger than the scattering objects, the diffraction pattern is the Fourier transform of the scattering object. As estimated in Chapter 3, the relation between the fwhm of the central peak along q_y, and the NW diameter, D, is $D \approx {}^{1.68 \cdot \pi}/_{fwhm}$. Accordingly, the evolution of the mean

[2]Note that in the volume calculation, the beam shape is not considered.

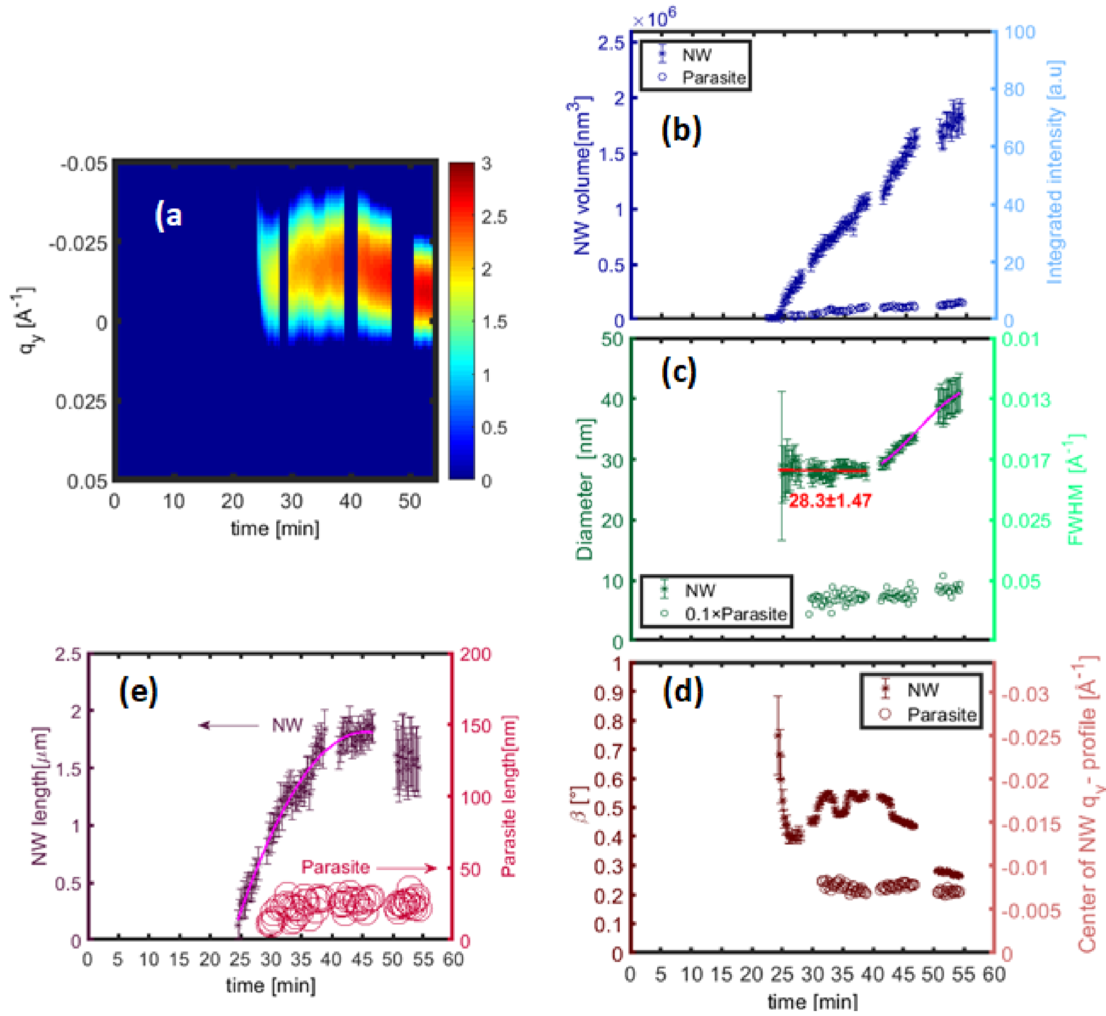

Figure 5.11: (a) The intensity distribution of the NW Gaussian fits along q_y–profiles after background removal with 14.4 s effective time per frame. On the gaps, RS and RSM are performed. The color scale is logarithmic. (b) Time-resolved scattering volume evolution of the NW and PI signals at the left axis (integrated intensity at the right axis). (c) Time-resolved diameter evolution of the NW and PI at the left axis (fwhm at the right axis); the red line is a linear fit at time $<$ 40 min which gives a mean NW diameter of 28.3±1.5 nm. The hot pink line is a polynomial fit for t $>$ 40 min for eye guide. (d) Time-resolved angular misorientation of the NW and PI with respect to the surface normal at the left axis (central position of the q_y–profile Gaussian fit at the right axis) (e) The NW and PI length evolution during growth.

diameter of the NW and the PI has been estimated as a function of growth time (see Figure 5.11c). The red line is a linear fit to the diameter of the NW at time $<$ 40 min. The slope of the fit is almost zero, with a value of D=28.3±1.5 nm. For the NWs with deviating NW diameter, the fwhm observed in an experiment illuminating the full NW

is reversely proportional to the volume average diameter, D, defined by:

$$D = \frac{\int D'(z)A(z)dz}{\int A(z)dz} \tag{5.5}$$

where D' is the NW diameter, and A is the cross-sectional area, which both depend on the z-coordinate along the NW axis [58]. In Figure 5.11c, the NW diameter at time > 40 min increases which can be explained by the onset of radial growth approaching a value of $D = 41.1 \pm 3.1$ nm at the end of NW growth. This is in good agreement with the volume average diameter extracted from SEM after growth (see Figure 5.5b). The diameter of the PI is also extracted. Note that the PI diameter is divided by a factor 10 for a better visualization in 5.11c. The average diameter of the PIs grown at the footprint of the X-ray beam (Figure 5.5b) shows that likely the PI signal comes from the PI which is grown near the NW in Figure 5.11c. Here, the averaged diameter after the growth is about 100 nm and agrees with the final diameter of the PI in Figure 5.11c.

The center of the q_y–profiles is a measure for the mean angular orientation angle β of the NW growth axis with respect to the substrate surface normal. As discussed in Chapter 3, β measures the projected tilt at the detector plane using equation 3.6. Given the pixel size of the detector and the scattering geometry, β can be determined with a resolution in centi-degree range ($0.01° \approx 2 \cdot 10^{-4}$ rad). At $27\,\text{min} < \text{time} < 40\,\text{min}$, β oscillates. However, at time > 40 min, β continuously decreases toward $\beta \approx 0$, where at the same time, the NW diameter increases. That indicates a stabilization of NW orientation for increasing diameter. In contrast to the NW, β angle of the PI is rather constant.

Using the evaluated NW volume, V, and NW diameter, D, the NW length, L, is extracted by assuming a simplified cylindrical shape for the NW: $L = V/(\pi \cdot (D^2/4))$, shown in Figure 5.11e. Here, uncertainties of the length are calculated using error propagation, assuming that the measured volume and diameter are uncorrelated.

$$\Delta L = L \cdot \sqrt{2(\frac{\Delta D}{D})^2 + (\frac{\Delta V}{V})^2} \tag{5.6}$$

Within a range of 25 min $<$ time $<$ 45 min, the length, L, evolves by a function:

$$L = -3.71 \times \text{time}^2 + 338.7 \times \text{time} - 5913. \tag{5.7}$$

where the units of L and time are nm and min, respectively. The slope of the curve in this period gives a rate, R, of axial NW growth to be:

$$R = -7.4\times\text{time} + 338.7. \quad (5.8)$$

where the unit of R and time are nm/min and min, respectively. Diameter and length evolution at Figure 5.11c and e show that at time $<$ 40 min, the NW dominantly grows axially (diameter stays almost constant), but at time $>$ 40 min, the NW volume increases mainly by radial growth. At the timestamp of 30 min, R is 117 nm/min (1.9 nm/s). By extrapolating the length curve at L =0, the incubation time of the NW growth is calculated to be about 23.5 min. That is about 0.5 min after the acquisition of the first NW signal (time = 24 min 7 s). Because the minimum scattering volume for visibility (see above) is $\sim 2.36 \times 10^4 \pm 0.91 \times 10^4$ nm^3 and D is $\sim$28.3$\pm$1.5 nm, the NW length corresponding to the first visible NW signal is calculated to be 37$\pm$26 nm. The height of the PI is shown at the right axis. Although with large uncertainty, the height is less than 50 nm which is in agreement with the average volume height of the PI extracted from the SEM micrograph in Figure 5.5b.

Further analysis

Because it is revealed that the NW is angularly instable within the detection plane (along q_y), angular movement of the NW perpendicular to the detection plane (along q_x) can not be excluded. In the following, the author discusses the likelihood that such an angular movement along q_x affects the NW characteristic curves in Figure 5.11. In Figure 5.4d−e, in order to perform the RSM scan, the sample is rocked, meaning that the X-ray incident angle changed in steps acquiring several frames. In those frames, the position of the detection plane moves mainly along q_x. To visualize, one could consider that the pixelized detection plane in Figure 5.4d moves through the NW 3D signal perpendicular to q_x and parallel to q_y. That allows for accessing to different cuts through the NW 3D peak. Those frames are analyzed by curve fitting of the NW 2D peak. In the following, the NW signal in 3D and 2D (within the detection plane) are referred to NW 3D signal and NW 2D peak, respectively. In Figure 5.12, the integrated intensity (left y-axis) and fwhm (right y-axis) of the NW 2D peaks are extracted. The x-axis ($\triangle q_x$) is the relative position of the detection plane with respect to the center of the 3D NW signal along q_x. It is revealed that a relative movement of the NW peak and detection plane along q_x, affects the intensity of the NW 2D peak. For example, by relative movement of about 0.003 Å^{-1} and 0.004 Å^{-1} along q_x, the NW intensity

collapses by 70% and 95%, respectively. On the other hand, the fwhm seems to be much less sensitive to such a movement. In particular, in order to estimate a considerable change in fwhm of the NW 2D peak, the intensity must collapse by 95% (see indicated dashed lines in Figure 5.12). Because the intensity curve in Figure 5.11b does not undergo any visible decrease of intensity along NW growth (consistently increases), one can conclude that the NW diameter is reliably acquired. Moreover, the data point at time=47 min in Figure 5.11b is acquired from the RSM of the NW, which follows the intensity trend. In particular, the detection plane at the central cut of the NW is extracted from the RSM and taken as a data point. Therefore, it is concluded that the volume curve is also sufficiently accurate. As a result of this analysis, it is found that the NW angular position along q_x has been sufficiently stable along the growth.

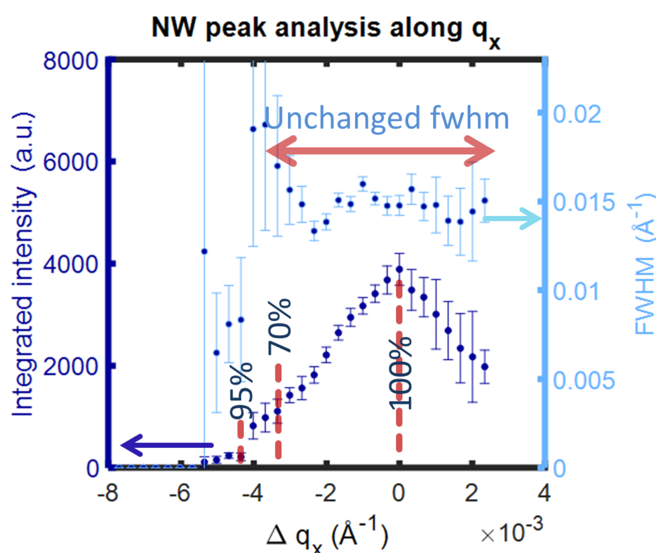

Figure 5.12: NW 3D signal analysis at 2D cuts along q_x. In other words, the detection plane moves with respect to the center of NW 3D signal. The NW peak is identified within the detection planes and the NW intensity and fwhm is extracted.

In Figure 5.13, the results of the RSs during the in-situ experiment are shown. In Figure 5.13a, the red ellipsoid shows the footprint of the X-ray beam at the experimental geometry. The blue circle shows the NW of interest. X and Y are the in-plane directions of the sample. At the RSs, the sample moved along X- and Y-directions until the NW signal entirely vanished on both ends. Note that in Figure 5.13a the X-ray beam is illuminated at about 7.27° incident angle leading to extending footprint. The results of three RSs along Y-direction (different timestamps during the in-situ experiment) are shown in Figure 5.13b. The vertical dotted line indicates the position of the NW

of interest along Y-axis. From the position of the Gaussian fits (see Caption of the Figure), it is observed that the beam position is stable along the experiment. The RSs along X-axis are shown in Figure 5.13c performed at three different timestamps. The maximum intensity of the NW peak along X-axis is shifted during NW growth (compare green and red data points corresponding to 28 and 39 min of growth, respectively). To discuss that, Figure 5.14a shows the horizontal and vertical beam shapes redrawn from ref. [75].

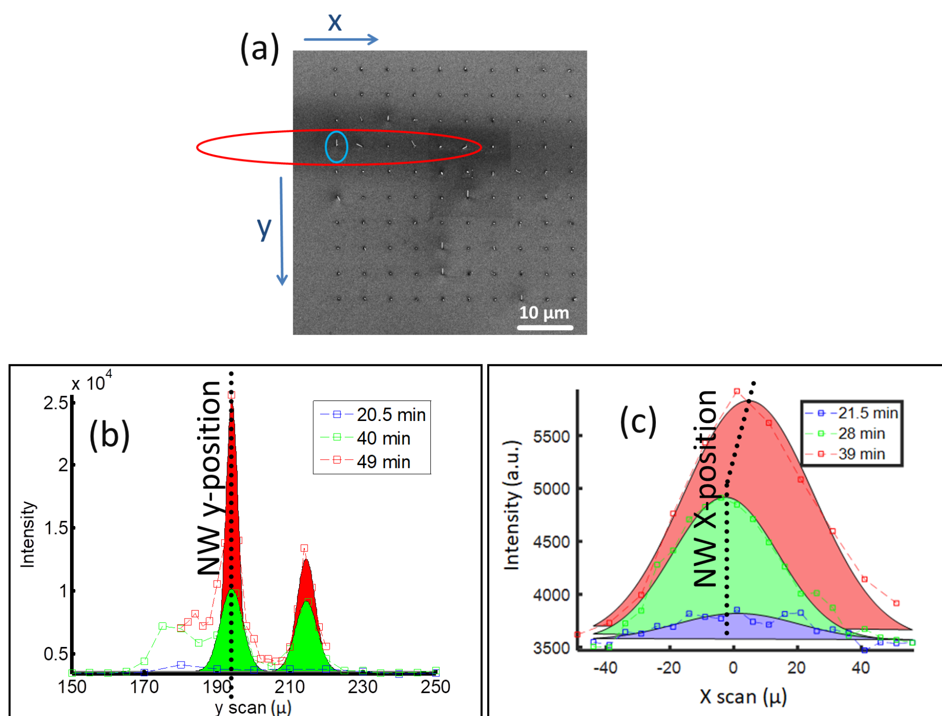

Figure 5.13: Raster scans along both in-plane directions of the sample resulted in the movement of the footprint of the X-ray beam with respect to the sample. In panel (a), 30° tilted SEM image at the NW growth region is shown. The footprint of the X-ray beam (red ellipsoid) and the NW of interest (blue circle) are indicated. The so-named X and y in-plane directions are indicated. As a consequence of the RSs, the intensity at the detector image around GaAs Bragg peak is plotted as a function of sample position along X in panel b and along y in panel c. Along the y-axis, several nano-objects are illuminated. Along the X-axis, the intensity of the NW peak is extracted and plotted. The solid peaks are Gaussian fits at the data points containing a specific nano-object identified by the signal shape.

Figure 5.14b illustrates a 2D scheme of the X-ray beam at its horizontal direction (along X-direction). According to equation 5.7, the NW length after 28 and 39 min of growth is about 0.6 μm and 1.6 μm, respectively. Figure 5.14c and d show a schematic illustration of the NW with different lengths at those growth times. It is schematically shown that increased NW length can result in asymmetric illumination of the NW, i.e.,

illumination of the NW with the tail of the X-ray beam. Therefore, readjustment of the beam with respect to the NW is required in order to acquire maximum illumination. That is fulfilled by moving the sample along X-axis as schematically shown in Figure 5.14d. The author believes that this is the reason for the corresponding observation in Figure 5.13c. Here, the fwhm of the X-RS is a convolution of the vertical beam shape and the length of the NW. The Gaussian fits in Figure 5.13c have fwhm of 38.9±3.1 μm and 48.2±4.5 μm for the green and red data points, respectively. In particular, the difference between the fwhm of the Gaussian fits directly reflect the NW length growth projected to the sample surface. Therefore, the deduction result ($9.3 \pm 1.1\,\mu$m) should be multiplied to tan $7.274° = 0.13$. In this way, based on the X-scan experimental data, and independent from our analysis analogy in Figure 5.11, it is revealed that the NW length has grown to $1.17 \pm 0.14\,\mu$m. This ascertains the NW volume and length characteristic curves in Figure 5.11 very well.

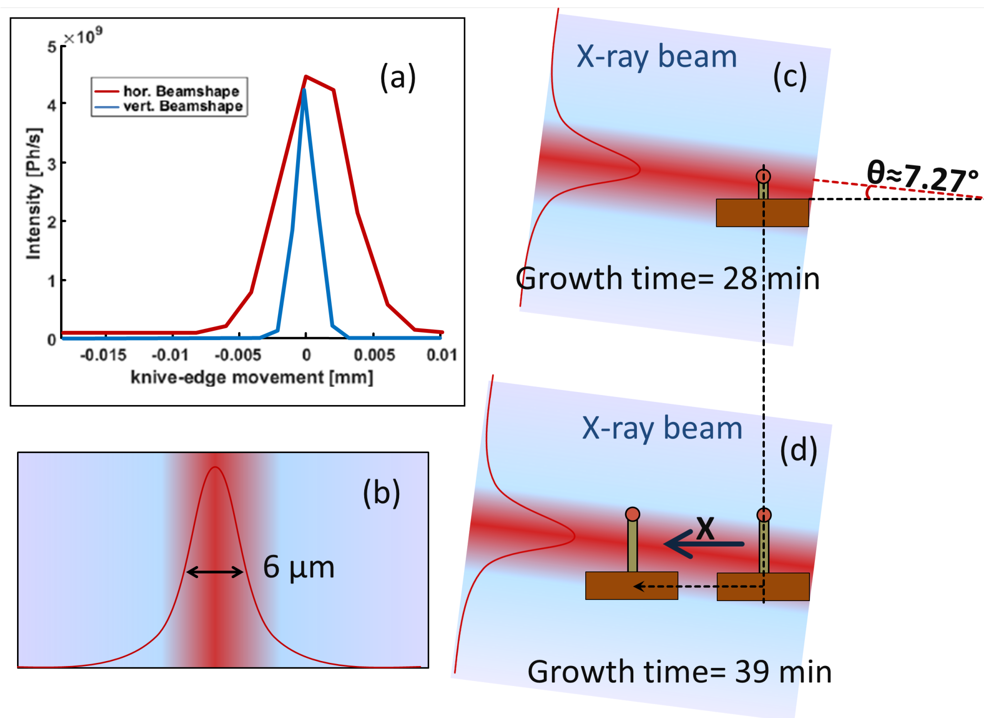

Figure 5.14: (a) Horizontal and vertical X-ray beam shape determined by knife-edge scans redrawn from ref. [75]. (b) Scheme of the vertical beam shape showing that the fwhm of the beam is about 6 μm. (c) Scheme of the illumination of the NW at its early stages of growth in symmetric (111) Bragg angle ($\theta \approx$7.27°). (d) Scheme of the illumination of the NW after 39 min of growth, illustrating that the NW length grows by time. Accordingly, in order to receive maximum intensity, the position of the NW with respect to the beam should be readjusted. That is performed by moving the sample along the X in-plane axis.

5.3 Discussion

Before initiating the supply of materials for NW growth, the sample was kept at the growth temperature for a total duration of 2 hours. That was the key to stabilize the system and setup. In this way, we examined and assured the angular and spatial stability of the beam with respect to the sample. The analysis of the stability tests during NW growth in Figures 5.12, 5.13, and 5.14 shows that the NW characteristic curves are acquired successfully. In particular, the evolutions of structure, size, and misorientation of an individual growing NW were resolved.

In the present work, it is shown for the first time that there is a competition between axial and radial growth within an individual NW. In particular, in Figure 5.11, for about 15 min after NW nucleation, the source material is used up for axial growth, and therefore, the radial growth is almost diminished (cf. Figure 5.11c and e at 25 min $<$ time $<$ 40 min). On the other hand, during the radial growth of the NW, the axial growth rate decreases (cf. Figure 5.11c and e at time $>$ 40 min). It has been formerly reported that the nano-objects which grow close to each-other compete for source material by overlapping the precursor collection volumes of group V species or diffusion areas of group III species [105, 161]. Such an analogy is acquired based on ex-situ studies or in-situ ensemble studies. In ex-situ studies, the growth on different samples is compared where numerous uncertainties exist, similar to the results in Section 4.1. In ensemble in-situ studies, the averaged behavior of NWs is accessed. Therefore, in both cases, the size evolution of specific single objects stays unknown. According to such studies, it is reported that the NWs with smaller diameters have a higher axial growth rate at NW systems with limited precursor material [162]. In other words, in order to have similar axial growth rates, the thicker NWs consume a higher amount of precursor material which might not be locally available at the collection volume of a NW. The NW growth rate in the present study decreases by increasing diameter. To summarize the points, first, the supplied material is consumed for radial growth at time $>$ 40 min, which locally decreases the material supply for NW axial growth. Second, the NW diameter increases, which means that more material supply is required for keeping the axial growth rate constant. As a result, the radial and axial growth of the NW compete with each other.

The driving force for the initiation of radial growth could be related to the diffusion length of Ga adatoms [163, 164]. At increased NW lengths, the diffusing Ga adatoms (i.e., a significant fraction of available Ga) can not migrate up to the NW top fact (111) under the Ga droplet to contribute in NW growth; and therefore, they incorporate in

the relatively less stable {110} NW side-walls [129].

At the footprint of the illuminating beam in Figure 5.5, a few PIs are present. In the analysis of the results, we assume that the PI signal, which appears near the NW signal in the reciprocal space, is the one which is shown in Figure 5.5b in the real space. The height and diameter of the PI in Figure 5.5b fit the diameter and height extracted from the XRD signal. As mentioned in the results section, the characteristic curves from the PI do not significantly evolve at prolonged growth durations (see Figure Figure 5.10 and 5.11 at structure, diameter, length, and angular orientation curves). For example, the integrated intensity (volume) of the PI saturates about 10 min after the appearance of the PI signal (nucleation). During the in-situ growth studies shown in this and the next chapter, the author monitored the growth of a few PIs. It was observed that within a few minutes, the final volume of the PIs is reached. That indicates that the facet growth (VS mechanism) of the PIs takes place at much lower rates compared to the VLS growth rates at the implemented growth parameters. In other words, the growth conditions are optimized for VLS NW growth.

The structure analysis is based on the assumption that the self catalyzed GaAs NWs usually grow with WZ and ZB phases reported for growth on Si [155, 58] as well as growth on GaAs substrates [29, 160]. XRD analysis of the mixture of WZ and ZB phases is reported in refs. [57, 96] for an ensemble of thousands of NWs. In the current work, a single NW is analyzed based on a theoretical model for a mixture of phases. In this way, it was revealed that the WZ content within the NWs increases along growth up to about 45%. That is related to the specific growth parameters, which is used [165, 42, 155] and again indicates a local deviation of growth parameters by increased NW length.

An outstanding aspect of the presented data is the angular misorientation of the NW during growth. In particular, β tilt angle of the NW could be determined with a resolution in centidegree range ($0.01° \approx 2 \cdot 10^{-4}$ rad). One could acquire a physical feeling for this angular misorientation by putting a piece of paper (thickness of 0.1 mm) under one side of a cupboard with half a meter width. Assuming that the paper is rigid and the height of the cupboard increases on one side for about 0.1 mm, the cupboard tilts about 0.01° with respect to its upright orientation. At a NW with a diameter of 30 nm, one has to increase the height of the NW on one side for about 0.05 Å. It is evident in the presented results that the NW tilts back and forth within 0.1° tilt angle. That is, in fact, a movement of the height of NW at one side about 0.5 Å similar to the cupboard example. We will see in the next chapter that the NWs tilt during annealing. The NW tilting is accompanied by shrinkage of the NW diameter. The regrowth of the same

NW results in the realignment of the NW along its surface normal. It seems like that the base of the NW undergoes tension also along NW growth, which is likely minimized by diameter growth. This small deviation (within $0.01°-0.1°$) of the NW orientation can be attributed to the movements of dislocations at the NW interface. Dislocations exist at the interface of GaAs and Si due to the 4.1% of lattice mismatch. They have been observed at the interface of Si substrate and GaAs layers [166] as well as GaAs NWs [17]. The dislocations can move at increased temperature. Challahan et al. have recently documented thermally driven movement of dislocations of GaAs layers on Si [166]. The small movement of the crystal structure by movement of dislocations is well known. However, to the best of my knowledge, an XRD study which quantifies local tilt of the structure around the dislocation is missing in the literature. The increased NW diameter seems to re-arrange the NW base and result in tilt of the NW toward surface normal.

5.4 Conclusion

In this chapter, the dynamics of growth of an individual GaAs self-catalyzed NWs is studied for the first time utilizing μXRD. In order to perform this highly sophisticated experiment, several technical considerations are realized. Methods and theoretical insights are also presented in order to extract NW characteristics from XRD signal. In particular, volume, diameter, length, angular misorientation, and the overall polytypic characteristics of a growing NW is resolved. The NW characteristic curves indicate that two stages of NW growth exist. At the first stage, the NW grows axially at an almost constant diameter. The angular orientation of the NW is unstable during this stage. In particular, the NW oscillates within the range of 0.1° tilt angle with respect to the substrate normal and by a periodicity of a few mins. At the second stage of NW growth, the NW grows radially, and the axial growth rate decreases. Moreover, the angular oscillations of the NW stop and the NW continuously tilts towards the surface normal. The overall structure of the NW evolves in favor of WZ by increased NW length. The results indicate that the radial and axial growth compete with each other and the local supply of material change at the NW by increased length. Therefore, in this work, aside from a technical breakthrough, a fundamental understanding of the growth of self-catalyzed GaAs on Si is demonstrated. We hope that this achievement demonstrates the capabilities of the μXRD platform for further studies on nanoparticles of different material systems using in-situ XRD.

Chapter 6

In-situ monitoring of nanowire stability

In this chapter, the stability of individual epitaxial GaAs NWs is studied along several hours of high-temperature MBE processing. The characterization methods are time-resolved in-situ μXRD and SEM. The data in this chapter is published in ref. [79]. In Section 6.1, the NW annealing studies are motivated. The experimental details are discussed in Section 6.2. It is shown in Section 6.3 that when the NWs are exposed to MBE processing conditions at 610±5 °C without the supply of Ga source, they can become thermally and angularly unstable. In particular, the facets of the NWs evaporate, and their diameter decreases. Along with facet evaporation, it is revealed that the PIs evaporate faster than the NWs. Moreover, the NWs tilt and fall down. The in-situ μXRD data evidences vibration/bending of the NWs prior to falling down. Interestingly, when exposed to the original growth conditions, which include gallium and arsenic supply, the vibrations/bendings are suppressed, and the tilting is reversed. The discussion and conclusion of the results are followed in Section 6.4 and 6.5, respectively. The findings in this research contribute in the fundamental understanding of reverse growth through annealing studies. Moreover, this work can provide insights toward the engineering of self-catalyzed GaAs NW growth by NW size tuning as well as the removal of parasitic growth objects which so far could not be reproducibly and fully suppressed in NW growth studies.

6.1 Introduction

Annealing studies can address reverse reaction kinetics and therefore enhance the fundamental understanding of NW formation/evaporation. In-situ TEM annealing studies of nanostructures have revealed an interaction of the catalyst particle with the top

facet of NWs [60, 61]. For GaAs NWs, there are indications of decreasing the defect density by annealing close to the temperature of 600±5 °C [62]. Annealing under UHV conditions at a temperature of 680±5 °C was used right after the growth of GaAs self-catalyzed NWs to reduce the NW diameters for tuning their quantum confinement [167]. In Chapter 5, it was briefly discussed that the high resolution of the μXRD setup ($0.01°\approx 2\cdot 10^{-4}$ rad) makes it a powerful tool for addressing angular orientation of overgrown nano-objects onto single crystalline substrates. Moreover, by extracting the size of the scattering objects, one could address thermal stability of nano-objects using the μXRD. Here, epitaxial self-catalyzed GaAs NWs and PIs are pre-grown on Si(111) and individual nano-objects are monitored at high temperature under MBE processing conditions by means of in-situ time-resolved μXRD. It has been reported that under such conditions, material can evaporate [167] and thermally induced mechanical vibrations of NWs can be excited [168, 169] similar to vibrations excited by electromagnetic waves [170]. In this chapter, the angular stability of pre-grown individual upright standing GaAs NWs is studied at high temperature under different MBE processing conditions namely: i) without supply of source material, ii) with arsenic supply, iii) with arsenic and gallium supply. Moreover, thermal stability of NWs is addressed in comparison to the PIs in GaAs self-catalyzed growth. Given that the PIs are nano-objects of significantly different size and shape compared to the NWs, they may influence the physical properties of a respective NW device. Therefore, removal of the PIs will improve the specific characteristics of a device based on NWs. Given that in growth on both Si native oxide (Section 4.1) and Si patterned substrates (Section 4.2), the growth of PIs could not be fully suppressed, alternative ways to remove the PIs are of interest. This work demonstrates that the ratio between the number of NWs and PIs can be effectively increased by annealing at a temperature below the congruent temperature. Due to the significant size differences, it is expected that the PIs have different evaporation rates upon annealing [171] fundamentally opening up the possibility to remove them. By ex-situ SEM studies, it will be shown that the NWs start to tilt until they lie down flat on the substrate surface by annealing at the temperatures between 460±5 °C and 610±5 °C depending on the NW sizes. That is about 20−170 °C below the congruent temperature of GaAs [120, 121], i.e., the temperature at which stoichiometric evaporation of species takes place. In particular, the NWs that the author grew on FIB patterned substrates with diameters more than 60 nm could fall down within 1 hour of annealing at 610±5 °C. However, the author observed that only at even higher temperatures the wires start to evaporate completely within a reasonable time of experiment. Moreover, the tilting occurs for NWs on patterned as well as non-patterned substrates and with or

without exposure to air. Using in-situ μXRD the tilting process is monitored, and vibration/bending of the NW are identified already before lying down onto the substrate surface.

6.2 Experimental details

Nanowire growth

The NW growth was performed as discussed in Section 4.2 by FIB patterning and using the pMBE chamber [70]. After the FIB procedure, the sample was 1 min HF treated, 10 min boiled in deionized water, 30 min annealed at a pre-chamber at 300 °C at 5×10^{-7} mbar, and in-situ transferred to the UHV pMBE. Here, the sample was further heated to 700±5 °C for 10 min and ramped down to the growth temperature of 610±5 °C, and 45 MLs of Ga were deposited to form Ga droplets which preferentially are located in the FIB patterned holes. Out of these droplets, NW growth was performed by VLS growth [24] at Ga rate of ∼140 nm/h and a V/III ratio of ∼2 for 1 hour. Additionally, several complimentary samples were grown on Si(111) samples of both FIB patterned and native oxide. Some samples are shown in Figure 6.1 where the specified growth conditions can be seen in the caption of the figure.

Scanning electron microscopy characterization

The details of SEM characterization were explained in Section 2.3. The FIB patterning allows for repeated imaging of a specific set of NWs after exposure to various MBE processing conditions discussed below.

Annealing under MBE processing conditions

After the SEM characterization, samples were reloaded back into the pMBE UHV system, to study the effect of exposure to MBE processing conditions. All the samples in this section were initially degassed at 300 °C for 30 mins within $1 - 5 \times 10^{-7}$ mbar range in a pre-chamber and then transferred to the growth chamber and exposed to the respective processing conditions for a defined time. The impact of the process was studied ex-situ by SEM or in-situ by μXRD as described below. In order to study the qualitative impact of air on this study, additional samples on Si(111) with

native oxide were directly processed after growth and cooled down to room temperature. The following conditions were chosen as processing conditions: i) high-temperature treatment without supply of source material, i.e., under UHV conditions with pressure typically below 10^{-8} mbar range; ii) high-temperature treatment in As atmosphere using a flux rate of 300 nm/h at a stabilized background pressure of $\sim 10^{-7}$ mbar; iii) high-temperature treatment with supply of both As and Ga, with an equivalent 2D GaAs growth rate of ~140 nm/h and a V/III ratio of ~2, equivalent to the original growth conditions of the NWs on the FIB patterned substrates.

In-situ micro X-ray diffraction

Time-resolved in-situ measurements by μXRD were performed as a complementary to SEM and in order to obtain a better understanding of the ongoing processes during the annealing in the MBE. The geometry of the μXRD setup is shown in Section 3.1, Figure 3.3. The details of the reciprocal space transformation are explained in Section 3.1. To study the behavior of NWs under MBE processing conditions, a sequence of detector frames is recorded with an exposure time of 1 s. Due to image processing overhead, one image is saved every 1.44 s.

6.3 Results

After the growth, SEM characterization of the FIB patterned sample, grown for in-situ measurement, revealed a growth yield of 21±2% for vertically growing NWs. That was obtained by studying more than 15 patterned subregions (see Figure 6.1a, where one of the subregions is shown). Two specific NWs grown on the FIB patterned substrate are shown in Figure 6.2a,b which are showing a typical length of 3−4 µm with diameter of 60−70 nm and 100−120 nm at the bottom and top, respectively. More SEM images of the as-grown FIB patterned substrates are shown in Figure 6.1a−b. SEM images of the as-grown NWs on the native oxide substrates are shown in Figure 6.1c−d.

In the pMBE chamber, several annealing steps for case i), i.e., without supply of source material, were performed at temperatures of 410±5 °C, 460±5 °C, 510±5 °C, 560±5 °C, and 610±5 °C for one hour and the sample was removed for SEM imaging after every step. For annealing temperatures up to 510±5 °C, no change in the NW morphology has been detected. However, the Ga seed particle on top of the wires seemed to disappear (see Figure 6.3). It is reported that the liquid Ga droplets on Si

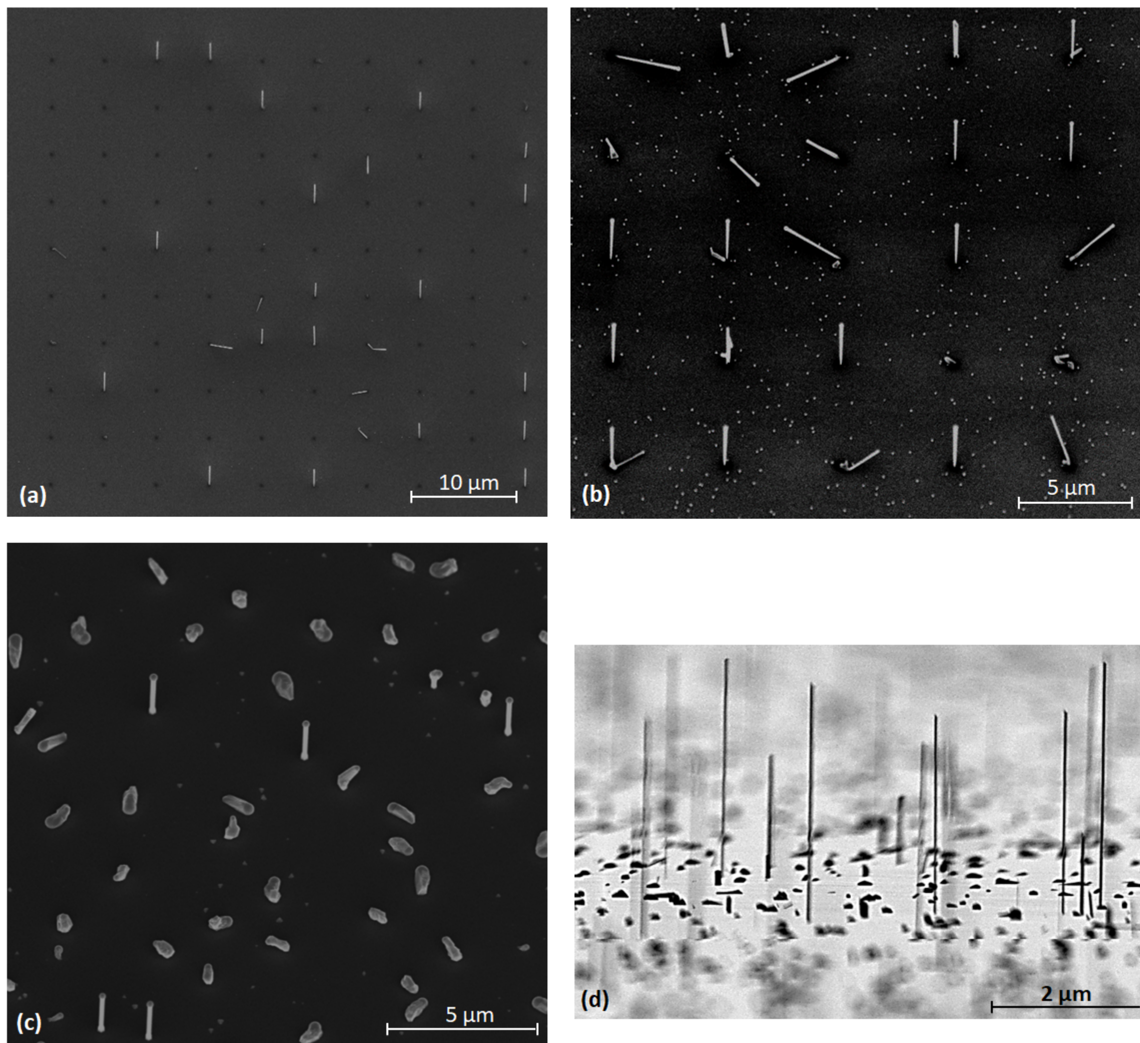

Figure 6.1: SEM image at 30° tilted substrate after GaAs growth on (a) the FIB patterned Si substrate studied during the μXRD in-situ experiment with a NWs with length of 3−4 µm and diameter of 60−70 nm; (b) a different FIB patterned Si substrate grown under similar processing and growth conditions as in (a) but grown at a different substrate temperature of 580±5 °C which resulted in NWs with similar sizes but a higher yield of NW growth as compared to that of (a). (c) Unpatterned native Si substrate; the sample is etched for 1 min in 0.5 % hydrogen fluoride acid diluted in water and boiled in deionized water for 10 min prior to growth and grown at a 2D GaAs growth rate of 30 nm/h and a V/III ratio of 5 at a temperature of 580±5 °C by simultaneous introduction of As and Ga. The NWs have an average diameter and length of 180±53 nm and 2.4±0.2 µm. (d) SEM image at 85° tilted substrate after GaAs growth: the sample was heated to 650±5 °C for 30 min of annealing prior to the growth. After deposition of 65 MLs of Ga to form Ga droplets, NW growth was performed at a growth temperature of 560±5 °C at an equivalent 2D GaAs growth rate of ∼50 nm/h and a V/III ratio of ∼6 for 1 hour.

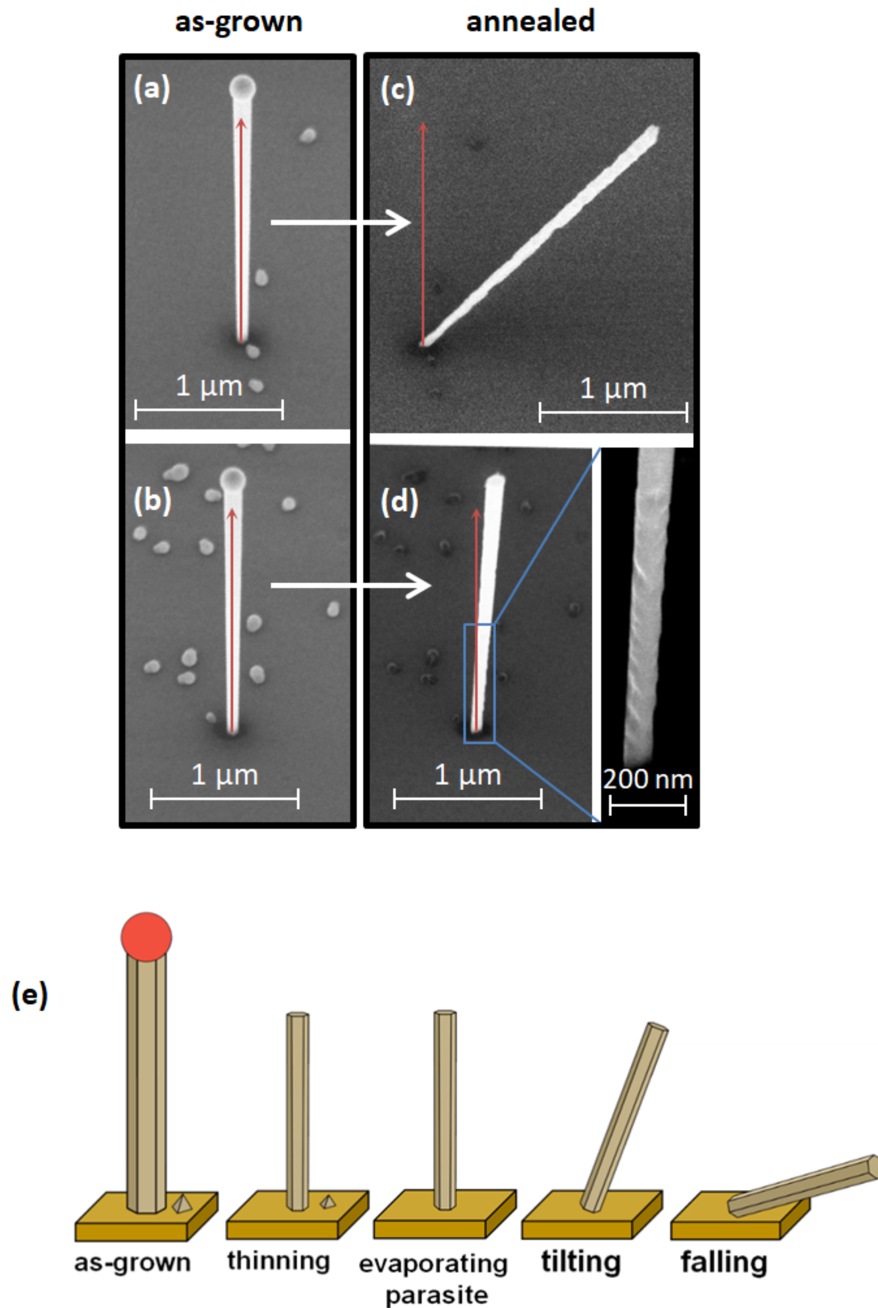

Figure 6.2: Scanning electron micro-graphs of NWs at 30° tilted substrate in their as grown state (a,b), and after exposure to 610±5 °C for 1 hour at UHV conditions (c,d). The comparison of the panels shows that due to the annealing, facets of the NWs are shrinking/degrading and NWs visibly tilt from their initial upright orientation. Additionally, the seed particle and PIs between the wires are disappearing. The diameter of the NW shown in (a) and (c) decreases by annealing from ~89 and ~125 nm to ~63 and ~111 nm at the NW top and bottom, respectively; and the diameter of the NW shown in (b) and (d) decreases by annealing from ~82 and ~138 nm to ~75 and ~120 nm at the NW top and bottom, respectively. (e) Schematic illustration of the summary of results from the several ex-situ SEM studies on patterned and unpatterned NW samples: after the annealing procedure which involved a cooling step down to room temperature, the NWs were thinner and tilted.

substrate decrease in size by annealing [138]. It was observed that during annealing of the samples above 510±5 °C without exposure to air, the Ga droplets on the NW tips indeed decrease size. Considering that Ga forms a self-limiting oxide layer at room temperature [172] and the oxide species of both Ga and As evaporate by annealing at similar temperatures [136], the shrinkage of Ga droplets in our case can be accelerated by evaporation of the oxide layer during annealing resulting in disappearance of Ga droplets (Figure 6.3).

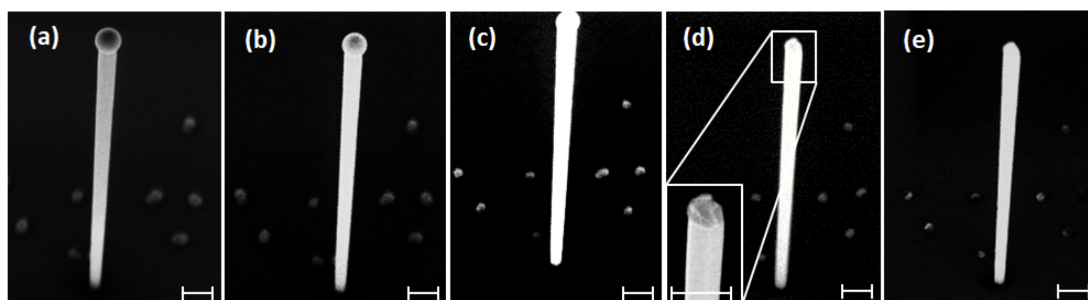

Figure 6.3: 30° tilted SEM image of a NW on sample of Figure 6.1b where panel (a) is after growth; (b) annealed at 410±5 °C; (c) annealed at 460±5 °C; (d) annealed at 510±5 °C; (e) annealed at 560±5 °C. The annealing time at each temperature is for a duration of one hour. The scale bar is 200 nm.

Depending on the NW sizes, the tilting started at different temperatures. On two different NW samples grown on native oxide which had NWs with diameter of 40±8 nm and 25±7 nm, the NWs fall down after annealing at 510±5 °C and 460±5 °C, respectively; however, the NWs maintained their original diameter characterized by SEM. On the FIB patterned samples with NWs above 60 nm diameter, after the annealing at 560±5 °C, few NWs appeared tilted with respect to the substrate normal, again by maintaining their original diameter under the resolution limits of SEM. In contrast, the diameter is decreased after the annealing at 610±5 °C, which can be seen in Figure 6.2c,d. The tilt of initially upright standing NWs drastically changed, cf. Figure 6.2a, b. The schematic illustration in Figure 6.2e pictorially summarizes the ex-situ SEM results. After the annealing, the orientation of the NWs covers an angular range from upright down to even fully fallen, i.e., lying flat on the substrate surface. From the comparison of Figures 6.1 and 6.4/6.5, it can be seen that the tilting behavior is something intrinsic to the NWs treated under such conditions. Especially it is seen in Figures 6.1c and 6.4c−d that NWs grown on native Si oxide, i.e., without patterning, also show similar tilting behavior and lie down on the substrate surface before they evaporate. Moreover, the sample which is not exposed to air after growth also shows fallen NWs after annealing at 610±5 °C, cf. Figure 6.1d, 6.5a of two samples grown under similar

conditions, where in Figure 6.5a the sample is annealed directly after growth. Figure 6.5b shows a sample grown similar to 6.1d but step by step annealed similar to Figure 6.2. On this sample, NWs of different sizes grow and the longer and thinner NWs fall down at lower temperatures. The NWs with 40±8 nm diameter fall down by annealing at a temperature of 510±5 °C. The cross-sectional image in Figure 6.5b in comparison to Figure 6.1d evidences that after annealing the NWs can lie completely flat on the substrate.

By means of ex-situ SEM studies, it is established that epitaxially upright standing NWs exposed to high temperature lie down on the substrate surface without supply of source material (case i) before they evaporate. Accordingly, to reveal the involved mechanisms, in-situ μXRD is performed for cases i−iii mentioned above. It is worth noting that the ex-situ SEM annealing study at each sample included a heating as well as a cooling step up to the annealing temperature and down to the room temperature before SEM characterization; and only an in-situ time-resolved monitoring study could reveal if the NW falling happens during the heat-up/cool-down or during the annealing. Using the pMBE chamber, time-resolved in-situ diffraction studies have been performed at beamline P09/DESY, Hamburg in the vicinity of the GaAs(111) Bragg peak. Similar to Chapter 5, the GaAs(111) Bragg condition is fulfilled at 7.27° incidence angle at 15 keV X-ray beam energy with respect to the surface, and the resulting beam footprint on the surface is 1.8×50 µm². Here, up to 10 holes were illuminated simultaneously (one row of holes in Figure 6.1a). By keeping the Bragg condition, the sample was mapped to locate the FIB patterned area containing the NWs of interest (similar to Figure 5.2 in Chapter 5). For the selected region of interest, a representative detector frame transformed into the reciprocal space coordinates was shown in Chapter 3, Figure 3.3b where the features in the detector frames at the μXRD setup were introduced. From the intensity ratio of ZB and WZ Bragg signals, one concludes that under the used growth conditions, the NWs are predominantly grown in the ZB phase in this chapter of my work. Once the NW region of interest was identified, the temperature was ramped up to 610±5 °C with a rate of 20 °C/min. Because the ex-situ SEM images indicated tilting of NWs at 610±5 °C, the author chose this temperature (which is 20 °C below the congruent temperature of GaAs [120]). At the same time, it is expected that all the oxide species of Ga and As evaporate which had been created during exposure of the sample to air [136]. First, the behavior of the NWs under As supply (case ii) is studied. In Figure 6.6a−c, evolution of the signal on the detector is shown for selected detector frames, while the full time evolution of the signal is shown in a supplementary video file in ref. [79] (Video 1). Note that during the initial 50 min

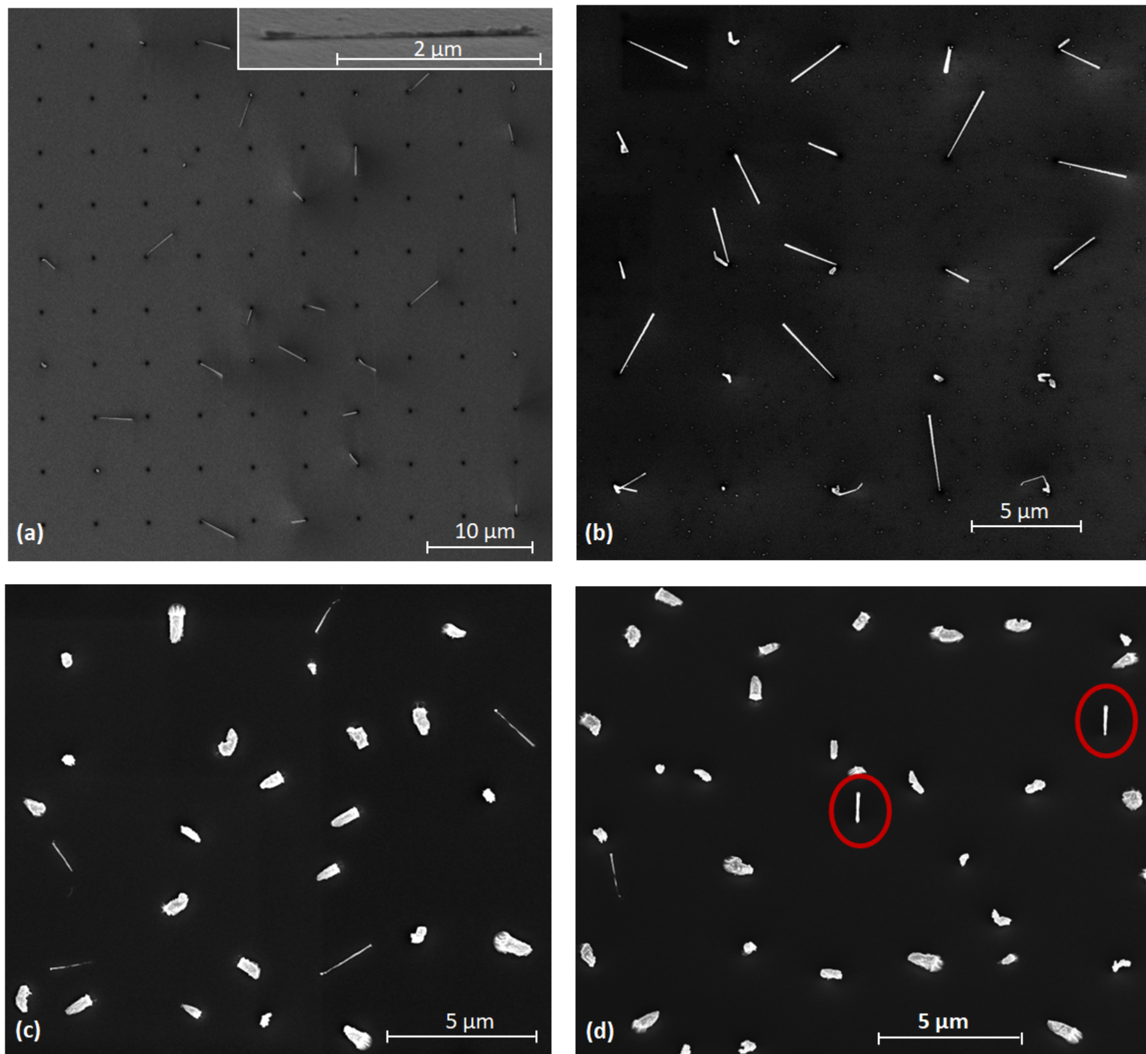

Figure 6.4: (a) and (b) are 0˚ degree tilted (top-view) SEM images after the annealing of the same sample region shown in Figure 6.1(a) and (b). Panel (a) shows the sample after the in-situ μXRD experiment where the inset shown at the top is a SEM image at 85˚ tilted substrate showing a NW (at one other growth region) horizontally lying on the substrate after annealing; and (b) shows the sample after annealing at 610±5 ˚C for 1 hour. Panel (c) is a 0˚ degree tilted and (d) is 30˚ tilted SEM image which show two regions of the sample in Figure 6.1(c) after annealing at 610±5 ˚C for 1 hour and an additional 10 min at 660±5 ˚C. The majority of the NWs fell down after annealing while (d) shows two thicker NWs marked by red circles which are still upright standing after annealing. The fallen NWs have an average diameter of 67±26 nm and the upright NWs have an average diameter of 99±36 nm. The overall average diameter and length are 84±30 nm 1.7±0.3 µm.

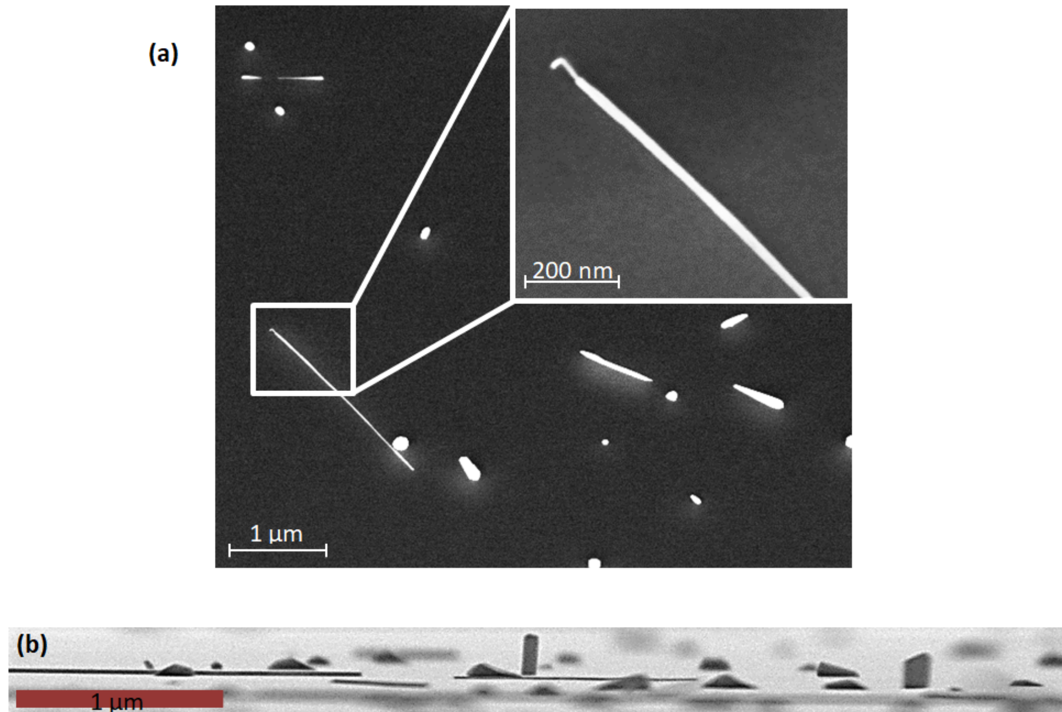

Figure 6.5: Two samples grown in identical procedure as in Figure 6.1(d) and annealed without any source supply: (a) 30° tilted SEM image of a sample which is annealed without exposure to air at 610±5 °C for 1 hour: the majority of the NWs fall down after annealing. The inset shows a high magnification focus on the NW base after falling. (b) Cross-sectional SEM image at 89° tilted substrate: after growth and SEM characterization, the sample was degassed at 300°C for 1 hour, reloaded back into the MBE chamber and annealed at 510°C for 1 hour. The longer NWs fall down, whereas the shorter and thicker ones seem to be more stable.

at the target temperature, beam-realignment and stabilization had to be performed repeatedly, which prohibited monitoring of the diffraction signal. Moreover, to assure the angular stability of the beam with respect to the sample, the specular beam position and intensity was monitored which demonstrates sufficient stability of the system (e.g., see Video 1 in ref. [79] at the specular beam). In the region of interest, initially, two NWs were in Bragg condition (see Figure 6.6a). In the time interval between 50 and 53 mins, the signal of both NWs slightly changes along the DS ring and also weakens in intensity.

The intensity variation of the signal either corresponds to the evaporation of NW material, or reflects a tilt perpendicular to the detector plane which causes deviation from exact Bragg condition and subsequent loss in intensity. Because the tilting of the NWs is observed at the detector plane within 1°, it seems likely that similar tilting also occurs in other directions. Based on the discussion in Chapter 5 in Figure 5.12, a range

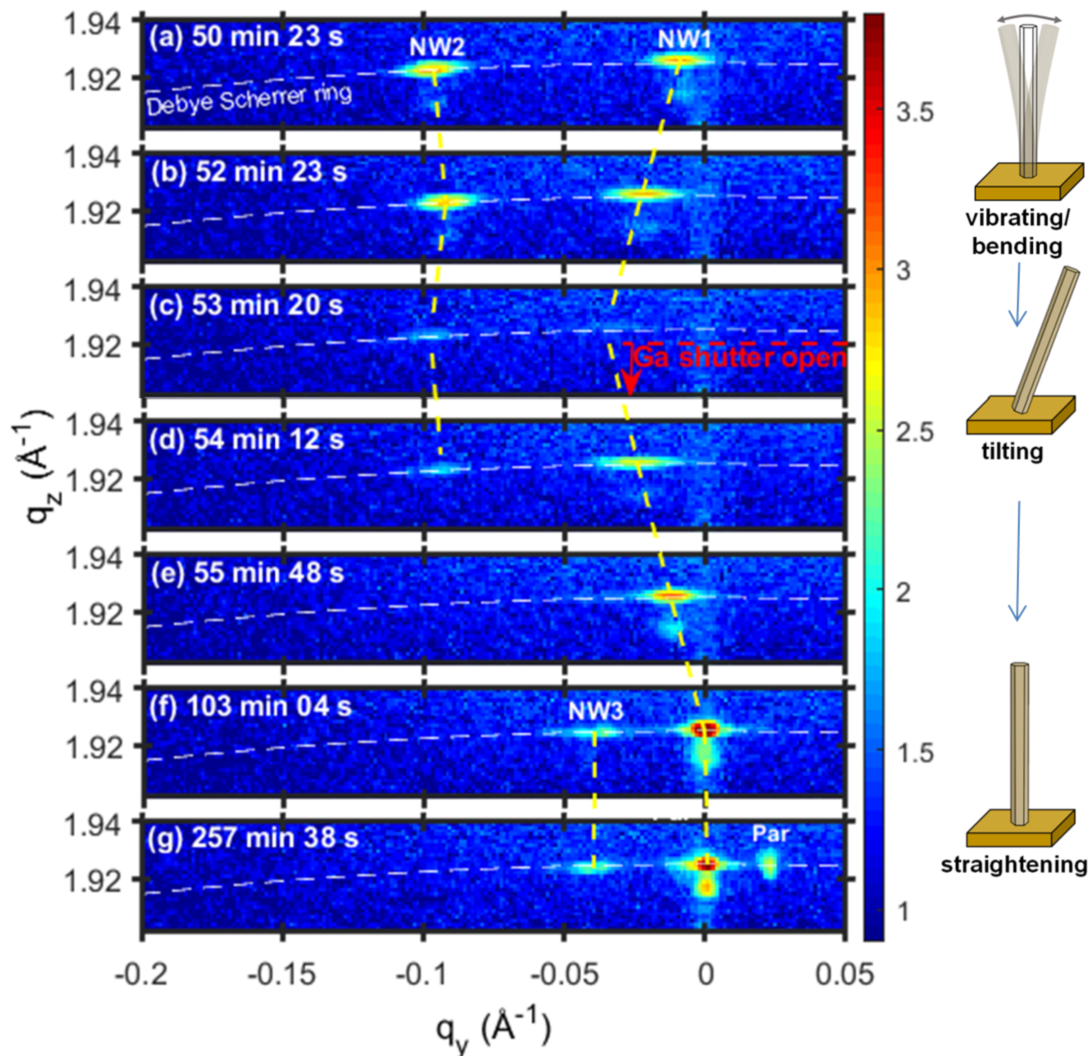

Figure 6.6: Evolution of the intensity distribution of the NWs in selected detector frames during exposure to As and simultaneous Ga and As flux at a substrate temperature of 610±5 °C: (a–c) annealing under an As flux equivalent to a ∼300 nm/h growth rate of 2D As-limited GaAs; (c–g) simultaneous introduction of As and Ga at a V/III ratio of 2. During the measurement, several objects are in the Bragg condition; however, during the several hours of the experiment, realignment was performed to remain aligned to the signal labeled as NW1. A logarithmic color scale is used as indicated on the right, which means that in part g the signal of NW1 is more than 1 order of magnitude stronger than the signal of a PI, labeled by "Par". One observes that, during the annealing in As, the tilt of NW1 is increasing, while this effect is reversed in parts c–g. The panel at the right side illustratively demonstrates the changes happening on NW1 in real space.

of NW tilting within 1° (> 0.03 Å^{-1}) along q_x is sufficient to fully loose the NW signal preventing the quantitative analysis of the diffracted intensity. In full agreement with the analogy of discussion in Chapter 5, the observation of NW integrated intensity in this chapter showed an oscillating intensity variation down to > 90 % collapse along the several hours of the experiment.

By observing the NW tilting during the annealing under As supply (case ii), it is concluded that the NW behavior is similar to that without supply of source material observed in Figure 6.2 (case i). Before NWs were fallen, the processing conditions are changed to further monitor the behavior under the supply of both Ga and As (case iii). To do this, at the timestamp of 54 min, the Ga source, in addition to the As source, was opened. It is seen in Figure 6.6d−g and the corresponding Video 1 in ref. [79] that the tilt position and intensity of NW1 were recovered; and at the end of this growth process, the intensity was even stronger compared to that at the beginning of the experiment, indicating growth of the GaAs NW.

At the same time, the β angle is reduced and approaching zero at the final stage of the growth run. The panel at the right side in Figure 6.6 pictorially illustrates the changes in NW1 in real space. The signal of NW2 is lost during the process, but a few frames just before the signal vanishes, the tilt β of NW2 is reduced after opening the Ga shutter (see NW2 in Video 1 in ref. [79] at the timestamp of 54.5 min to 55 min). The loss of the signal of NW2 can either be due to a slight drift in the position of the X-ray beam (since the alignments scans only targeted NW1) or simply due to a tilt along q_x. During the last phase of the growth, newly appearing signals are associated to a NW and PI which in Figure 6.6 are named “NW3” and “Par”, respectively. Signals of NWs and PIs, similar to Chapter 5, can be distinguished because the PIs have much smaller height compared to NWs and show an extended signal along q_z [157]. Moreover, different NWs can be distinguished and monitored from the different ratio between their ZB and WZ content. It was observed that the growth rate of PIs is slower than that of NWs. However, the observations here evidence the appearance of the signal, assigned to a PI, about 150 min after opening the Ga shutter (see video 1 in ref. [79]). This could be related to the suppressed nucleation of the PI after oxidation of the sample at the first growth run, which is in agreement with the findings in ref. [173].

During the processing with supply of both Ga and As, also the difference between the two peaks along q_z was observed to evolve. The NW remains mainly in the ZB phase; however, the peak associated with pure WZ moved toward the ZB peak indicating a change of the polytype mixture during the additional growth similar to ref. [96].

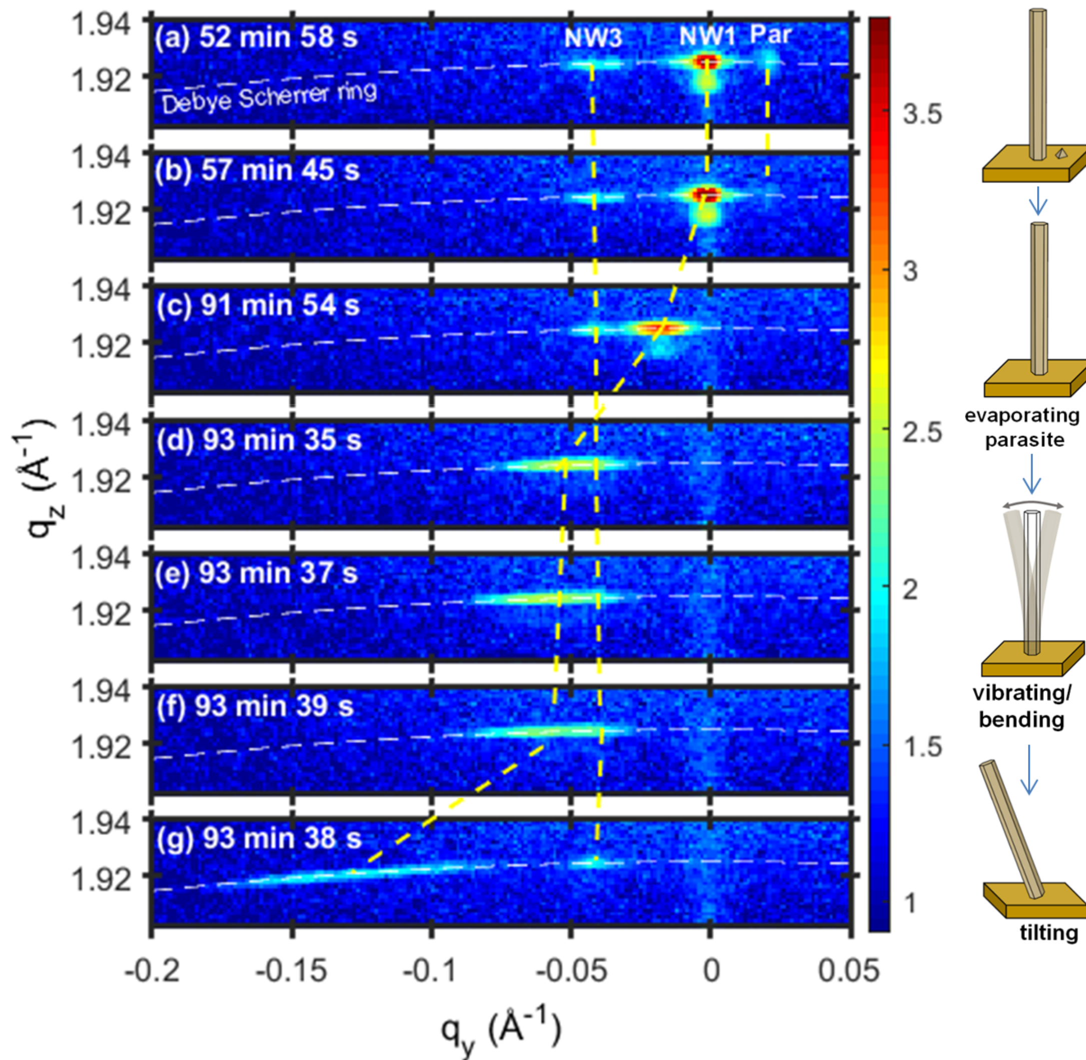

Figure 6.7: Evolution of the intensity distribution of the NW in selected detector frames during annealing without source supply at 610±5 °C. Panel a shows the NW fully upright, similar to the end of the regrowth process shown in Figure 6.6g. While the annealing is ongoing, the parasite ("Par") evaporates (b) and the NW tilts until it vanishes from the detector plane (c–g). Panels d–g show four consecutive frames. A logarithmic color scale is used as indicated on the right. The panel at the right side illustratively demonstrates NW1 in real space.

After 220 min, the supply of Ga and As molecular beams was stopped and the NWs were further monitored by μXRD without source supply (case i). Roughly 10 and 25 min after ending the supply of material, the pressure decreased below 5×10^{-8} and 10^{-9} mbar, respectively. In Figure 6.7, the evolution of the diffraction signal is shown for selected detector frames during annealing without source supply (case i). During the initial 53 min, the NW1 signal remains very similar to that observed in Figure 6.6g, but in agreement with the findings observed in Figure 6.2, the PI signal becomes weaker and vanishes much faster than the NWs at the timestamp 58 min. This indicates that the PI is thermally not stable. In the time interval between 57 and 91 min, the NW signal slightly broadens and moves along the DS ring, indicating a change of β by 0.26° (see Figure 6.7a–c). After 91 min of UHV annealing, changes in β are accelerating. As seen in Figure 6.7c–f, the signal from NW1 gets significantly broadened along the DS ring and also begins to tilt more. In the detector frame acquired after Figure 6.7g, the signal from NW1 completely vanished, and it could not be found again even by sample rocking scans and X/Y mapping. Finally, after a further 44 min, the heating was stopped. The pictorial illustration at the right side of Figure 6.7 shows a summary of the changes in NW1 along the annealing process. The full time evolution of the signal can be seen in ref. [79] at the supplementary information, Video 2.

6.4 Discussion

As is shown above, high-temperature treatment of GaAs NWs in a high vacuum can result in tilting of the NWs. Up to 510±5 °C, the NWs with diameters of more than 60 nm grown on FIB-patterned Si substrates are stable, and no significant change is observed after 1 h of treatment. At 560±5 and 610±5 °C, tilting of the NWs, as well as relatively slow evaporation, takes place. However, a side-wall roughening visible in SEM occurs only at annealing temperatures as high as 610±5 °C. This is attributed to material evaporation from the facets, shrinking the sizes of the NWs, which is in agreement with the annealing effects at a temperature of 680 °C, as reported in ref [60]. It is reported that, by annealing of GaAs, pits may form at the surface irregularities (kinks) [174]. In the annealing experiment presented in this chapter, the surface irregularities could be enhanced as a result of oxidation and consecutive oxide removal, which leave atomistic kinks on the NW surface. Moreover, the PIs fully evaporate during annealing at 610±5 °C (cf. Figure 6.2a,b). The latter might be related to the Gibbs–Thomson effects, explaining the greater detachment rates of adatoms from smaller object sizes

[171]. Similar to the shrinkage of Ga droplets after exposure to air explained above, evaporation of oxide species on the PIs could accelerate the shrinkage rate [173].

The ex-situ studies also reveal that the PIs, which inevitably grow during self-catalyzed growth of GaAs NWs, disappear when the samples are treated at 610±5 °C for 1 hour. It is notable that the tilting of the NWs occurs on the onset of evaporation for NWs thicker than 60 nm; however, as is shown for growth on pre-patterned as well as non-patterned (native Si oxide) Si substrates, NWs get thinner first, tilt, and finally lie down on the substrate surface before they fully evaporate (see Figure 6.2 and 6.8). Although a critical thickness might exist under which the NW tilt and fall down, the author could not report such a critical thickness for 610 °C. That is because the diameter shrinkage seems to be inhomogeneous along the NWs where the NWs possess a much smaller diameter close to their bases (see Figure 6.8b and c).

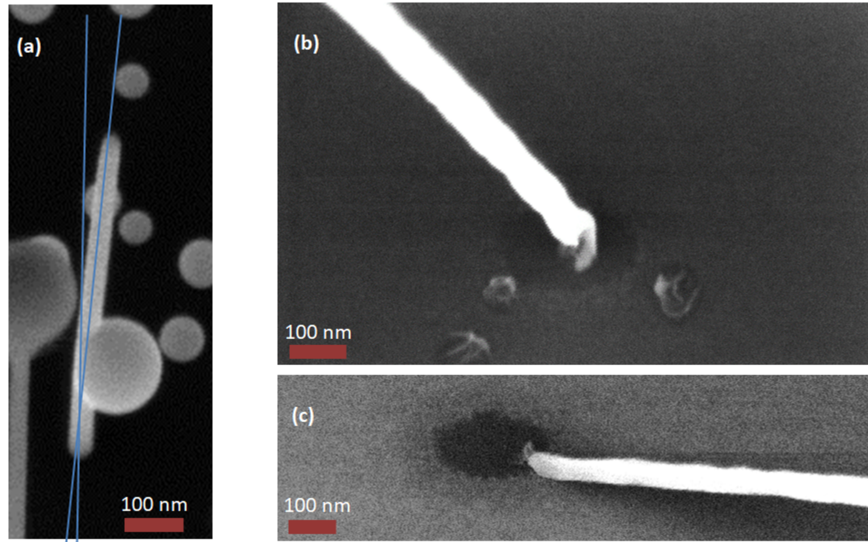

Figure 6.8: SEM image at 30° tilted substrate: (a) Ga droplet at the NW side-wall result in NW bending. (b) and (c) NW tilt after annealing of the sample shown in Figure 6.2.

On the other hand, it is observed that the initially grown thinner NWs are angularly unstable at even lower temperatures. In particular, the NWs in the samples with average NW diameter of 40±8 nm and 25±7 nm tilt at annealing temperatures of 510±5 °C and 460±5 °C, respectively. Variations in the onset of tilting from NW to NW on each sample can be explained by the local differences in the object sizes and surroundings, which imply deviations of the local evaporation kinetics. Also, the nucleation within the FIB-patterned holes might vary from NW to NW [94] influencing the tilting behavior and direction as well. The NWs seem to be still straight in the SEM images even after they fully lie down to the substrate surface (see Figures 6.4 and 6.9f). At even

higher temperatures above 660±5 °C, the NWs completely evaporate within 1 hour of annealing. From the comparison of the NW length and diameter in Figures 6.1c and 6.4c,d, one sees that the average length of the NWs decreases by about 30%, whereas the diameter decreases by 54%, which corresponds to evaporation of about 80% of the volume of the NW. This indicates that the evaporation mainly takes place from the NW side planes. Tuning of the diameter of self-catalyzed GaAs NWs by a comparably small change of the length was formerly reported by annealing at a temperature of 680 °C at a UHV pressure of 10^{-8} mbar [60]. The density of the NW growth in ref. [60] has been 25 times higher than that of our FIB patterned holes (10^8 cm^{-2} vs. $4{\times}10^6$ cm^{-2}), the diameter of the NWs was considerably smaller, and the annealing time was limited to 30 min. Considering these differences to our experimental parameters, the evaporation/tilting of the NWs are expected to be different. Moreover, no high-resolution XRD was performed by the authors; therefore, a small tilt might have been left unnoticed with SEM characterization. In order to understand the detailed mechanism of this tilting process, the author analyzes the evolution of the peak width, i.e., fwhm on the DS ring, and the tilt angle β monitored during the in-situ experiments (Figure 6.9). Gaps in the extracted data originate from interruptions of the data acquisition due to realignment of the NW position and Bragg angle. In the results of this realignment/tracking process, the peak intensity may slightly change and is therefore not analyzed. Figures 6.9a and b show the tilt β and parts d and e of Figure 6.9 show the peak width along the DS ring of NW1 during processing with only As and with both Ga and As supply (a,d), and without supply of any source material (d,e). The dashed lines in Figure 6.9a, c indicate the moment when the Ga shutter was opened. The NW starts to tilt during annealing after 50 min if only As is supplied (Figure 6.9a) and after 89 min without supply of source material (Figure 6.9b). In particular, in Figure 6.9b, between 53 and 88 min, β changes by a small amount ($\Delta\beta < 0.1°$) but increases drastically during the following 6 min and reaches tilt angles as large as 3.5°. From the change of β with time, the tilt rate can be derived, i.e., the velocity with which the NWs are lying down to the substrate surface. The derived data are shown in Figure 6.9c and show that up to the timestamp 88 min, the NW is tilting back and forth with velocities below 0.025 °/s. After the onset of the tilting, the velocity is sharply increasing at the last frame (Figure 6.7g) and reaches 1.6 °/s which is significantly beyond the y-axis limits in Figure 6.9c and not shown. This occurs just before the signal disappears from the detector, and the ex-situ SEM images in Figure 6.9f show that the NW has likely laid down on the substrate surface. In the inset of Figure 6.4a, a cross-sectional SEM image at 85° tilted substrate is shown at another growth region on this sample where a NW

is horizontally lying on the substrate. Although Figure 6.9a,b corresponds to the case with and without supply of As, one attributes differences in the onset of the tilting to the different properties of the NWs before the procedure was started. Our conclusion is based on the SEM study of the native oxide sample, where NWs with different diameters coexist. The key importance of the diameter is deduced from the fact that after the annealing NWs with a larger diameter are still standing upright whereas thin NWs are mostly fallen down. As shown in Figure 6.4c,d, the observed average diameter of the wires which are still standing after annealing is 99 ± 36 nm whereas the fallen wires have an average diameter of only 67 ± 26 nm though again with a significantly smaller diameter at a certain point near the NW base. In this sample, one can distinguish the fallen NWs from those which were initially grown tilted according to the following facts: (i) NWs and crystallites can be clearly distinguished by their shapes and sizes; (ii) by comparing the length of the fallen NWs after annealing to those NWs formerly vertically standing, it is concluded that the upright NWs fell down by annealing; (iii) the orientations of the fallen NWs after the annealing do not follow any crystallographic orientation, whereas the crystallites, which were present before the annealing, seem to have particularly preferred orientations, as determined from the low magnification SEM micro-graphs. The latter is applicable also in our other annealing experiments.

In Figure 6.9a, it is also shown that the supply of both Ga and As can reverse the tilting behavior. While the tilt of the NW increases above 1.5° before the Ga shutter was opened, it decreases immediately once the gallium shutter was opened and remains around 0° for the full duration that Ga and As were supplied. Note that the reversal of the tilt was shown for a NW which did not yet fully lie down on the substrate surface and likely only occurs upon such an intermediate tilt position.

From the evolution of the tilt angle, the tilt process itself is established. Additional insight can be gained from analyzing the fwhm of the signal along the DS ring. Generally, this fwhm has various contributions:

1) Because it is inversely proportional to the diameter of the crystalline structure, its changes indicate shrinking of the NW in the respective direction. For the inversely tapered NWs, as shown in Figure 6.2, it is the volume average diameter as defined in equation 5.5.

2) Any variation of lattice plane tilt within the structure affects the peak position of the respective parts and therefore causes a broadening. This is an important factor in bent NWs, often occurring during core-shell growth [175, 176].

3) Additionally, any change of the peak position during the data acquisition time also translates into an additional peak broadening.

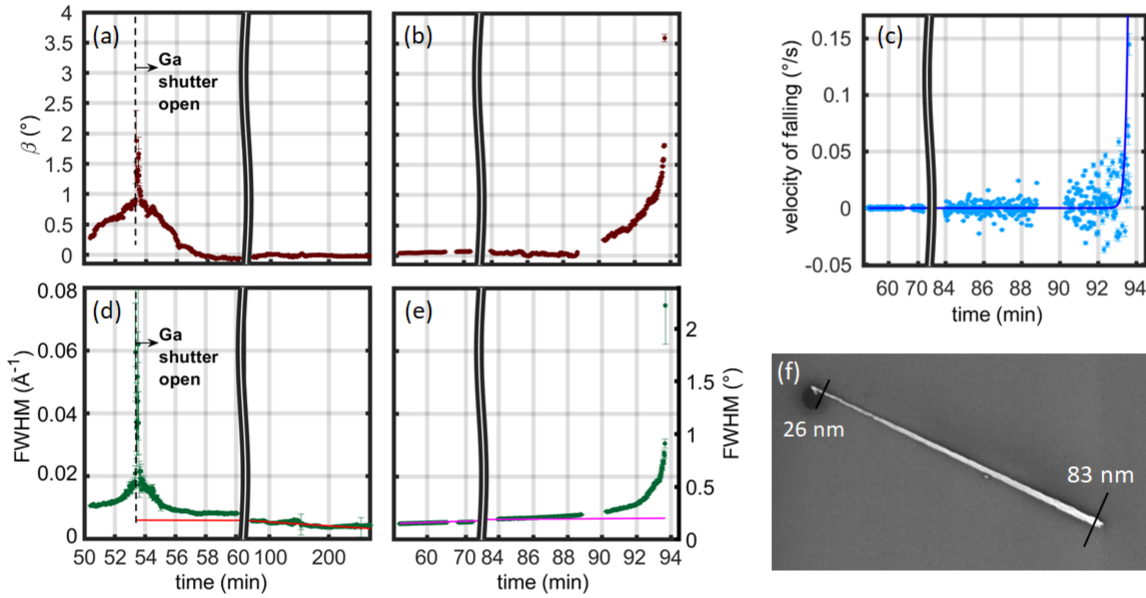

Figure 6.9: Time-resolved characteristics of NW1 extracted from the detector images shown in Figures 6.6 and 6.7. Panels a and b show the lattice tilt β during the annealing with and without source supply, respectively. A vertical line in part a indicates the moment when the Ga shutter was opened in addition to the constant supply of As. Panel c shows the velocity of falling of the NW deduced from the evolution of the lattice tilt in panel b. Data points show the actual falling velocity, while the solid line is a guide to the eye. Panels d and e show the fwhm of the diffraction signal along the DS ring for the equivalent processes shown in parts a and b. Gaps in the data correspond to moments when realignments were performed. The axes are broken to highlight the areas were the interesting variations occur. The red line in part d shows a linear fit for the time interval larger than 65 min, and the purple line in part e connects the fwhm values at time = 0 and the values extracted from SEM results corresponding to the end of the experiment as a guide to the eye, suggesting our best guess for contribution #1 discussed in the text. (f) 0° tilted SEM image of the NW after in-situ experiment: the NW is horizontally lying on the substrate.

A priori it is not clear which of these effects is dominating, but because the NW sizes are known from ex-situ SEM investigations (Figure 6.1a and Figure 6.9f/6.4a), one can estimate the volume average diameter and obtain contribution #1 to the fwhm as 0.11±0.02° (143±26 nm) and 0.25±0.02° (63±5 nm) at the beginning and end of the experiment, respectively. During the final phase of Ga and As supply, the observed fwhm is trending downwards, indicating that the NW diameter grows. Additionally, a small increase of the NW length is determined by SEM after the experiment, indicating that, in addition to the diameter growth, also length growth occurred. Although the seed particle evaporated during annealing above a temperature of 510±5 °C (see Figure 6.3), it could either have been reformed during the simultaneous supply of gallium and arsenic or the NW could be growing via a vapor-solid mechanism [29]. The red line in Figure 6.9d indicates the continuous increase of the diameter and concomitant decrease

of the fwhm. As discussed above, during the annealing without source supply, the NW material is continuously evaporating from the side facets, causing the NW to shrink and accordingly increasing the fwhm, as indicated by the purple line in Figure 6.9e. The purple line connects the fwhm of values at time=0 min and time≈138 min. Here, at time=0 min, the fwhm is assigned to that by the end of the experiment in Figure 6.9d, and at time≈138 min, that is assigned to the volume average diameter extracted from Figure 6.9f. So, in summary, one can state that the red and purple lines in parts d and e of Figure 6.9, respectively, represent the best guess for contribution #1 and its variation with time. Accordingly, the average diameter growth during roughly 210 min of growth is estimated to be about 67 nm, while during the full 138 min (94 min as shown in Figure 6.7 and an additional 44 min) of annealing without source supply, it decreases from about 170 nm to 63 nm.

As can be seen in Figure 6.9d,e, contribution #1 explains the observations during the end of Ga and As supply, as well as at the beginning of the annealing without source supply. However, during the time when the NW is rapidly tilting (Figure 6.9a,b), the corresponding fwhm is significantly larger ($0.25° < \text{fwhm} < y2.25°$) than the estimation from only the NW thickness, indicating that also other effects contribute. The additional broadening of the diffraction signal could be explained by bending of the NW according to contribution #2. Although NWs are always found to be straight by SEM inspection, even after the lie down to the substrate surface, the required amount of bending could be undetectable by the resolution of the SEM. However, note that a homogeneous bending along the NW or a bending limited to a small segment of the NW would lead to distinct peak shapes, which one does not observe. Experimentally, a symmetric Bragg peak with nearly Gaussian shape is observed. In order to obtain such a peak shape from bending, an inhomogeneous bending radius would be needed along the NW. Therefore, only a very special type of bending could explain our observations. On the other hand, it is obvious that the velocity of falling shown in Figure 6.9c causes an additional broadening according to the contribution #3, which is also insufficient to explain the observed broadening. Given the maximal peak broadening from the NW diameter and velocity of falling, one would expect a fwhm below 0.33° considering the integration time of one detector frame. However, after the timestamp 93 min in Figure 6.9e, the observed fwhm is larger than 0.5°. The remaining extra broadening, if not caused by the sophisticated bending scenario mentioned above, could be also attributed to the effect of thermally excited vibrations. From basic elasticity considerations, it follows that the thermal energy during annealing is by a factor of 10^6 larger than the energy needed to excite the eigenfrequencies. In other words, the eigenfrequency of

such vibrations is in the megahertz range for the GaAs NWs with the typical sizes of the NWs in this chapter [170] and would be far beyond the ability of the XRD setup time resolution. However, such vibrations may cause an additional broadening of the diffraction signal as a result of contribution #3. Because the presented experiments cannot unambiguously distinguish the effect of static bending or dynamic vibrations, one could propose to disentangle these phenomena by future optical interferometric investigations [177]. Looking back to Figure 6.9d, the increase of the peak width during treatment with As supply can also be interpreted in the same way because the huge increase of the peak width cannot be explained by a variation of the diameter or falling speed alone but only by the presence of vibrations/bendings. The vibrations/bendings are suppressed once the Ga and As shutters are opened.

Therefore, the following processes are likely responsible for the scenario of the straight NWs lying down to the substrate. Generally, during the annealing, material slowly evaporates. Whereas As evaporates into the gas phase, a significant part of Gallium atoms diffuse along the NW side plane, rebind into the surface and diffuse again mainly toward the substrate. Because no gallium droplets were observed after the annealing procedure in agreement with observations in ref. [138], one could assume that individual gallium atoms diffuse from the NW toward the substrate. It is speculated that the kink at the connection of the NW with the substrate presents a particular pinning center for the Ga atoms, and therefore, accumulation might take place at this position. Because of Ga-assisted etching, an increased removal of material could happen in proximity to the holes [178]. Considering the small contact plane between NW bottom and the pre-patterned hole [94] as well as that on the native Si oxide [17], it is very likely that the material at the contact plane will be consumed fast and finally initiates the falling of the remaining NW. In agreement with this explanation, images after the annealing (Figures 6.2c and 6.9f) show that the NW is the thinnest at the bottom part. In order to test the hypothesis of Ga accumulation at the NW base, the author performed an additional experiment, where after the NW growth, Ga deposition was performed without supply of As (see Figure 6.10). Ga deposition resulted in significant formation of Ga droplets (Figure 6.10a compared to Figure 6.10b−g). The results indicate that the Ga droplets can accumulate at the NW side-walls or at the NW bases (see Figure 6.10d−g), which lead to a visible bending of the NWs in some cases characterized by SEM, as shown in Figure 6.8a. The strong surface tension of the Ga droplets can be an explanation for the NW bending. By the annealing procedure presented in Figure 6.2, which is without Ga deposition, the NW base does not contain a detectable Ga droplet by SEM inspection (see Figure 6.8b−d). It is also noted that

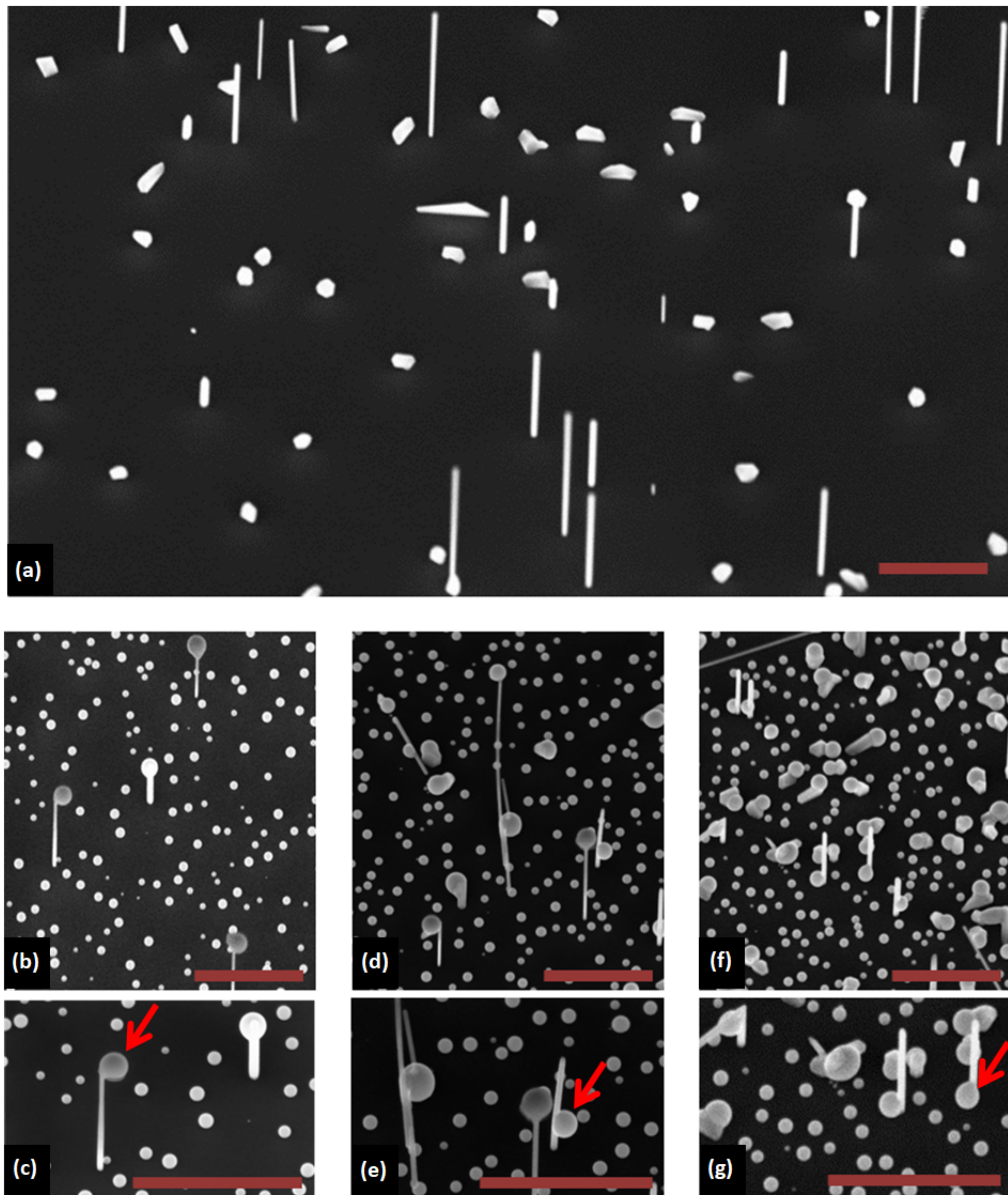

Figure 6.10: SEM images at 30° tilted substrate (a) unpatterned native Si substrate; 45 ML of Ga was deposited initially at a substrate temperature of 590±5 °C. The NW growth was performed by simultaneous introduction of As and Ga at 2D GaAs growth rate of 40 nm/h and a V/III ratio of 5 at a substrate temperature of 560±5 °C. (b−g) the sample was grown like in (a), but after stabilizing the background pressure at $1-2\times10^{-8}$ mbar by a waiting time of 30 min at the growth temperature without material supply, 16 min of Ga deposition at 40 nm/h and 13 min of Ga deposition at 150 nm/h was performed. (b&c), (d&e), (f&g) are different locations at the sample shown in low and higher magnifications. The Ga droplet is accumulated at different locations with respect to the NWs. The scale bar is 1 µm in all panels.

the type of bending shown in Figure 6.8a is unlikely to result in a symmetric broadened Bragg peak.

Although calculations show that the bottom part of a NW is hotter compared to the main NW body, this has been shown to be a minor effect according to ref. [179]. Therefore, one could rule out that a variation in temperature along the NW explains the observation.

During the final part of the falling, at which the NW was suggested to vibrate/bend, it is, in particular, this thinnest point where the biggest strain is induced by the vibrations. From elasticity theory, it follows, in analogy to the vibrations of a cantilever beam, that the highest strain occurs close to the clamping point [180] corresponding to the NW/substrate interface. Because the strain is changing the local bond length, which influences the bonding energies, it would also enhance the local evaporation rate. Note that both tensile and compressive strain occurring during the oscillation of the NW cause such an enhancement because the atomic distances deviate from their equilibrium. The possible vibrations therefore might enhance the speed of the tilting during the final stage of the falling process. For the thinner NWs, the sufficient Ga etching is faster due to their size and, on the other hand, the energy needed to vibrate/bend them is lower; therefore, the strain enhanced evaporation could be activated at lower thermal energies. Thus, the combination of the described processes results in the NWs lying down on the substrate surface.

6.5 Conclusion

In this chapter, the stability of epitaxial GaAs NWs under MBE processing conditions is studied, with and without supply of source material. In particular, it is found that by annealing below a temperature of 510±5 °C (1 hour) without supply of source material, no change of the NW morphology can be detected; however, the Ga-rich seed particles decrease size or vanish. Exposure of the samples to air facilitates evaporation of the seed particles further. The ex-situ SEM studies showed that when the annealing temperature is increased to 660±5 °C, the NWs up to about 100 nm diameter fully evaporate within 1 hour. Interestingly at the intermediate temperature of 610±5 °C, where the evaporation rate is slower, by both ex-situ SEM investigations as well as in-situ studies using μXRD, it is shown that the NWs lie down to the substrate surface before they fully evaporate. That is evident for NWs grown on either pre-patterned substrates, or for random nucleation and also observed with and without exposure of

the NWs to air showing that this behavior is intrinsic to various types of GaAs NWs.

It is found that during annealing, the evaporation of PIs is much faster than that of NWs opening up the possibility of their removal by an aftergrowth step which could be used in future for the engineering of self-catalyzed NW growth.

The in-situ μXRD studies, furthermore, reveal that, before the wires lie down on the substrate surface, they vibrate/bend. That is attributed to either NW bending or thermally excited vibrations that increase upon decreasing thickness caused by the evaporating material. Because the As partial pressure influences the congruent temperature [121], it is also expected to change the evaporation rate. However, by our in-situ study, we also showed that the phenomenology of the falling behavior, including the vibration-induced tilt, is similar without supply of a source material and with As background pressure. In contrast to that, the tilting process can be reversed, and vibrations/bendings suppressed when the NWs are exposed to growth conditions, i.e., Ga and As molecular beams. This chapter shows the limits of the stability of GaAs NWs upon annealing close to the growth temperature. Even before evaporation occurs, the NWs lose their epitaxial relationship to the substrate and lie down on the substrate surface. To maintain epitaxial up-right NWs, in addition to the evaporation kinetics, one also has to consider the mechanical stability.

In disentangling the effect of tilting and vibrations/bending, we benefit from the high angular and sufficient temporal resolution of the μXRD setup, which is able to resolve also minor tilts below 0.01° and, in our case, was used with around 1 s temporal resolution. The time resolution can, however, be increased to the millisecond regime when the highest frame rate of the detector is used [181]. Although similar frame rates can be achieved with many techniques, the angular resolution is clearly beyond other commonly used techniques like TEM and electron backscatter diffraction [182]. With reference to this work, in the future, the use of in-situ XRD might enable understanding dynamical phenomena of other material systems, e.g., refs. [176, 183, 184].

Chapter 7

Conclusions and outlooks

> "*The next-generation optoelectronics devices will consist of semiconductors, organic molecules, metal complexes, and biological molecules that are regularly positioned in nanospace.*" M.H. Crawford, in Semiconductors and Semimetals, 2017

Summary and conclusions

In the last two decades, tremendous advancements have been achieved toward the application of NWs in our daily lives. These advancements are in both fundamental understandings and engineering aspects. In this work, the author focuses on the synthesis and characterization of GaAs self-catalyzed NWs on Si(111). These nanostructures are the future building blocks of our (opto)electronic devices. In particular, we aim for contributing in both engineering and fundamental understanding of GaAs NWs toward future mass production of the NW arrays in devices.

The author performed a set of NW growth experiments on both native and thermal Si oxide substrates using an MBE system characterized by SEM. The author demonstrates technically feasible approaches for engineering of NW growth, addressing size homogeneity, position-control, and suppression of parasitic growth. On native Si oxide substrates ($\sim$1 nm thickness), the author first could successfully manipulate the NW sizes and density using available literature. Then a new strategy of growth is proposed, which leads to a uniform size of the NWs and relatively high control on parasitic growth. The strategy includes Ga pre-deposition with homogeneous sizes, and a consequent growth step from the deposited Ga droplets. It was revealed that by employing high substrate temperatures and low Ga fluxes, after the Ga positioning, one could con-

trol the diameter and length distributions down to a standard deviation within 3−6% of the average values. Moreover, the NW to parasitic island ration increased to above 30. On the Si thermal oxide substrates ($>$ 15 nm thickness), a focused ion beam patterning technique was reported and detailed to achieve high yield of NW growth. It was revealed that an interplay between ion doses, wet etching, and high-temperature steps define the quality of growth. In particular, the diameter of the holes turned out to be the key, which we could widely manipulate and control, leading to above 80 % of NW growth. Using FIB, we demonstrate a platform to pattern Si substrates for GaAs self-catalyzed NW growth. FIB patterning can attract significant attention in the future because a lithography-free single-step offers the patterning. Another advantage is the fundamental simplicity where a small window of trial and error can efficiently result in a high yield of growth. Our results can also be qualitatively considered for other systems of NW growth to substitute other patterning techniques.

In the next set of experiments, the NWs were in-situ characterized using a micrometer-sized X-ray beam at a synchrotron source with high illumination. Combining a small X-ray beam size and controlled NW density led to resolving XRD signal from individual NWs. Here, we report on our technical achievements in performing this sophisticated experiment for the first time. Moreover, fundamental understandings are acquired about NW behavior and the dynamics under MBE growth conditions.An individual NW is monitored during the process of growth utilizing μXRD. In particular, the evolution of the volume, diameter, length, angular misorientation, and the overall polytypic characteristics of a growing NW are resolved. It is revealed that the NW growth includes two stages. In the first stage, the NW grows mainly axially. Here, it is found that the NW oscillates within 0.1° while it is tilted a few tenths of a degree. In the second stage of the NW growth, radial growth is dominant. The angular oscillations of the NW stops and the NW tilts toward the surface normal. Individual NWs and PIs are monitored by μXRD at the NW growth temperature under different MBE conditions: i) without source supply, ii) with As supply, iii) with both As and Ga fluxes. Moreover, several complementary annealing studies were performed on both native and thermal Si oxide substrates utilizing ex-situ SEM. It was revealed that without the supply of source material, at temperatures below 510±5 °C, the GaAs solid surfaces are thermally stable. However, the Ga particles decrease the size or vanish increasingly by an intermediate step of exposure to air after growth and before annealing. At temperatures above 660 °C, the GaAs material entirely evaporates within an hour. At a temperature of 610 °C, taking advantage of the slow dynamics of evaporation, the nano-objects were monitored for several hours. We evidenced that the NWs become angularly unstable along with

the evaporation of NW facets. Moreover, by prolongation of annealing time, the NWs tilt and eventually fall flat on the substrate. That is documented for a range of different growth samples on native or thermal oxide Si substrates, and on samples with or without an intermediate exposure to air. The XRD data evidenced that the dynamics of evaporation with As supply were similar to that without supply. Before the NWs fall down, they vibrate or bend. By supply of both As and Ga fluxes, the vibrations/bendig can be reversed. Moreover, similar to the findings in single NW growth, the NWs tilt back toward the substrate normal, while the NW facets increase (radial growth).

Outlooks

"*The greatest enemy of knowldge is not ignorance, it is illusion of knowledge.*" Stephen Hawkings

The outlooks of this work can be divided into three categories:

1) In this thesis, the first successful in-situ monitoring of individual NWs at MBE growth conditions was performed using μXRD. By the analysis methods we developed in this thesis, the potential future studies can address dynamical monitoring of volume, size, structure, and angular misorientation of the overgrown nano-objects on hetero or homo-epitaxial substrates. This opens up a possible platform for a wide range of future studies in different material systems.

2) There are a set of experiments which I proposed and performed along with this thesis. They were either a continuation or interconnectedly relevant to the presented data, so they were preliminarily analyzed. These results are not included in this thesis, and some of them were mentioned at the end of Chapter 1.

- Along with the annealing studies in this thesis, the WZ and ZB phase-dependent evaporation kinetics at the NWs were monitored on a few NW samples. In particular, the different samples were illuminated by both micrometer-sized and millimeter-sized X-ray beams within a temperature range of 300 − 660 °C. In this way, XRD RSM data are resolved from individual NWs and PIs, as well as thousands simultaneously illuminated nano-objects. The full analysis of the available experimental data would contribute in the following understandings: i) temperature-dependent evaporation kinetics of WZ, ZB, and mixed crystal phases at both NWs and PIs, ii) size-dependent expansion coefficients of the NWs and PIs.

- Along with the several annealing studies in this work, we observed indications of NW capsulation. In particular, the NWs showed a protective layer of carbon, leading to suppression of evaporation at high-temperatures (above 660 °C). Such a finding was not a part of the initial scope but an interesting side-observation. For chemical analysis of the surface, energy-dispersive X-ray spectroscopy analysis within SEM and X-ray photoemission spectroscopy was utilized. The preliminary analysis of data revealed that carbon species stick to the surface in air and by exposure to SEM. The typical cleaning procedures could not entirely remove the carbon species, leading to the formation of carbon layers (likely carbon nano-ribbons) on the surface.

- As a complement to the studied NW processing effects, I exposed NW samples to Ga supply during in-situ μXRD experiments, illuminating individual NWs. Additional samples were studied by ex-situ SEM and in-situ RHEED. It was revealed that the NWs which are stable for several hours without Ga supply at high-temperatures, can fully evaporate within a minute with Ga supply. The full analysis of data can reveal evaporation kinetics of NWs in the presence of Ga supply (Ga etching dynamics).

- After monitoring the Ga etching of an individual NW, the NW was regrown along with RSM XRD. The full analysis of the data will represent the second in-situ monitoring of an individual NW growth monitored by μXRD.

3) The fundamental understandings, which we developed in this work, can open up new questions for further investigations. Two examples are as follows.

- It was found that at the initial stages of NW growth, NWs mainly grow axially. After a time gap, the radial growth starts. It would be interesting to see how this gap is influenced by NW characteristics as well as the growth conditions. That can shed light on the effects of substrate diffusion lengths on the NW growth.

- It was found that the NWs vibrate/bend by annealing after facet shrinkage. Because the presented experiments cannot unambiguously distinguish the effect of static bending or dynamic vibrations, I would propose to disentangle these phenomena by future optical interferometric investigations similar to ref. [177].

Bibliography

[1] M. R. Ramdani, E. Gil, C. Leroux, Y. Andre, A. Trassoudaine, D. Castelluci, L. Bideux, G. Monier, C. Robert-Goumet, and R. Kupka, "Fast Growth Synthesis of GaAs Nanowires with Exceptional Length," *Nano Lett.*, vol. 10(5), no. 1836-1841, 2010.

[2] B.-C. Zhang, H. Wang, L. He, C.-J. Zheng, J.-S. Jie, Y. Lifshitz, S.-T. Lee, and X.-H. Zhang, "Centimeter-Long Single-Crystalline Si Nanowires," *Nano Lett.*, vol. 17(12), no. 1530-6984, 2017.

[3] C. M. Lieber, "One-Dimensional Nanostructures: Chemistry, Physics and Applications," *Solid State Commun.*, vol. 107, no. 607, 1998.

[4] J. Hu, T. W. Odom, and C. M. Lieber, "Chemistry and Physics in One Dimension: Synthesis and Properties of Nanowires and Nanotubes," *Acc. Chem. Res.*, vol. 32(5), no. 435-445, 1999.

[5] G. E. Moore, "Cramming more components onto integrated circuits," *Electronics*, vol. 38, no. 8, 1965.

[6] C. Thelander, P. Agarwal, S. Brongersma, J. Eymery, L. F. Feiner, A. Forchel, M. Scheer, W. Riess, B. J. Ohlsson, U. Gosele, and L. Samuelson, "Nanowire-based one-dimensional electronics," *Mater. Today*, vol. 9, no. 10, 2006.

[7] P. Yang, R. Yan, and M. Fardy, "Semiconductor Nanowire: What's Next?" *Nano Lett.*, vol. 10, no. 1529-1536, 2010.

[8] B. Yirka, "New nanowire transistors may help keep Moore's Law alive," https://phys.org/news/2013-05-nanowire-transistors-law-alive.html, May 2013, accessed: 6 Jun 2019.

[9] "Why Use Gallium Arsenide Solar Cells?" https://www.altadevices.com/use-gallium-arsenide-solar-cells/, Oct. 2017, accessed: 3 Jun 2019.

[10] X. Miao, K. Chabak, C. Zhang, P. K. Mohseni, J. W, D., and X. Li, "High-Speed Planar GaAs Nanowire Arrays with fmax > 75 GHz by Wafer-Scale Bottom-up Growth," *Nano Lett.*, vol. 15, no. 2780-2786, 2015.

[11] M. A. Seyedi, M. Yao, J. OBrien, S. Y. Wang, and P. D. Dapkus, "Efficient Schottky-like junction GaAs nanowire photodetector with 9 GHz modulation bandwidth with large active area," *Appl. Phys. Lett.*, vol. 105, no. 041105, 2014.

[12] X. Dai, S. Zhang, Z. Wang, G. Adamo, H. Liu, Y. Huang, C. Couteau, and C. Soci, "GaAs/AlGaAs Nanowire Photodetector," *Nano Lett.*, vol. 14(5), no. 2688-2693, 2014.

[13] K. Peng, P. Parkinson, L. Fu, Q. Gao, N. Jiang, Y.-N. Guo, F. Wang, H. J. Joyce, J. L. Boland, H. H. Tan, C. Jagadish, and M. B. Johnston, "Single Nanowire Photoconductive Terahertz Detectors," *Nano Lett.*, vol. 15, no. 206-210, 2015.

[14] M.-H. Bae, B.-K. Kim, D.-H. Ha, S. J. Lee, R. Sharma, K. J. Choi, J.-J. Kim, W. J. Choi, and J. Shin, "Non-Lithographic Growth of Core-Shell GaAs Nanowires on Si for Optoelectronic Applications," *C. Cryst. Growth Des.*, vol. 14(4), no. 1510-1515, 2014.

[15] K. Tomioka, J. Motohisa, S. Hara, K. Hiruma, and T. Fukui, "GaAs/AlGaAs Core Multishell Nanowire-Based Light-Emitting Diodes on Si," *Nano Lett.*, vol. 10, no. 1639-1644, 2010.

[16] T. Martensson, C. P. T. Svensson, B. A. Wacaser, M. W. Larsson, W. Seifert, K. Deppert, A. Gustafsson, L. R. Wallenberg, and L. Samuelson, "Epitaxial III-V nanowires on silicon," *Nano Lett.*, vol. 4, no. 1987, 2004.

[17] A. Biermanns, S. Breuer, A. Trampert, A. Davydok, L. Geelhaar, and U. Pietsch, "Strain Accommodation in Ga-Assisted GaAs Nanowires Grown on Silicon (111)," *Nanotechnology*, vol. 23, no. 305703, 2012.

[18] M. T. Bjork, B. J. Ohlsson, T. Sass, A. I. Persson, C. Thelander, M. H. Magnusson, K. Deppert, L. R. Wallenberg, and L. Samuelson, "One-dimensional Steeplechase for Electrons Realized," *Nano Lett.*, vol. 2, no. 87, 2002.

[19] R. S. Wagner and W. C. Ellis, "Vapor-Liquid-Solid Mechanism of Single Crystal Growth," *Appl. Phys. Lett.*, vol. 4, no. 89, 1964.

[20] Z. H. Wu, X. Y. Mei, D. Kim, M. Blumin, and H. E. Ruda, "Growth of Au-catalyzed ordered GaAs nanowire arrays by molecular-beam epitaxy," *Appl. Phys. Lett.*, vol. 81, no. 5177, 2002.

[21] F. Martelli, S. Rubini, M. Piccin, G. Bais, F. Jabeen, S. De Franceschi, V. Grillo, E. Carlino, F. D'Acapito, F. Boscherini, S. Cabrini, M. Lazzarino, L. Businaro, F. Romanato, and A. Franciosi, "Manganese-Induced growth of GaAs nanowires," *Nano Lett.*, vol. 6, no. 9, 2006.

[22] C. Lindberg, A. Whiticar, K. A. Dick, N. Skold, J. Nygard, and J. Bolinsson, "Silver as Seed-Particle Material for GaAs Nanowires-Dictating Crystal Phase and Growth Direction by Substrate Orientation," *Nano Lett.*, vol. 16(4), no. 2181-2188, 2016.

[23] S. Heun, B. Radha, D. Ercolani, G. U. Kulkarni, F. Rossi, V. Grillo, G. Salviati, F. Beltram, and L. Sorba, "Pd-Assisted growth of InAs nanowires," *Cryst Growth Des.*, vol. 10, no. 9, 2010.

[24] A. F. iMorral, C. Colombo, and G. Abstreiter, "Nucleation Mechanism of Gallium-Assisted Molecular Beam Epitaxy Growth of Gallium Arsenide Nanowires," *Appl. Phys. Lett.*, vol. 92, no. 063112, 2008.

[25] S. Breuer, C. Pfuller, T. Flissikowski, O. Brandt, H. T. Grahn, L. Geelhaar, and H. Riechert, "Suitability of Au- and Self-Assisted GaAs Nanowires for Optoelectronic Applications," *Nano Lett.*, vol. 11(3), no. 1276-1279, 2010.

[26] B. Bauer, A. Rudolph, M. Soda, A. Fontcuberta i Morral, J. Zweck, D. Schuh, and E. Reiger, "Position controlled self-catalyzed growth of GaAs nanowires by molecular beam epitaxy," *Nanotechnology*, vol. 21, no. 435601, 2010.

[27] G. E. Cirlin, V. G. Dubrovskii, Y. B. Samsonenko, A. D. Bouravleuv, K. Durose, Y. Y. Proskuryakov, B. Mendes, L. Bowen, M. A. Kaliteevski, R. A. Abram, and D. Zeze, "Self-catalyzed, pure zincblende GaAs nanowires grown on Si(111) by molecular beam epitaxy," *Phys. Rev. B*, vol. 82(3), no. 035302, 2010.

[28] A. Fontcuberta i Morral, "Gold-Free GaAs Nanowire Synthesis and Optical Properties," *IEEE J. Sel. Top. Quantum Electron.*, vol. 17, no. 819-828, 2011.

[29] S. Ambrosini, F. V. Grillo, A. Franciosi, and S. Rubini, "Vapor-Liquid-Solid and Vapor-Solid Growth of Self-Catalyzed GaAs Nanowires," *AIP Advances*, vol. 1, no. 042142, 2011.

[30] E. Russo-Averchi, M. Heiss, L. Michelet, P. Krogstrup, J. Nygard, C. Magen, J. R. Morante, E. Uccelli, J. Arbiol, and A. F. iMorral, "Suppression of three dimensional twinning for a 100 percent yield of vertical GaAs nanowires on silicon," *Nanoscale*, vol. 4, no. 1486-1490, 2012.

[31] V. G. Dubrovskii, T. Xu, A. D. Alvarez, S. R. Plissard, P. Caroff, F. Glas, and B. Grandidier, "Self-Equilibration of the Diameter of Ga-Catalyzed GaAs Nanowires," *Nano Lett.*, vol. 15(8), no. 5580-5584, 2015.

[32] F. Matteini, V. G. Dubrovskii, D. Ruffer, G. Tutuncuoglu, Y. Fontana, and A. F. iMorral, "Tailoring the Diameter and Density of Self-Catalyzed GaAs Nanowires on Silicon," *Nanotechnology*, vol. 26(10), no. 105603, 2015.

[33] L. Balaghi, T. Tauchnitz, R. Hubner, L. Bischoff, H. Schneider, M. Helm, and E. Dimakis, "Droplet-confined alternate pulsed epitaxy of gaas nanowires on si substrates down to cmos-compatible temperatures," *Nano Letters*, vol. 16(7), no. 4032-4039, 2016.

[34] F. Bastiman, H. Kuepers, C. Somaschini, and L. Geelhaar, "Growth map for Ga-assisted growth of GaAs nanowires on Si(111) substrates by molecular beam epitaxy," *Nanotechnology*, vol. 27, no. 9, 2016.

[35] E. S. Koivusalo, T. V. Hakkarainen, M. D. Guina, and V. G. Dubrovskii, "Sub-Poissonian Narrowing of Length Distributions Realized in Ga-Catalyzed GaAs Nanowires," *Nano Lett.*, vol. 17(9), no. 5350-5355, 2017.

[36] E. Koivusalo, T. Hakkarainen, and M. Guina, "Structural Investigation of Uniform Ensembles of Self-Catalyzed GaAs Nanowires Fabricated by a Lithography-Free Technique," *Nanoscale Res. Lett.*, vol. 12(1), no. 192, 2017.

[37] J. Vukajlovic-Plestina, W. Kim, V. G. Dubrovski, G. Tutuncuoglu, M. Lagier, H. Potts, and A. Friedl, M. und Fontcuberta iMorral, "Engineering the Size Distributions of Ordered GaAs Nanowires on Silicon," *Nano Lett.*, vol. 17, no. 4101-4108, 2017.

[38] E. S. Koivusalo, T. V. Hakkarainen, H. V. A. Galeti, Y. G. Gobato, V. G. Dubrovskii, and M. D. Guina, "Deterministic Switching of the Growth Direction of Self-Catalyzed GaAs Nanowires," *Nano Lett.*, vol. 19(1), no. 82-89, 2019.

[39] S. Breuer, F. Karouta, H. H. Tan, and C. Jagadish, "Mocvd growth of gaas nanowires using ga droplets," in *COMMAD 2012*, no. 39-40, 2012.

[40] Y. Takahashi, T. Soga, S. Sakai, M. Umeno, and S. Hattori, "Mechanism of mocvd growth for gaas and alas," *Jpn. J. Appl. Phys*, vol. 23(6), no. 709-713, 1984.

[41] Z. Dong, Y. Andre, V. G. Dubrovskii, C. Bougerol, C. Leroux, M. R. Ramdani, G. Monier, A. Trassoudaine, D. Castelluci, and E. Gil, "Self-catalyzed gaas nanowires on silicon by hydride vapor phase epitaxy," *Nanotechnology*, vol. 28(12), no. 125602, 2017.

[42] L. Guniat, P. Caroff, and A. Fontcuberta i Morral, "Vapor phase growth of semiconductor nanowires: Key developments and open questions," *Chemical Reviews*, vol. 0, no. 0, p. null, 0.

[43] J. Jo, Y. Tchoe, G. C. Yi, and M. Kim, "Real-Time Characterization Using in situ RHEED Transmission Mode and TEM for Investigation of the Growth Behaviour of Nanomaterials," *Sci. Rep*, vol. 8, no. 1694, 2018.

[44] M. Tchernycheva, J. C. Harmand, G. Patriarche, L. Travers, and G. E. Cirlin, "Temperature Conditions for GaAs Nanowire Formation by Au-assisted Molecular Beam Epitaxy," *Nanotechnology*, vol. 17, no. 4025, 2006.

[45] S. H. Oh, M. F. Chisholm, Y. Kauffmann, W. D. Kaplan, W. Luo, M. Ruhle, and C. Scheu, "Oscillatory Mass Transport in Vapor-Liquid-Solid Growth of Sapphire Nanowires," *Science*, vol. 330, no. 489-493, 2010.

[46] C. Y. Wen, J. Tersoff, K. Hillerich, M. C. Reuter, J. H. Park, S. Kodambaka, E. A. Stach, and F. M. Ross, "Periodically Changing Morphology of the Growth Interface in Si, Ge, and GaP Nanowires," *Phys. Rev. Lett.*, vol. 107, no. 025503, 2011.

[47] D. Jacobsson, F. Panciera, J. Tersoff, M. C. Reuter, S. Lehmann, S. Hofmann, K. A. Dick, and F. M. Ross, "Interface Dynamics and Crystal Phase Switching in GaAs Nanowires," *Nature*, vol. 531, no. 317-322, 2016.

[48] Y. Wu and P. Yang, "Direct Observation of Vapor-Liquid-Solid Nanowire Growth," *J. Am. Chem. Soc.*, vol. 123, no. 3165-3166, 2001.

[49] D. E. Aspnes, J. P. Harbison, A. A. Studna, and L. T. Florez, "Optical reflectance and electron diffraction studies of molecular-beam-epitaxy growth transients on GaAs(001)," *Phys. Rev. Lett.*, vol. 59 (15), no. 1687-1690, 1987.

[50] W. G. Breiland and K. P. Killeen, "A virtual interface method for extracting growth rates and high temperature optical constants from thin semiconductor

films using insitu normal incidence reflectance," *J. Appl. Phys.*, vol. 78 (11), no. 6726-6736, 1995.

[51] S. Tsukamoto and N. Koguchi, "Atomic-level in situ real-space observation of Ga adatoms on GaAs(001)(2X4)-As surface during molecular beam epitaxy growth," *J. Cryst. Growth*, vol. 201, no. 118-202, 1999.

[52] S. Fernandez-Garrido, J. K. Zettler, L. Geelhaar, and O. Brandt, "Monitoring the Formation of Nanowires by Line-of-Sight Quadrupole Mass Spectrometry: A Comprehensive Description of the Temporal Evolution of GaN Nanowire Ensembles," *Nano Lett.*, vol. 15 (3), no. 1930-1937, 2015.

[53] N. Shin and M. A. Filler, "Controlling Silicon Nanowire Growth Direction via Surface Chemistry," *Nano Lett.*, vol. 12(6), no. 2865-2870, 2012.

[54] M. Takahashi, M. Kozu, and T. Sasaki, "Effects of Growth Temperature and Growth Rate on Polytypes in Gold-Catalyzed GaAs Nanowires Studied by in-situ X-ray Diffraction," *Jpn. J. Appl. Phys*, vol. 55, no. 04EJ04, 2016.

[55] M. Takahashi, M. Kozu, T. Sasaki, and W. Hu, "Mechanisms Determining the Structure of Gold-Catalyzed GaAs Nanowires Studied by in-situ X-ray Diffraction," *Cryst. Growth Des.*, vol. 15, no. 4979-4985, 2015.

[56] P. Krogstrup, M. H. Madsen, W. Hu, M. Kozu, Y. Nakata, J. Nygard, M. Takahasi, and R. Feidenhans'l, "In-situ X-ray Characterization of Wurtzite Formation in GaAs Nanowires," *Appl. Phys. Lett.*, vol. 100, no. 093103, 2012.

[57] P. Schroth, M. Koehl, J. W. Hornung, E. Dimakis, C. Somaschini, L. Geelhaar, A. Biermanns, S. Bauer, S. Lazarev, U. Pietsch, and T. Baumbach, "Evolution of Polytypism in GaAs Nanowires during Growth Revealed by Time-Resolved in-situ X-ray Diffraction," *Phys. Rev. Lett.*, vol. 114, no. 055504, 2015.

[58] P. Schroth, J. Jakob, L. Feigl, S. M. Mostafavi Kashani, J. Vogel, J. Strempfer, T. F. Keller, U. Pietsch, and T. Baumbach, "Radial Growth of Self-Catalyzed GaAs Nanowires and the Evolution of the Liquid Ga-Droplet Studied by Time-Resolved in-situ X-ray Diffraction," *Nano Lett.*, vol. 18, no. 101-108, 2018.

[59] A. Biermanns, E. Dimakis, A. Davydok, T. Sasaki, L. Geelhaar, M. Takahasi, and U. Pietsch, "Role of Liquid Indium in the Structural Purity of Wurtzite InAs Nanowires that Grow on Si(111)," *Nano Lett.*, vol. 14, no. 6878-6883, 2014.

[60] R. S. Pennington, J. Jinschek, J. B. Wagner, C. Boothroyd, and R. E. Dunin-Borkowski, “Atomic Resolution Imaging of in-situ InAs Nanowire Dissolution at Elevated Temperature,” *J. Phys. Conf. Ser*, vol. 209, no. 012013, 2010.

[61] H. Zheng, J. Wang, J. Y. Huang, J. Wang, Z. Zhang, and S. X. Mao, “Dynamic Process of Phase Transition from Wurtzite to Zinc Blende Structure in InAs Nanowires,” *Nano Lett.*, vol. 13, no. 6023-6027, 2013.

[62] S. Ambrosini, J. B. Wagner, T. Booth, A. Savenko, G. Fragiacomo, P. Boggild, and S. Rubini, “In-situ Transmission Electron Microscopy Analyses of Thermally Annealed Self-Catalyzed GaAs Nanowires Grown by Molecular Beam Epitaxy,” *18th Int. Symp. of (Nanostructures: Physics and Technology) Ekaterinburg, Russia, June 20-25*, 2011.

[63] C. Hammond, *The Basics of Crystallography and Diffraction.* Oxford Science Publications, 2001.

[64] “Tetrahedral molecular geometry,” https://en.wikipedia.org/wiki/Tetrahedral molecular geometry, accessed: 16 Jun 2019.

[65] O. Madelung, *Semiconductors: Data Handbook.* Springer, Berlin, Heidelberg, 2004.

[66] D. Jacobsson, F. Yang, K. Hillerich, F. Lenrick, S. Lehmann, D. Kriegner, J. Stangl, L. R. Wallenberg, K. A. Dick, and J. Johansson, “Phase transformation in radially merged wurtzite GaAs nanowires,” *Cryst. Growth Des.*, vol. 15, no. 4795-4803, 2015.

[67] K. G. Guenther, “Aufdampfschichten aus halbleitenden Ill-V-Verbindungen [Evaporated Films of III-V Semiconducting Compounds],” *Z. Naturf.*, vol. 13a, no. 1081-1089, 1958.

[68] H. Freller and K. G. Guenther, “Three-temperature method as an origin of molecular beam epitaxy,” *Thin Solid Films*, vol. 88(4), no. 291-307, 1982.

[69] M. Henini, Ed., *Molecular Beam Epitaxy from research to mass production.* Elsevier, 2012.

[70] T. Slobodskyy, P. Schroth, D. Grigoriev, A. A. Minkevich, D. Z. Hu, S. D. M., and T. Baumbach, “A Portable Molecular Beam Epitaxy System for in-situ X-ray Investigations at Synchrotron Beamlines,” *Rev. Sci. Instrum*, vol. 83, no. 105112, 2012.

[71] "The Nobel Prize in Physics 1901 - An Illuminating Accident," Nobelprize.org, accessed: 9 Jan 2019.

[72] "Nobel Prize in Physics 1914 - Presentation," Nobelprize.org, accessed: 9 Jan 2019.

[73] S. Galli, "X-ray Crystallography: One Century of Nobel Prizes," *J. Chem. Educ.*, vol. 91, no. 2009, 2014.

[74] J. Strempfer, S. Francoual, D. Reuther, D. K. Shukla, A. Skaugen, H. Schulte-Schrepping, T. Kracht, and H. Franz, "Resonant scattering and diffraction beamline P09 at PETRA III," *J. Synchrotron Radiat*, vol. 20, no. 4, 2013.

[75] J. Vogel, *Master thesis - Limits for X-ray nanowire difraction with synchrotron radiation.* Univeristy of Siegen, Physics Department, 2016.

[76] "Nobel Prize in Physics 1915 - Presentation speech," Nobelprize.org, accessed: 9 Jan 2019.

[77] M. Koehl, *Analysis of nanostructures based on diffraction of X-ray radiation.* Fakultat fur Physik des Karlsruher Instituts fur Technologie(KIT), 2014.

[78] U. Pietsch, V. Holy, and T. Baumbach, *High-Resolution X-Ray Scattering from Thin Films and Lateral Nanostructures.* Springer, 2004.

[79] S. M. Mostafavi Kashani, D. Kriegner, D. Bahrami, J. Vogel, A. Davtyan, L. Feigl, P. Schroth, J. Jakob, T. Baumbach, and U. Pietsch, "X-ray Diffraction Analysis of the Angular Stability of Self-Catalyzed GaAs Nanowires for Future Applications in Solar Light Harvesting and Light Emission Devices," *ACS Appl. Nano Mater.*, vol. 2(2), no. 689-699, 2019.

[80] A. Authier, *Dynamical theory of x-ray diffraction.* Oxford University Press, New York, 2004.

[81] R. Mehrem, "The Plane Wave Expansion, Infinite Integrals and Identities involving Spherical Bessel Functions," *APPL MATH COMPUT*, vol. 217(12), no. 5360-5365, 2009.

[82] M. Schmidbauer, *X-ray diffuse scattering from self-organized mesoscopic semiconductor structures.* Springer, Berlin New York, 2004.

[83] J. Als-Nielsen and D. McMorrow, *Elements of Modern X-ray Physics, 2nd Edition.* John Wiley and Sons Ltd, 2011.

[84] I. K. Robinson, "Crystal truncation rods and surface roughness," *Physical Review B*, vol. 33, no. 3830, 1986.

[85] I. A. Vartanyants and I. K. Robinson, "Partial coherence effects on the imaging of small crystals using coherent x-ray diffraction," *J. Phys. Condens. Matter*, vol. 13, no. 10593, 2001.

[86] "MATLAB," https://www.mathworks.com/products/matlab.html, accessed: 28 Jun 2019.

[87] T. Hakkarainen, A. Schramm, J. Makela, P. Laukkanen, and M. Guina, "Lithography-free oxide patterns as templates for selfcatalyzed growth of highly uniform GaAs nanowires on Si(111)," *Nanotechnology*, vol. 26, no. 275301, 2015.

[88] T. Tauchnitz, T. Nurmamytov, R. Hubner, M. Engler, S. Facsko, H. Schneider, M. Helm, and E. Dimakis, "Decoupling the Two Roles of Ga Droplets in the Self-Catalyzed Growth of GaAs Nanowires on SiOx/Si(111) Substrates," *Cryst. Growth Des.*, vol. 17(10), no. 5276-5282, 2017.

[89] C. Colombo, D. Spirkoska, M. Frimmer, G. Abstreiter, and A. Fontcuberta i Morral, "Ga-assisted catalyst-free growth mechanism of GaAs nanowires by molecular beam epitaxy," *Phys. Rev. B*, vol. 77, no. 155326, 2008.

[90] J. H. Paek, T. Nishiwaki, M. Yamaguchi, and N. Sawaki, "Catalyst free MBE-VLS growth of GaAs nanowires on Si(111) substrate," *Phys. Status Solidi C*, vol. 6, no. 1436-1440, 2009.

[91] A. M. Munshi, D. L. Dheeraj, V. T. Fauske, D. C. Kim, J. Huh, and L. Reinertsen, J. F. und Ahtapodov, "Position-controlled uniform GaAs nanowires on silicon using nanoimprint lithography," *Nano Lett.*, vol. 14, no. 960-966, 2014.

[92] H. Kuepers, F. Bastiman, E. Luna, C. Somaschini, and L. Geelhaar, "Ga predeposition for the Ga-assisted growth of GaAs nanowire ensembles with low number density and homogeneous length," *Journal of Crystal Growth*, vol. 459, no. 43-49, 2017.

[93] H. Kuepers, A. Tahraoui, R. B. Lewis, S. Rauwerdink, M. Matalla, O. Krueger, F. Bastiman, H. Riechert, and L. Geelhaar, "Surface Preparation and Patterning by Nano Imprint Lithography for the Selective Area Growth of GaAs Nanowires on Si(111)," *Semicond. Sci. Technol.*, vol. 32, no. 115003, 2017.

[94] S. J. Gibson, J. P. Boulanger, and R. R. LaPierre, “Opportunities and Pitfalls in Patterned Self-Catalyzed GaAs Nanowire Growth on Silicon,” *Semicond. Sci. Technol.*, vol. 28, no. 105025, 2013.

[95] P. Schroth, *Growth of self-catalyzed GaAs nanowires using molecular-beam-epitaxy and structural characterization by in-situ X-ray diffraction.* Naturwissenschaftlich-Technischen Fakultaet der Universitaet Siegen, 2016.

[96] P. Schroth, J. Jakob, L. Feigl, S. M. Mostafavi Kashani, U. Pietsch, and T. Baumbach, “Lithography-Free Variation of the Number Density of Self-Catalyzed GaAs Nanowires and its Impact on Polytypism,” *MRS Communications*, vol. 145, no. 1-7, 2018.

[97] D. Bahrami, M. K. S.M., A. Al Hassan, A. Davtyan, and U. Pietsch, “High yield of self-catalyzed GaAs nanowire growth on silicon (111) substrate templated by focused ion beam patterning,” *Nanotechnology*, vol. 31, no. 18, 2020.

[98] L. T. T. Giang, C. Bougerol, H. Mariette, and R. Songmuang, “Intrinsic Limits Governing MBE Growth of Ga-assisted GaAs Nanowires on Si(111),” *J Cryst Growth.*, vol. 364, pp. 118 – 122, 2013.

[99] Y. B. Samsonenko, G. E. Cirlin, A. I. Khrebtov, A. D. Bouravleuv, N. K. Polyakov, V. P. Ulin, V. G. Dubrovskii, and P. Werner, “Study of Processes of Self-Catalyzed Growth of GaAs Crystal Nanowires by Molecular-Beam Epitaxy on Modified Si (111) Surfaces,” *Semiconductors*, vol. 45(4), no. 431-435, 2011.

[100] T. Rieger, S. Heiderich, S. Lenk, M. I. Lepsa, and D. Gruetzmacher, “Ga-assisted MBE growth of GaAs nanowires using thin HSQ layer,” *J. Cryst. Growth*, vol. 353, no. 39-46, 2012.

[101] F. Matteini, G. Tutuncuoglu, R. D., E. Alarcon-Llado, and A. F. i Morral, “Ga-assisted growth of gaas nanowires on silicon, comparison of surface siox of different nature,” *J. Cryst. Growth*, vol. 404, no. 246-255, 2014.

[102] F. Matteini, G. Tutuncuoglu, D. Mikulik, J. Vukajlovic-Plestina, H. Potts, J.-B. Leran, W. C. Carter, and A. Fontcuberta i Morral, “Impact of the Ga Droplet Wetting, Morphology, and Pinholes on the Orientation of GaAs Nanowires,” *Cryst. Growth Des.*, vol. 16, no. 5781-5786, 2016.

[103] Y. Nitta, M. Shibata, K. Fujita, and M. Ichikawa, “Nanometer-scale Si selective growth on Ga-adsorbed voids in ultrathin SiO2 films,” *Surf. Sci.*, vol. 431, no. L565, 1999.

[104] C. Somaschini, S. Bietti, A. Trampert, U. Jahn, C. Hauswald, H. Riechert, S. Sanguinetti, and L. Geelhaar, "Control over the Number Density and Diameter of GaAs Nanowires on Si(111) Mediated by Droplet Epitaxy," *Nano Lett.*, vol. 13(8), no. 3607-3613, 2013.

[105] P. Schroth, M. Al Humaidi, L. Feigl, J. Jakob, A. Al Hassan, A. Davtyan, H. Kuepers, A. Tahraoui, L. Geelhaar, U. Pietsch, and T. Baumbach, "Impact of the shadowing effect on the crystal structure of patterned self-catalyzed gaas nanowires," *Nano Letters*, vol. 19(7), no. 4263-4271, 2019.

[106] L. Daweritz and R. Hey, "Reconstruction and defect structure of vicinal GaAs(001) and AlxGa1-xAs(001) surfaces during MBE growth," *Surf. Sci.*, vol. 236, no. 15, 1990.

[107] A. Y. Cho, "Bonding direction and surface-structure orientation on GaAs (001)," *J. Appl. Phys.*, vol. 47, no. 2841-2843, 1976.

[108] R. D. Richards, F. Bastiman, C. J. Hunter, D. F. Mendes, A. R. Mohmad, J. S. Roberts, and J. P. David, "Molecular beam epitaxy growth of GaAsBi using As2 and As4," *J. Cryst. Growth*, vol. 390, no. 120-124, 2014.

[109] "Dr. Faebian Bastiman," faebianbastiman.wordpress.com, accessed: 4 March 2019.

[110] J. H. Neave, B. A. Joyce, P. J. Dobson, and N. Norton, "Dynamics of film growth of GaAs by MBE from Rheed observations," *AppI. Phys. A*, vol. 31(1), no. 1-8, 1983.

[111] N. Masud and P. J. B., "Theory of RHEED," *J. Phys. C: Solid State Phys.*, vol. 9(10), no. 1833-1844, 1976.

[112] I. P. Soshnikov, G. E. Cirlin, A. A. Tonkikh, V. N. Nevedomskii, Y. B. Samsonenko, and V. M. Ustinov, "Electron diffraction on GaAs nanowhiskers grown on Si(100) and Si(111) substrates by molecular-beam epitaxy," *Phys. Solid State*, vol. 49(8), no. 1440-1445, 2007.

[113] D. Rudolph, S. Hertenberger, S. Bolte, W. Paosangthong, D. Spirkoska, M. Doeblinger, M. Bichler, J. J. Finley, G. Abstreiter, and G. Koblmueller, "Direct Observation of a Noncatalytic Growth Regime for GaAs Nanowires," *Nano Lett.*, vol. 11(9), no. 3848-3854, 2011.

[114] K. Watanabe, N. Koguchi, and Y. Gotoh, "Fabrication of GaAs Quantum Dots by Modified Droplet Epitaxy," *Jpn. J. Appl. Phys.*, vol. 39, no. L79-L81, 2000.

[115] A. Nemcsics, "Formation Kinetics of the Self-organized III-Vbased Nanostructures Grown by Droplet Epitaxy," *Acta polytech. Hung.*, vol. 8, no. 4, 2011.

[116] Y. Wang, A. S. Ozcan, C. Sanborn, and K. F. Ludwig, "Real-time x-ray studies of gallium nitride nanodot formation by droplet heteroepitaxy," *J. Appl. Phys. 102, 073522*, vol. 102, no. 073522, 2007.

[117] H. Y. Chen, H. W. Lin, C. H. Shen, and S. Gwo, "Structure and Photoluminescence Properties of Epitaxially Oriented GaN Nanorods Grown on Si(111) by Plasma-Assisted MolecularBeam Epitaxy," *Appl. Phys. Lett.*, vol. 89, no. 243105, 2006.

[118] K. L. Mittal, Ed., *Proceeding of third symposium on Particles on surfaces: detection, adhesion, and removal*, San Diego, California, August 21-25, 1990.

[119] A. Busnaina and I. Kashkoush, "The effect of time, temperature and particle size on submicron particle removal using ultrasonic cleaning," *CHEM ENG COMMUN*, vol. 125, no. 1, 1993.

[120] C. Chatillon and C. D., "Congruent Vaporization of GaAs(s) and Stability of Ga(l) Droplets at the GaAs(s) Surface," *J Cryst Growth.*, vol. 151, no. 91-101, 1995.

[121] Z. Y. Zhou, C. X. Zheng, W. X. Tang, D. E. Jesson, and J. Tersoff, "Congruent Evaporation Temperature of GaAs (001) Controlled by As Flux," *Appl. Phys. Lett.*, vol. 97, no. 121912, 2010.

[122] B. Mandl, J. Stangl, E. Hilner, A. A. Zakharov, K. Hillerich, A. W. Dey, L. Samuelson, G. Bauer, K. Deppert, and A. Mikkelsen, "Growth Mechanism of Self-Catalyzed Group III-V Nanowires," *Nano Lett.*, vol. 10, no. 4443-4449, 2010.

[123] H. Kuepers, R. B. Lewis, A. Tahraoui, M. Matalla, O. Krueger, F. Bastiman, H. Riechert, and L. Geelhaar, "Diameter evolution of selective area grown Ga-assisted GaAs nanowires," *Nano Res.*, vol. 11(5), no. 2885-2893, 2018.

[124] C. Sartel, D. L. Dheeraj, F. Jabeen, and J. C. Harmand, "Effect of arsenic species on the kinetics of GaAs nanowires growth by molecular beam epitaxy," *J. Cryst. Growth*, vol. 312, no. 2073-2077, 2010.

[125] D. Spirkoska, C. Colombo, M. Heib, M. Heigoldt, G. Abstreiter, and A. Fontcuberta i Morral, "The use of molecular beam epitaxy for the synthesis of high purity III-V nanowires," *J. Phys.: Condens. Matter*, vol. 20, no. 454225, 2008.

[126] L. Roskop, J. W. Evans, and M. S. Gordon, "Adsorption and Diffusion of Gallium Adatoms on the Si(100)-2X1 Reconstructed Surface: A Multiconfiguration Self-Consistent Field Study Utilizing Molecular Surface Clusters," *J. Phys. Chem. C*, vol. 115, no. 23488-23500, 2011.

[127] M. Zinke-Allmang, L. C. Feldman, and S. Nakahara, "Role of Ostwald Ripening in Islanding Processes," *Appl. Phys. Lett.*, vol. 51, no. 975, 1987.

[128] M. Kolibal, T. Cechal, E. Brandejsova, J. Cechal, and T. Sikola, "Self-limiting Cyclic Growth of Gallium Droplets on Si(111)," *Nanotechnology*, vol. 19(47), no. 475606, 2008.

[129] V. G. Dubrovskii, *Nucleation Theoryand Growth of Nanostructures.* Springer-Verlag Berlin Heidelberg, 2014.

[130] W. S. and H. Kroemer, "Reduction of oxides on silicon by heating in a gallium molecular beam at 800 degree celsius," *Appl. Phys. Lett.*, vol. 36(3), no. 210-211, 1980.

[131] S. M. Mostafavi Kashani, *Master thesis in Physics: Gallium Nanoparticle Deposition for Selfcatalyzed GaAs Nanowire Growth.* Lund University, 2013.

[132] E. P.A.M.Bakkers, M. T.Borgstrom, and M. A. Verheijen, "Epitaxial Growth of III-V Nanowires on Group IV Substrates," *MRS BULLETIN*, vol. 32, no. 117, 2007.

[133] X. Zhang, V. G. Dubrovskii, N. V. Sibirev, G. E. Cirlin, C. Sartel, M. Tchernycheva, J. C. Harmand, and F. Glas, "Growth of Inclined GaAs Nanowires by Molecular Beam Epitaxy: Theory and Experiment," *Nanoscale Res. Lett.*, vol. 5(10), no. 1692, 2010.

[134] C. N. Cochran and L. M. Foster, "Vapor Pressure of Gallium, Stability of Gallium Suboxide Vapor, and Equilibria of Some Reactions Producing Gallium Suboxide Vapor," *J. Electrochem. Soc.*, vol. 109(2), no. 144-148, 1962.

[135] H. Hijazi, V. G. Dubrovskii, G. Monier, E. Gil, C. Leroux, G. Avit, A. Trassoudaine, C. Bougerol, D. Castellucci, C. Robert-Goumet, and Y. An-

dre, “Influence of Silicon on the Nucleation Rate of GaAs Nanowires on Silicon Substrates,” *J. Phys. Chem. C*, vol. 122 (33), no. 19230-19235, 2018.

[136] A. Y. Cho, “Growth of III-V Semiconductors by Molecular Beam Epitaxy and Their Properties,” *Thin Solid Films*, vol. 100, no. 291-317, 1983.

[137] R. W. Olesinski, N. Kanani, and G. J. Abbaschian, “The Ga-Si (Gallium-Silicon) System,” *Bulletin of Alloy Phase Diagrams*, vol. 6, no. 4, 1985.

[138] H. Detz, M. Kriz, D. MacFarland, S. Lancaster, T. Zederbauer, M. Capriotti, A. M. Andrews, W. Schrenk, and G. Strasser, “Nucleation of Ga Droplets on Si and SiOx Surfaces,” *Nanotechnology*, vol. 26, no. 315601, 2015.

[139] S. Plissard, G. Larrieu, X. Wallart, and P. N. Caroff, “High yield of self-catalyzed GaAs nanowire arrays grown on silicon via gallium droplet positioning,” *Nanotechnology*, vol. 22, no. 275602, 2011.

[140] A. R. Madaria, M. Yao, C. Chi, N. Huang, C. Lin, R. Li, M. L. Povinelli, P. D. Dapkus, and C. Zhou, “Toward Optimized Light Utilization in Nanowire Arrays Using Scalable Nanosphere Lithography and Selected Area Growth,” *Nano Lett.*, vol. 12, no. 2839-2845, 2012.

[141] B. Fuhrmann, H. S. Leipner, H.-R. Hooche, L. Schubert, P. Werner, and U. Gosele, “Ordered arrays of silicon nanowires produced by nanosphere lithography and molecular beam epitaxy,” *Nano Lett.*, vol. 5, no. 2524-2527, 2005.

[142] D. S. Kim, R. Ji, H. J. Fan, F. Bertram, R. Scholz, A. Dadgar, K. Nielsch, A. Krost, J. Christen, U. Gosele, and M. Zacharias, “Laser-Interference Lithography Tailored for Highly Symmetrically Arranged ZnO Nanowire Arrays,” *Small*, vol. 3, no. 76-80, 2007.

[143] C. M. Lilleya and Q. Huang, “Surface contamination effects on resistance of gold nanowires,” *Appl. Phys. Lett.*, vol. 89, no. 203114, 2006.

[144] H. Detz, M. Kriz, S. Lancaster, D. MacFarland, M. Schinnerl, T. Zederbauer, A. M. Andrews, W. Schrenk, and G. Strasser, “Lithography-free positioned GaAs nanowire growth with focused ion beam implantation of Ga,” *J. Vac. Sci. Technol. B*, vol. 35, no. 011803, 2017.

[145] S. Lancaster, M. Kriz, M. Schinnerl, D. MacFarland, T. Zederbauer, A. M. Andrews, W. Schrenk, G. Strasser, and H. Detz, “Focused ion beam implantation

for the nucleation of self-catalyzed III-V nanowires, ," *MICROELECTRON ENG*, vol. 177, no. 93-97, 2017.

[146] A. B. Mosberg, S. Myklebost, D. Ren, H. Weman, B. O. Fimland, and A. T. J. van Helvoort, "Evaluating focused ion beam patterning for position-controlled nanowire growth using computer vision," *IOP Conf. Series: Journal of Physics: Conf. Series*, vol. 902, no. 012020, 2017.

[147] J. F. Ziegler, J. P. Biersack, and M. D. Ziegler, "SRIM-The stopping and range of ions in matter (2010)," *Nucl. Instrum, Methods Phys. Res. B*, vol. 268, no. 1818, 2010.

[148] R. M. A. Azzam and N. M. Bashara, *Ellipsometry and polarized light.* North-Holland, 1987.

[149] C. W. White, S. R. Wilson, B. R. Appleton, and F. W. Young Jr., "Supersaturated substitutional alloys formed by ion implantation and pulsed laser annealing of group-III and group-V dopants in silicon," *J. Appl. Phys.*, vol. 51, no. 738, 1980.

[150] M. I.-T. W. S. P. G. Schmid, "Vapor Pressure Calculator," www.iap.tuwien.ac.at, accessed: 21 Feb. 2019.

[151] G. M. Pound, M. T. Simnad, and L. Yang, "Heterogeneous Nucleation of Crystals from Vapor," *J. Chem. Phys.*, vol. 22(7), no. 1215-1219, 1954.

[152] C. Chatillon, I. Ansara, A. Watson, and B. B. Argent, "Re-assessment of the thermodynamic properties and phase diagrams of the Ga-As and In-As systems," *CALPHAD*, vol. 14(2), no. 203-214, 1990.

[153] S. G. Ihn, J. I. Song, T. W. Kim, D. S. Leem, T. Lee, S. G. Lee, and K. Koh, E. K. und Song, "Morphology and Orientation-Controlled Gallium Arsenide Nanowires on Silicon Substrates." *Nano Lett.*, vol. 7(1), no. 39-44, 2007.

[154] R. N. Proust, J. Magarino, and K. Zellama, "Crystallization Study of Chemically Vapour-Deposited Amorphous Silicon Films by In Situ X-ray Diffraction," *Thin Solid Films*, vol. 124(2), no. 171-177, 1985.

[155] P. Krogstrup, R. Popovitz-Biro, E. Johnson, M. H. Madsen, J. Nygard, and H. Shtrikman, "Structural phase control in self-catalyzed growth of GaAs nanowires on silicon (111)," *Nano Lett.*, vol. 10, no. 4475-4482, 2010.

[156] W. J. Williams, M. A. Pfeifer, I. A. Vartanyants, and I. K. Robinson, "Three-dimensional imaging of microstructure in Au nanocrystals," *Phys. Rev. Lett.*, vol. 90, no. 175501, 2003.

[157] M. Koehl, P. Schroth, A. A. Minkevich, J.-W. Hornung, E. Dimakis, C. Somaschini, L. Geelhaar, T. Aschenbrenner, S. Lazarev, D. Grigoriev, U. Pietsch, and T. Baumbach, "Polytypism in GaAs Nanowires: Determination of the Interplanar Spacing of Wurtzite GaAs by X-ray Diffraction," *J. Synchrotron Radiat*, vol. 22, no. 67-75, 2015.

[158] "Gallium Arsenide," http://www.ioffe.ru/SVA/NSM/Semicond/, accessed: 16 Jan 2019.

[159] "Gaussian function," en.wikipedia.org, accessed: 11 Jan 2019.

[160] J. C. Pinero, D. Araujo, C. E. Pastore, M. Gutierrez, C. Frigeri, B. A., J. F. Lelievre, and M. Gendry, "Twins and strain relaxation in zincblende GaAs nanowires grown on silicon," *Appl. Surf. Sci.*, vol. 395, no. 195-199, 2017.

[161] F. Fathi Aghdam, H. Liao, and Q. Huang, "Modeling Interaction in Nanowire Growth Process Toward Improved Yield," *IEEE T AUTOM SCI ENG*, vol. 14(2), no. 1139-1149, 2017.

[162] J. Johansson, B. A. Wacaser, K. A. Dick, and W. Seifert, "Growth related aspects of epitaxial nanowires," *Nanotechnology*, vol. 17(11), no. S355-S361, 2006.

[163] L. E. Jensen, M. T. Bjork, S. Jeppesen, A. I. Persson, B. J. Ohlsson, and L. Samuelson, "Role of surface diffusion in chemical beam epitaxy of inas nanowires," *Nano Letters*, vol. 4, no. 10, pp. 1961–1964, 2004.

[164] A. I. Persson, M. W. Larsson, S. Stenstrom, B. J. Ohlsson, L. Samuelson, and L. R. Wallenberg, "Solid-phase diffusion mechanism for gaas nanowire growth," *Nature Materials*, vol. 3, no. 677-681, 2004.

[165] A. M. Munshi, D. L. Dheeraj, J. Todorovic, A. T. J. van Helvoort, H. Weman, and B.-O. Fimland, "Crystal phase engineering in self-catalyzed GaAs and GaAs/GaAsSb nanowires grown on Si(111)," *J. Cryst. Growth*, vol. 372, no. 163-169, 2013.

[166] P. G. Callahan, B. B. Haidet, D. Jung, G. G. E. Seward, and K. Mukherjee, "Direct observation of recombination-enhanced dislocation glide in heteroepitaxial GaAs on silicon," *Phys. Rev. Materials*, vol. 2, no. 081601, 2018.

[167] B. Loitsch, D. Rudolph, S. Morkotter, M. Doblinger, G. Grimaldi, L. Hanschke, S. Matich, E. Parzinger, U. Wurstbauer, G. Abstreiter, J. J. Finley, and G. KoblmÃŒller, "Tunable Quantum Confinement in Ultrathin, Optically Active Semiconductor Nanowires Via Reverse-Reaction Growth," *Adv. Mater.*, vol. 27, no. 2195-2202, 2015.

[168] H. J. Butt and M. Jaschke, "Calculation of Thermal Noise in Atomic Force Microscopy," *Nanotechnology*, vol. 6, no. 1-7, 1995.

[169] D. R. Kiracofe, M. M. Yazdanpanah, and A. Raman, "Mass and Stiffness Calibration of Nanowires using Thermally Driven Vibration," *Nanotechnology*, vol. 22, no. 295504, 2011.

[170] S. O. Mariager, D. Khakhulin, H. T. Lemke, K. S. Kjaer, L. Guerin, L. Nuccio, C. B. Sorensen, M. N. Nielsen, and R. Feidenhans, "Direct Observation of Acoustic Oscillations in InAs Nanowires," *Nano Lett.*, vol. 10, no. 2461-2465, 2010.

[171] B. Krishnamachari, J. McLean, B. Cooper, and J. Sethna, "Gibbs-Thomson Formula for Small Island Sizes: Corrections for High Vapor Densities," *Phys. Rev. B*, vol. 54, no. 12, 1996.

[172] A. Plech, U. Klemradt, H. Metzger, and J. Peis, "In situ X-ray Reflectivity Study of the Oxidation Kinetics of Liquid Gallium and the Liquid Alloy," *J. Phys.: Condens. Matter*, vol. 10, no. 971, 1998.

[173] C. G. Nunez, A. F. Brana, N. Lopez, and B. J. Garcia, "A Novel Growth Method to Improve the Quality of GaAs Nanowires Grown by Ga-Assisted Chemical Beam Epitaxy," *Nano Lett.*, vol. 18, no. 3608-3615, 2010.

[174] M. F. Millea and D. F. Kyser, "Thermal Decomposition of Gallium Arsenide," *J. Appl. Phys*, vol. 36, no. 308, 1965.

[175] R. B. Lewis, P. Corfdir, H. Kuepers, T. Flissikowski, O. Brandt, and L. Geelhaar, "Nanowires Bending over Backward from Strain Partitioning in Asymmetric Core-Shell Heterostructures," *Nano Lett.*, vol. 18, no. 2343-2350, 2018.

[176] M. Keplinger, D. Kriegner, J. Stangl, T. Martensson, B. Mandl, E. Wintersberger, and G. Bauer, "Core-shell nanowires: From the Ensemble to Single-Wire Characterization," *Nucl. Instrum. Methods Phys. Res B*, vol. 268, no. 316-319, 2010.

[177] M. Belov, N. J. Quitoriano, S. Sharma, W. K. Hiebert, T. I. Kamins, and S. Evoy, "Mechanical Resonance of Clamped Silicon Nanowires Measured by Optical Interferometry," *J. Appl. Phys.*, vol. 103, no. 074304, 2008.

[178] T. D. Lowes and M. Zinke-Allmang, "Microscopic Study of Cluster Formation in the Ga on GaAs(001)," *J. Appl. Phys.*, vol. 73, no. 4937, 1993.

[179] F. Glas and J. C. Harmand, "Calculation of the Temperature Profile in Nanowhiskers Growing on a Hot Substrate," *Phys. Rev. B*, vol. 73, no. 155320, 2006.

[180] G. Markou, M. Papadrakakis, and A. Simplified, "Efficient Hybrid Finite Element Model (HYMOD) for Non-Linear 3D Simulation of RC Structures," *ENG COMPUTATION*, vol. 32, no. 1477-1524, 2015.

[181] "PILATUS3 R 300K," https://www.altadevices.com/use-gallium-arsenide-solar-cells/, accessed: 3 Jan 2019.

[182] I. Brough, P. S. Bate, and F. J. Humphreys, "Optimising the angular resolution of EBSD," *J. Mater. Sci. Technol.*, vol. 22, no. 1279-1286, 2006.

[183] G. Chen, B. Sanduijav, D. Matei, G. Springholz, D. Scopece, M. J. Beck, F. Montalenti, and L. Miglio, "Formation of Ge Nanoripples on Vicinal Si (1110): From Stranski-Krastanow Seeds to a Perfectly Faceted Wetting Layer," *Phys. Rev. Lett.*, vol. 108, no. 055503, 2012.

[184] G. A. Chahine, M. Richard, R. A. Homs-Regojo, T. N. Tran-Caliste, D. Carbone, V. L. R. Jacques, R. Grifone, P. Boesecke, J. Katzer, I. Costina, H. Djazouli, T. Schroeder, and T. U. Schulli, "Imaging of strain and lattice orientation by quick scanning X-ray microscopy combined with three-dimensional reciprocal space mapping," *J. Appl. Cryst.*, vol. 47, no. 762-769, 2014.

Chapter 8

Acknowledgements

> *"Doing a Ph.D. is like putting 100,000 piece puzzle together without a box. And the pieces keep changing shape and colour. And the room is on fire."*
> Emma Quilty

In the following, I would like to thank all the colleagues and amazing people who helped me to overcome this incredibly fun challenge called a Ph.D.

I would like to thank Prof. Ullrich Pietsch, my supervisor, gratefully. He provided continuous, generous, and open contribution in the last five years in all stages of the many projects included or not included in this thesis (see Chapter 1, list of publications and conferences). Moreover, he provided funding via BMBF projects (05K13PS3 and 05K16PSA). I would like to also thank him for training me to contribute in writing the BMBF and DESY proposals actively. With his supervision, we could have several successful projects accepted by the DESY review panels. Moreover, I would like to thank him for making a big group in Siegen and also collaborate with many researchers in different countries. That made it a unique opportunity for group members to grow. I was also privileged to learn from his outstanding management skills.

I would like to gratefully thank Prof. Tilo Baumbach, who provided support through the above-mentioned BMBF projects. I am thankful for that he accepted me as a research assistant visitor in KIT (Nord Campus) throughout my Ph.D. I would also like to thank him for giving me full access to all resources at the institute for photon science and synchrotron radiation and UHV Lab at ANKA. Moreover, it was a pleasure to openly talk to him about the scientific and sociological topics even late in the evenings during my time in Karlsruhe.

This work was done along with several other projects which belonged to my great tireless colleagues. I am honored and grateful for having the chance to work with such enthusiastic physicists. Therefore, I would like to delightedly thank my colleagues in

Siegen and KIT for our countless meetings and open discussions about each other's work as well as a wide range of topics in physics:

My colleagues at Siegen University: Arman Davtyan, Danial Bahrami, Jonas Vogel, Ali Abboud, Taseer Anjum, Lisa Randolph, Linda Grodd, Andreas Biermanns, etc.

My colleagues at KIT: Philipp Schroth, Ludwig Feigl, Julian Jakob, Martin Köhl, Helmuth Letzguss, etc.

I also would like to gratefully acknowledge and thank Dominik Kriegner from Max-Planck-Institute for Chemical Physics of Solids. For me, it has been a great pleasure to work with a brilliant and passionate physicist like him.

I would like to thankfully acknowledge UHV laboratory at ANKA, KIT, the house of the pMBE chamber. I would like to thank the competent lab-responsible people there: Barbel Krause, Hans Gräfe, Annette Weißhardt, who were always available with a smile.

I would like to acknowledge P09 beamline at Petra III, DESY, where the in-situ XRD experiments were performed. Moreover, I would also like to thank its enthusiastic staff: Jörg Strempfer, David Reuther, and Sonia Francoual.

I would like to acknowledge Siegen University, KIT INT, and DESY Nanolab for giving me access to the SEM machines and the helpful, and responsible staff, e.g., Michael Vogel, Thomas F. Keller, and Satishkumar Kulkani.

I would like to also express many thanks to all the other colleagues, friends, and people whom I met along the way and learned from them.

Last but not least, I would like to thankfully mention my incredible family members, my mother, father, and sister, who were always sending me love.